Fermilab

FERMILAB-THESIS-2002-56

MEASUREMENT OF CONTINUUM DIMUON PRODUCTION IN 800-GEV/C PROTON-NUCLEON COLLISIONS

BY

JASON C. WEBB, B.S.

A Dissertation submitted to the Graduate School

in partial fulfillment of the requirements

for the degree

Doctor of Philosophy

Major Subject: Physics

New Mexico State University

Las Cruces New Mexico

December 2002

"Measurement of Continuum Dimuon Production in 800-GeV/C Proton-Nucleon Collisions," a dissertation prepared by Jason C. Webb in partial fulfillment of the requirements for the degree, Doctor of Philosophy, has been approved and accepted by the following:

Roy C. Rodriguez
Interim Dean of the Graduate School

Vassili Papavassiliou
Chair of the Examining Committee

Date

Committee in charge:

Dr. Vassili Papavassiliou, Chair

Dr. Gary Kyle

Dr. William Gibbs

Dr. Vincent Gutschick

DEDICATION

For Mom.

ACKNOWLEDGMENTS

Any experiment in nuclear physics is the work of not one, but many. I would like to thank the members of the FNAL E866/NuSea collaboration for their hard work and dedication which made this thesis possible.

(finish before submitting to the graduate school.)

VITA

July 27, 1973–Born in Danville, IL

May 1995–B.S. in Physics, Valparaiso University, Valparaiso, IN

1995–Graduate Assistant, New Mexico State University, Las Cruces, NM

PROFESSIONAL SOCIETIES

Sigma Pi Sigma

ABSTRACT

MEASUREMENT OF CONTINUUM DIMUON PRODUCTION IN

800-GEV/C PROTON-NUCLEON COLLISIONS

BY

JASON C. WEBB, B.S.

Doctor of Philosophy in Physics

New Mexico State University

Las Cruces, New Mexico, 2002

Dr. Vassili Papavassiliou, Chair

Fermilab Experiment 866 has performed an absolute measurement of continuum dimuon (Drell-Yan) cross sections in 800-GeV/c pp and pd interactions. Results differential in the mass, Feynman-x (x_F) and transverse momenta (p_T) of the dimuon pairs are reported. These results represent the most extensive study of the Drell-Yan process to date, based on a data sample of 175,000 dimuon events covering the widest range in kinematics yet achieved ($4.2 \leq M \leq 16.85$ GeV and $-0.05 \leq x_F \leq 0.8$) with this level of precision. The cross sections are

primarily sensitive to the magnitude and shape of the light antiquark distributions ($\bar{d}(x)$ and $\bar{u}(x)$) in the nucleon, but also provide important information on the valence quarks as well as the gluons. They are in good agreement with other existing proton-induced Drell-Yan experiments. There is also general agreement between the data and next-to-leading-order calculations based on various sets of parton distribution functions. Differences between data and theory are examined, and the potential impact of these data on future parameterizations of the parton distributions are be discussed.

CONTENTS

LIST OF TABLES

LIST OF FIGURES

1 INTRODUCTION

Investigation into the field of lepton-pair production in hadronic interactions began with an experiment carried out at Brookhaven National Laboratory in 1970 [Chr 70]. This experiment studied the reaction $p\mathrm{U} \rightarrow \mu^+\mu^- X$ for proton energies between 22 and 29 GeV, resulting in pair masses between 1 and 6.7 GeV[1]. The data above ~ 3 GeV (where the J/ψ resonance family would later be found) exhibited a rapidly decreasing continuum of muon pairs. The steeply falling nature of the cross section was explained later that year by Drell and Yan [Dre 70], who were interested in dilepton production as a possible application of the quark-parton model of hadron structure outside of deeply-inelastic scattering experiments. Their model of quark-antiquark annihilation through the electromagnetic interaction, which has become known as the Drell-Yan process, was generally successful in describing the data and would only improve as our understanding of the strong interaction improved.

The Drell-Yan process still remains an active area of experimental and theoretical research some thirty years later. It has played a key role in developing the mathematical technology of perturbative Quantum Chromodynamics (QCD), being one of the first processes to be calculated to next-to-leading order $\mathcal{O}(\alpha_s)$, and remains one of the few processes to be calculated to next-to-next-to-leading

[1] Throughout this thesis, we will utilize "God-given" units, setting $\hbar = c = 1$.

$\mathcal{O}(\alpha_s^2)$. Experimentally it has provided a wealth of information about nucleon structure; its confirmation of the quark-parton model and its verification of the quark charge assignments being two notable early applications. In this thesis we describe and report the results of an absolute measurement of the dimuon cross sections from the interaction of an 800-GeV proton beam with hydrogen and deuterium targets. As will be shown, these data provide important information about the distributions of antiquarks in the nucleon sea.

1.1 Background

The disciplines of high-energy and particle physics consist of the search for the ultimate constituents of matter and the study of the fundamental interactions between them. With the introduction of Quantum Chromodynamics in the mid-1970's, a consistent treatment of the weak, electromagnetic and strong interactions was finally realized. The gauge field theories of Quantum Electrodynamics (QED) and the Weinberg-Glashow-Salam model had long treated the electromagnetic and weak interactions felt by the leptons – the electron (e), muon (μ), tau (τ), and associated neutrinos (ν_e, ν_μ, ν_τ) – as the exchange of gauge field bosons (the photon (γ) and the $W^\pm$ and Z^0 bosons). Attempts to formulate similar theories for the strongly interacting hadrons, however, initially met with only limited success. The realization by Gell-Mann and (independently) Zweig in 1964 that the hadron spectrum could be explained in terms of three fractionally charged

Table 1.1: Properties of the light quarks. Shown are the isospin (I) and its third component (I_3), strangeness (S), baryon number (B) and charge (Q/e).

flavor	I	I_3	S	B	Q/e
u	$1/2$	$1/2$	0	$1/3$	$2/3$
d	$1/2$	$-1/2$	0	$1/3$	$-1/3$
s	0	0	-1	$1/3$	$-1/3$

fermionic constituents, called quarks, set the stage for the development of QCD and its inclusion in what has become known as the Standard Model.

Although Gell-Mann and Zweig's static quark model needed only three different quark flavors, experiment confirms the existence of six, with larger numbers being ruled out in the framework of the Standard Model by recent experiments. The six quarks are conventionally known as up (u), down (d), strange (s), charm (c), bottom (b) and top (t) and are found only in bound states called hadrons: mesons ($\pi^{\pm}$, π^0, J/ψ, etc...) are quark-antiquark ($q\bar{q}$) bound states, while baryons (p, n, Δ^{++}, etc...) are the bound states of three quarks (qqq). Table 1.1 shows the quantum numbers of the three quarks of the first three quarks. In order to avoid violating the Pauli principle in baryons such as the Δ^{++} (uuu), the static quark model had to add an additional quantum number called color. Each quark carries one of three colors (red, green or blue). An object in which all three colors (or one color and its anti-color) are present is a color-neutral (color-singlet) state.

Color was an *ad hoc* addition to the static quark model. The role which it plays in QCD is more fundamental. QCD is a non-Abelian color gauge field theory, the three colors representing the fundamental basis of the $SU(3)$ symmetry group. Color plays essentially the same role in the strong interaction as electric charge in electromagnetism, the principal difference being the number of "charge" states – two electric charge states ($+$ and $-$) versus six color states (r, g, b, $\bar{r}$, $\bar{g}$, $\bar{b}$)[2]. The quarks interact through the exchange of QCD's gauge field bosons, the gluons (g). Unlike the photons in QED, which are electrically neutral, the gluons carry color charge. This leads to some important differences. A well-known property of QED is the running of the electromagnetic coupling constant $\alpha \approx \frac{1}{137}$. A test charge polarizes the virtual e^+e^- pairs surrounding it, leading to screening of the test charge at larger distances, resulting in an effective reduction in α. Probing the test charge at smaller distance scales, i.e. larger momentum transfers (q^2), results in an observed increase in the coupling. The same effect occurs in QCD, but the color-charged gluons are self interacting. This leads to an antiscreening of the color test charge, resulting in a decrease in the strong coupling constant (α_s) with increasing q^2. This property of the strong interaction is known as asymptotic freedom.

Owing to the mathematical complexity of the $SU(3) \otimes SU(2) \otimes U(1)$ Standard Model, exact solutions are often not possible for physical interactions. We must

[2]Red, green, blue and their anti-colors.

therefore rely upon perturbation theory to obtain meaningful predictions from the model. This has never presented a problem in either the weak or electromagnetic interactions, where one can simply carry out the perturbative expansion in the coupling constant to whatever level of precision is desired. However, the strong interaction derives its name from the fact that it is a *strong* interaction. For momentum scales on the order of the proton mass, the size of the strong coupling constant ($\alpha_s(M_p^2) \sim 1$) renders fixed-order perturbation theory meaningless – all orders in the perturbative expansion are significant. Fortunately, the asymptotic freedom exhibited by QCD results in a strong coupling constant which decreases with increasing q^2. At momentum-transfers typical of high-energy fixed-target experiments, α_s becomes sufficiently small that it may be reliably used as an expansion parameter. Nevertheless, it remains sufficiently large that terms next-to-leading order in α_s may remain important.

An additional complication in hadronic interactions is that we cannot be certain which of the interacting partons (the quark, antiquark and gluon constituents) are participating in the interaction. We can at best speak of the probability of finding a given parton carrying a fraction x (called Björken-x) of the interacting hadron's momentum, which we in general denote by $f_{q/A}(x)$ for a parton of type q in a hadron of type A. Calculations of physical processes in the Standard Model are thus predicated on prior knowledge of these parton distribution functions (PDF's).

Of particular importance to many experiments are the parton distributions in the nucleon (i.e. $u(x) = f_{u/p}(x)$, $\bar{u}(x) = f_{\bar{u}/p}(x)$, etc...). Early parameterizations of the PDF's relied on fits to the structure functions measured in deeply-inelastic lepton-hadron scattering experiments (DIS), which are primarily sensitive to the light quark distributions ($u(x)$ and $d(x)$). More modern parameterizations, such as those performed by the CTEQ, MRST and GRV collaborations [MRST, CTEQ, GRV] use several different physical processes to extract complementary information about the parton distributions. The lepton-charge asymmetry observed in $W^{\pm}$ production provides additional information about the light quark distributions, while jet production and prompt photon measurements are used to constrain the gluon distributions. The Drell-Yan process for dilepton production, which involves quark-antiquark annihilation, provides constraints on the light antiquark distributions ($\bar{u}(x)$ and $\bar{d}(x)$) in the nucleon sea. The CTEQ 5 set of parton distributions is shown in figure 1.1, along with the light antiquark distributions from the MRST 98 and GRV 98 distributions.

1.2 The Drell-Yan Process

Prior to the introduction of QCD, hadronic interactions were calculated with some success using the quark-parton model, whereby the interacting partons (quarks and antiquarks) were treated as being free of the strong interactions on the timescale of a hard interaction (the impulse approximation). Cross sections

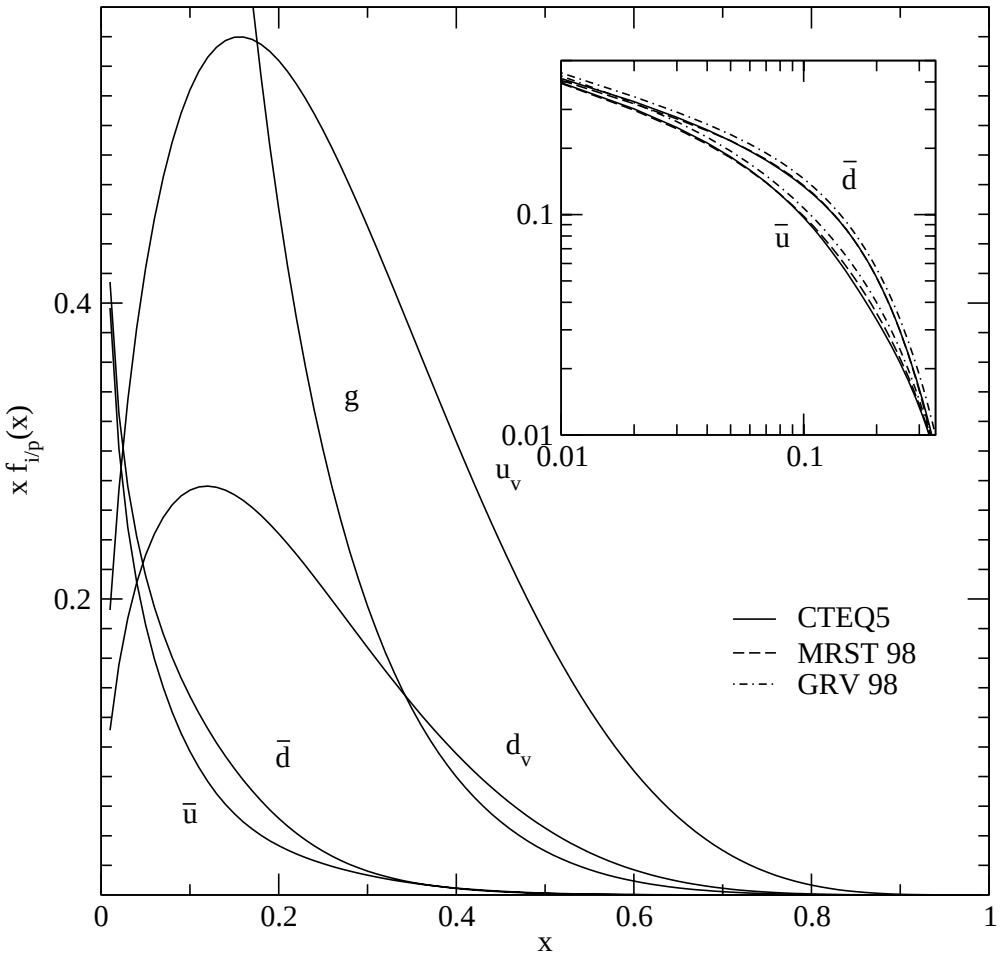

Figure 1.1: CTEQ5 partons. Shown are the valence quark and light anti-quark distributions, and the gluons. The inset compares $\bar{d}(x)$ and $\bar{u}(x)$ from the CTEQ5 [CTEQ], MRST 98 [MRST] and GRV 98 [GRV] fits.

involving hadrons were then reduced to the comparatively simple problem of calculating the parton-level cross sections and folding in the probability to find the particular parton configuration. Figure 1.2 shows the Feynman diagram for the Drell-Yan process for lepton pair production in proton-nucleon collisions in the dimuon channel studied by E866. In the initial state, a quark (antiquark) carrying a fraction x_1 of the beam's momentum annihilates an antiquark (quark) carrying a fraction x_2 of the target's momentum. This results in a time-like ($q^2 > 0$) intermediate photon, which decays into the final state $\mu^+\mu^-$ pair.

1.2.1 Kinematics

In the lab, we measure the invariant mass of the muon pair, and their total longitudinal momentum. The mass of the dimuon is related to the momentum fractions of the interacting partons by

$$q^2 = M^2 = s\, x_1 x_2 \tag{1.1}$$

where s is the total four-momentum squared of the interacting hadrons. The longitudinal momentum of the dimuon, as a fraction of its maximum possible value ($p_L^{\max} \approx \sqrt{s}/2$), is referred to as Feynman-x (x_F). It is related to the initial state momentum fractions by

$$x_F = \frac{p_L}{p_L^{\max}} = x_1 - x_2. \tag{1.2}$$

Thus, measurement of the invariant mass and x_F of the muon pair allows us to determine the momentum fractions carried by the interacting partons. Solving for x_1 and x_2 in equations 1.1 and 1.2 we find

$$x_{1,2} = \frac{1}{2}(x_F \pm \sqrt{x_F^2 + 4\tau}) \tag{1.3}$$

where we have taken $\tau = x_1 x_2 = M^2/s$.

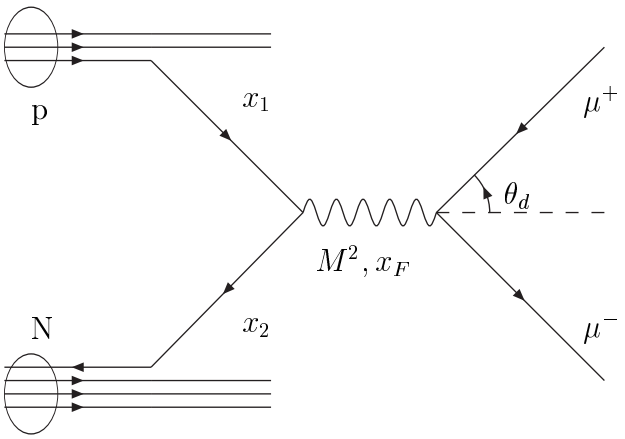

Figure 1.2: The Drell-Yan process for dimuon production.

In order to completely specify the final state of the interaction, we need four more variables. One of these is the momentum of the muon pair transverse to the beam, denoted by p_T. This is expected to be small in the Drell-Yan process: $< p_T > \approx 0.3$ GeV, non-zero only due to Fermi smearing of the momenta of the interacting partons. The larger values of p_T which are observed in dilepton production require additional partons in the final state, which are provided by the higher-order QCD processes which we discuss later.

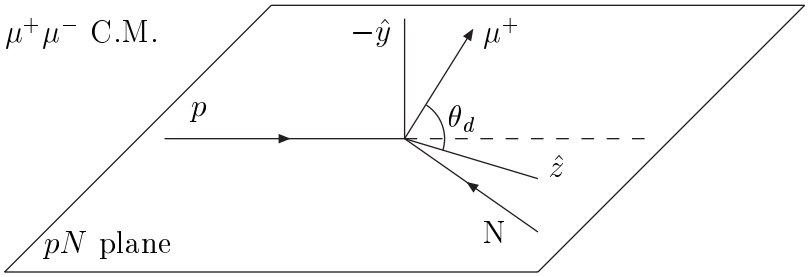

Figure 1.3: Definition of the Collin-Soper frame.

The three other variables which characterize the process are the polar decay angle θ_d, and the azimuthal production and decay angles ϕ_p and ϕ_d respectively. These variables are most naturally defined with respect to the $q\bar{q}$ annihilation axis. However, when p_T is non-zero, this axis becomes difficult to measure. The angular variables are therefore measured with respect to the Collins-Soper frame [Col 77], which is shown schematically in figure 1.3. In this frame, the z-axis is taken to be parallel to the bisector of the angle between the interacting hadrons in the rest frame of the virtual photon.

1.2.2 Cross Section

The cross section for the Drell-Yan process is easily constructed in the quark-parton model. The assumption that the interacting quark and antiquark are free on the timescale of the hard interaction allows us to factor the cross section into a short distance $q\bar{q}$ annihilation term ($\sigma_{q\bar{q}}$), and a term expressing the probability of finding the particular partonic configuration. The $q\bar{q}$ annihilation cross section

is simply given by [Dre 70]

$$\sigma_{q\bar{q}} = \frac{1}{3}\frac{4\pi\alpha^2}{3M^2}e_q^2 \tag{1.4}$$

which is just the cross section for the annihilation of two fermions in QED, multiplied by a factor of 1/3 required by color conservation and a factor of e_q^2 to account for the fractional charge of the quarks. Multiplying by the probability of a quark (antiquark) in the beam annihilating an antiquark (quark) in the target and summing over all parton species we have an expression for the Drell-Yan cross section differential in x_1 and x_2

$$\frac{d^2\sigma_{AB}}{dx_1 dx_2} = \frac{1}{3}\frac{4\pi\alpha^2}{3M^2}\sum_{q\in u,d,s,\ldots} e_q^2\left[f_{q/A}(x_1)f_{\bar{q}/B}(x_2) + f_{\bar{q}/A}(x_1)f_{q/B}(x_2)\right]. \tag{1.5}$$

Expressed in terms of quantities measured in the lab we obtain

$$M^2\frac{d^2\sigma_{AB}}{dM^2 dx_F} = \frac{1}{3}\frac{4\pi\alpha^2}{3M^2}\frac{x_1x_2}{x_1+x_2}\sum_q e_q^2\left[f_{q/A}(x_1)f_{\bar{q}/B}(x_2) + f_{\bar{q}/A}(x_1)f_{q/B}(x_2)\right] \tag{1.6}$$

where equation 1.3 is used to evaluate x_1 and x_2. Alternatively, we can express the cross section in terms of the dimensionless variables τ and $y = \frac{1}{2}\ln\frac{x_1}{x_2}$ (the rapidity)

$$s\frac{d^2\sigma_{AB}}{d\tau dy} = \frac{1}{3}\frac{4\pi\alpha^2}{3\tau}\sum_q e_q^2\left(f_{q/A}(x_1)f_{\bar{q}/B}(x_2) + f_{\bar{q}/A}(x_1)f_{q/B}(x_2)\right). \tag{1.7}$$

This is known as the scaling form of the cross section.

1.2.3 Predictions

The Drell-Yan model makes some important predictions about the dilepton cross sections. The left-hand side of equation 1.7 is a function of the variables τ, y

and s, while the right-hand side is only a function of τ and y. Thus, the model predicts that the cross sections multiplied by s, and measured at different beam energies, but the same kinematics, should be the same – the cross sections should scale with $\frac{1}{s}$, and this is generally observed [Yoh 78, Con 89, Ant 82].

Another important prediction is the shape of the angular distributions. The angular distribution of the μ^+ in the pair rest frame can be expressed as [Cle 78]

$$\frac{d^2\sigma}{d\phi_d \, d\cos\theta_d} \propto 1 + \lambda \cos^2\theta_d + \mu \ \sin\ 2\theta_d \cos\phi_d + \nu/2 \sin^2\theta_d \ \cos\ 2\phi_d \qquad (1.8)$$

where λ, μ and ν are functions of the other kinematic variables. For the Drell-Yan process, the assumption of massless quarks implies that the virtual photon is transversely polarized ($\lambda = 1$, $\mu = \nu = 0$), resulting in the prediction

$$\frac{d^2\sigma}{d\cos\theta_d} \propto 1 + \cos^2\theta_d \qquad (1.9)$$

when θ_d is measured with respect to the $q\bar{q}$ annihilation axis. Several experiments [Con 89, McG 99, Cha 99, Bro 01] have confirmed that the dileptons are produced transversely polarized.

Despite these successes in describing experimental data, the Drell-Yan model also had some initial failures. Because there are no particles in the final state off which to recoil, any transverse momentum in the dilepton must originate with the initial state. The mechanism for this is most likely Fermi smearing of the parton distributions, and the expected size of this intrinsic k_T is small (~ 300 MeV). The

observed (s-dependent) values of $< p_T^2 > \sim 1.75$ GeV^2 cannot be reproduced by this mechanism in the Drell-Yan process.

A second problem came about when absolute measurements of the dilepton cross sections were compared to Drell-Yan calculations based on the early PDF fits to DIS structure functions. Table 1.2 shows the K-factors, defined as the ratio of measured to calculated cross sections ($K = \sigma_{\text{meas.}}/\sigma_{\text{DY}}$), from several different experiments using different beams and targets. Typically, experiments measured a cross section which was a (nearly constant) factor of two larger than the Drell-Yan model and DIS structure function measurements implied. Along with the discrepancy in the p_T distribution, this was taken as a sign that QCD would play an important role in dilepton production.

1.3 QCD Modifications

With the introduction of QCD, the basic physics behind the Drell-Yan process was confirmed theoretically. That quark-antiquark annihilation gives rise to dilepton pairs is a consequence of the electromagnetic interaction. QCD provides substantial, albeit well-known, corrections to the leading-order (LO) electromagnetic contribution described by Drell and Yan. The diagrams which contribute at next-to-leading order (NLO or $\mathcal{O}(\alpha_s)$) are shown in figure 1.4. The gluon-bremsstrahlung and vertex-correction diagrams represent corrections to the basic $q\bar{q}$ annihilation picture of the Drell-Yan process, increasing the magnitude of the theoretical cross

Table 1.2: Experimental K-factors from several different early lepton pair production experiments.

Experiment	Interaction	Beam Momentum	$K = \sigma_{\text{meas.}}/\sigma_{\text{DY}}$
E288 [Kap 78]	$p\ Pt$	300/400 GeV	~ 1.7
WA39 [Cor 80]	$\pi^{\pm}\ W$	39.5 GeV	~ 2.5
E439 [Smi 81]	$p\ W$	400 GeV	1.6 ± 0.3
NA3 [Bad 83]	$(\bar{p}$ - $p)Pt$	150 GeV	2.3 ± 0.4
	$p\ Pt$	400 GeV	$3.1 \pm 0.5 \pm 0.3$
	$\pi^{\pm}\ Pt$	200 GeV	2.3 ± 0.5
	$\pi^{-}\ Pt$	150 GeV	2.49 ± 0.37
	$\pi^{-}\ Pt$	280 GeV	2.22 ± 0.33
NA10 [Bet 85]	$\pi^{-}\ W$	194 GeV	$\sim 2.77 \pm 0.12$
E326 [Gre 85]	$\pi^{-}\ W$	225 GeV	$2.70 \pm 0.08 \pm 0.40$
E537 [Ana 88]	$\bar{p}\ W$	125 GeV	$2.45 \pm 0.12 \pm 0.20$
E615 [Con 89]	$\pi^{-}\ W$	252 GeV	1.78 ± 0.06

section and providing a mechanism to reach larger values of p_T. Resummation techniques have been developed, which enable the calculation of such corrections to all orders in α_s. Taking K equal to the resummed cross section divided by the LO contribution gives $K \approx 1.8$ for α_s evaluated at q^2 typical of fixed-target experiments. This already accounts for much of the experimental K-factor.

The contributions described above are simply modifications to the basic $q\bar{q}$ picture of the Drell-Yan process – the main interaction is still the electromagnetic annihilation of the interacting partons, with the strong interaction only modifying the initial states of the $q\bar{q}$ pair. The gluon Compton-scattering diagram, however, is fundamentally different. Here, the incoming quark (antiquark) scatters off a gluon through the strong interaction, emitting the virtual photon which decays in the final state of the interaction. Theoretical studies of this process by Berger *et al.* [Ber 98] have shown that for transverse momenta large compared to the mass of the pair ($p_T > M/2$), the gluon Compton scattering diagrams dominate the cross section (accounting for $\approx 80\%$ of the NLO calculation). Therefore, with increasing p_T, the dilepton cross section becomes less sensitive to the antiquark distributions, and more sensitive to the gluons.

1.4 Motivation

The primary goal of Fermilab Experiment 866 (FNAL E866/NuSea) was to measure the ratio of continuum dimuon cross sections in proton-deuteron (σ_{pd}) interactions to those in proton-proton (σ_{pp}) interactions. These measurements are sensitive to the x-dependence of the ratio $\bar{d}/\bar{u}$ in the nucleon, and were motivated by several experiments [Ama 91, Bal 94, Ada 95] which demonstrated a large and previously unanticipated flavor asymmetry $\bar{d}/\bar{u} > 1$. The E866 results [Haw 98, Tow 01], which were based on a large sample of dimuon events

Gluon Bremsstrahlung ($q\bar{q}g$)

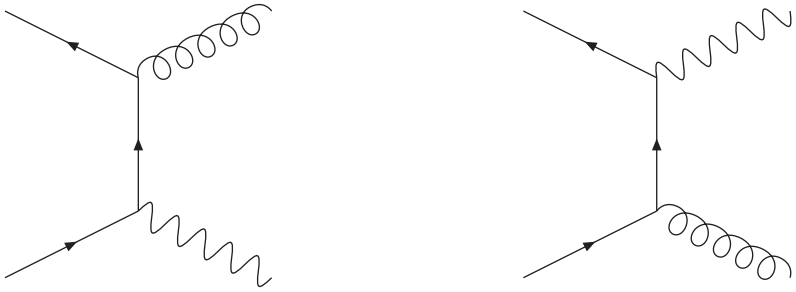

Gluon Compton Scattering (qg and $\bar{q}g$)

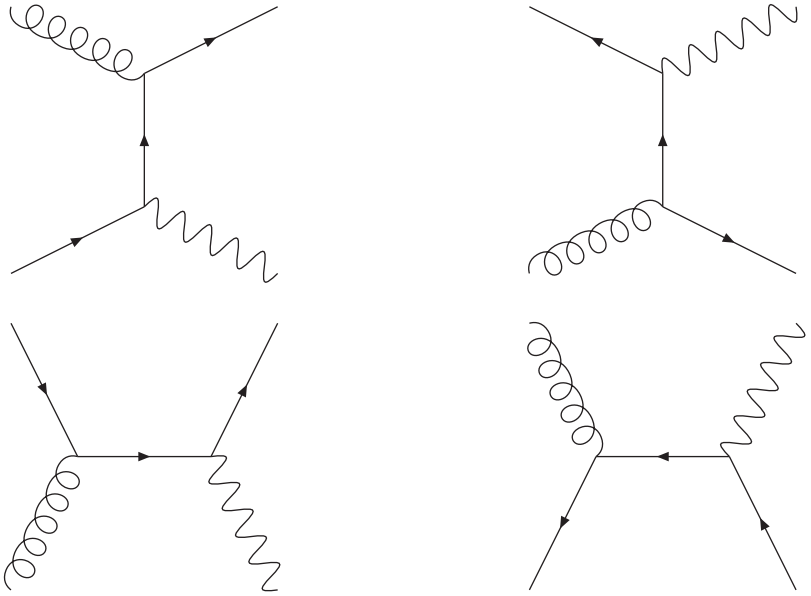

Vertex correction ($q\bar{q}$)

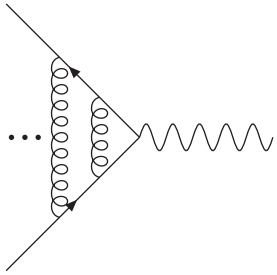

Figure 1.4: Next-to-leading order (NLO) diagrams which contribute to the dilepton cross section. The final state muon pair is omitted.

($\approx 360,000$) induced by an 800-GeV proton beam ($\sqrt{s} = 38.8$ GeV) interacting with hydrogen and deuterium targets, provided the first determination of the strong x-dependence of this flavor asymmetry.

Absolute measurements of the hydrogen and deuterium cross sections, the topic of this thesis, provide additional information on the magnitude and absolute shape of the light antiquarks. This can be easily shown by writing the leading-order cross section expression in equation 1.6 for various targets. Evaluating the sum for the hydrogen cross section, and taking the limit of large x_F appropriate for much of the E866 data[3] we have

$$\left(M^2 \frac{d^2\sigma}{dM^2 dx_F}\right)_{x_1 \gg x_2} \approx \frac{1}{3}\frac{4\pi\alpha^2}{3M^2}\left(\frac{4}{9}u(x_1)\bar{u}(x_2) + \frac{1}{9}d(x_1)\bar{d}(x_2)\right). \qquad (1.10)$$

Owing to the larger charge-squared factor in front of the $u\bar{u}$ term and the size of the up distribution compared to that of the down distribution in the proton, about 80% of the proton cross section at leading order is due to the $u\bar{u}$ annihilation. Thus, to the extent that the valence distributions are known (DIS measurements constrain these well in our kinematic range), the proton cross section provides a direct measurement of the $\bar{u}(x)$ distribution.

The deuterium cross section can be similarly written. Nuclear effects in deuterium are small, and confined to small x_2 [Ald 90]. This allows us to express the deuterium cross section as the sum $\sigma_{pd} = \sigma_{pp} + \sigma_{pn}$. If we assume that charge

[3] In the large x_F limit, x_1 is sufficiently large compared to x_2 that we can neglect terms in the cross section with the antiquark in the beam and the quark in the target.

symmetry holds, then the parton distributions in the proton and neutron are related through $u(x) = d^n(x)$, $\bar{u}(x) = \bar{d}^n(x)$, etc.... This yields an expression for the deuterium cross section (per nucleon)

$$\left(M^2 \frac{d^2\sigma}{dM^2 dx_F}\right)_{x_1 \gg x_2} \approx \frac{1}{3}\frac{4\pi\alpha^2}{3M^2}\left\{\frac{4u(x_1) + d(x_1)}{9}\right\}\left[\bar{d}(x_2) + \bar{u}(x_2)\right] \qquad (1.11)$$

where we have again taken the large-x_F limit. Thus, the deuterium cross section is directly proportional to the sum of the light antiquarks $\bar{d}(x) + \bar{u}(x)$.

In this thesis we describe and report results on the absolute measurement of continuum dimuon production in 800-GeV pp and pd interactions. The doubly-differential ($M^3 d^2\sigma/dMdx_F$) and triply-differential ($Ed^3\sigma/dp^3$) cross sections have been measured over a large range in the mass ($4 \leq M \leq 16.85$ GeV), x_F ($-0.05 \leq x_F \leq 0.8$) and p_T ($0 \leq p_T \leq 7$ GeV) of the muon pair. These data represent the first such measurement of the pp cross sections over an extended range of kinematics, while the pd cross sections have been measured over a wider kinematic range with greater statistical precision than has previously been achieved.

Traditionally, the Drell-Yan process is discussed in the context of probing the light antiquark distributions in the proton. And indeed, that was the primary motivation of this experiment. But it is clear from equations 1.10 and 1.11 that dimuon production also provides sensitivity to the valence distributions. While the kinematic range covered by previous dimuon measurements [Mor 91] has been limited to regions where the valence quarks are well constrained by DIS measure-

ments, the E866 data cover a much wider kinematic range. Our data probe the valence out to $x \sim 0.8$, which provides an important measurement of the large-x behavior of the valence quarks complimentary to existing DIS measurements.

2 APPARATUS

Fermilab Experiment 866 used a modified version of the dimuon spectrometer [Cri 86] located in the Meson East experimental area at the Fermi National Accelerator Laboratory. Previous experiments which used this spectrometer were E605, E772 and E789. Figure 2.1 shows a drawing of the E866 spectrometer, which was designed to detect oppositely-charged muon pairs while minimizing sensitivity to everything else. The coordinate system of the spectrometer was defined in the following way: the z-axis of the spectrometer was parallel to the nominal direction of the beam; the x-axis laid parallel to the floor of the experimental hall, pointing to the left facing station-1 from the targets; the y-axis then formed the right-handed Cartesian coordinate system by pointing up, perpendicular to the floor of the experimental hall. The origin of the coordinate system was chosen as the center of the upstream face of the SM12 magnet.

2.1 Beam line

An 800-GeV proton beam was extracted from the Fermilab Tevatron, split at the switchyard and sent to several fixed target experiments which ran concurrently during the 1996 fixed target run. The beam was transported down the east beam line of the Meson experimental area and arrived at the target in 20-second-long spills, with new spills arriving once every minute. The accelerator's frequency

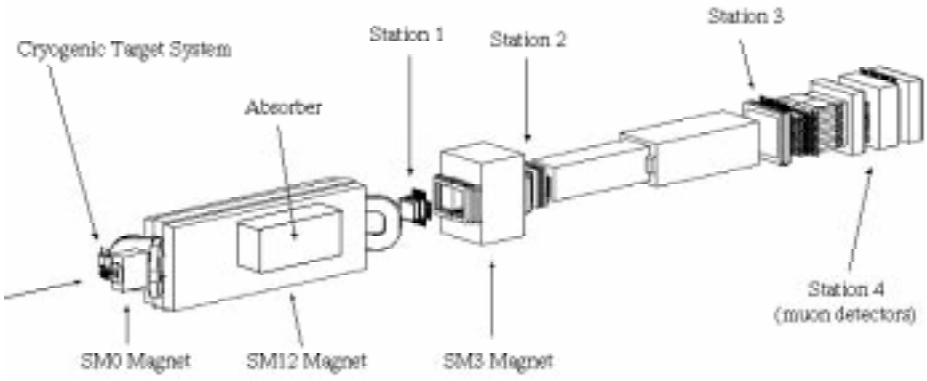

Figure 2.1: FNAL E866/NuSea Spectrometer.

was 53 MHz, which meant that during the spill the protons arrived grouped into "buckets" separated by 19 ns. The typical intensities which were used for E866 were between 1×10^{11} and 2×10^{12} protons per spill, depending on trigger rates and radiation-safety requirements for a particular spectrometer configuration.

The position, size and intensity of the beam was constantly monitored at various points along the beam line by several detectors. The beam's position and size were monitored by segmented wire ion chambers (SWICs). The last SWIC in the beam line was located approximately 188 cm upstream of the target. It had a 2 mm horizontal wire spacing and a 0.5 mm vertical wire spacing. During the experiment, the beam spot on the target was approximately 6 mm wide by 1 mm high.

Three different types of detectors monitored the intensity of the beam. The

primary detector was a secondary-emission monitor (SEM), located at about 100 m upstream of the targets. In addition to the SEM counter, an ion chamber (IC3) and a quarter-wave RF cavity were used. These additional detectors allowed us to study the linearity and offsets of the SEM.

The luminosities of the targets were also monitored during the experiment with a pair of four element scintillator telescopes located about 85° from the beam direction in the horizontal plane. The data from these detectors (referred to as AMON and WMON) were used to determine beam duty factor, data acquisition live-time and which target was in the beam during the spill.

2.2 Targets

Three identical target flasks, one of which is shown in figure 2.2, were mounted on a movable table located at $z \approx -400$ cm. They consisted of a 17-inch long cylindrical shell with a 3-inch inside diameter. Hemispherical end caps with a 3-inch diameter sealed either end, creating a 20-inch (50.8-cm) long target along the beam axis[1]. Facing the targets from upstream, the leftmost target was filled with liquid hydrogen and the rightmost target was filled with liquid deuterium. The center target was empty and held at vacuum to measure the background rates due to the beam interacting with the SWIC, the material in the target flasks, and

[1] It was confirmed by visual inspection after the experiment that the z-axis of each target was aligned properly with the beam.

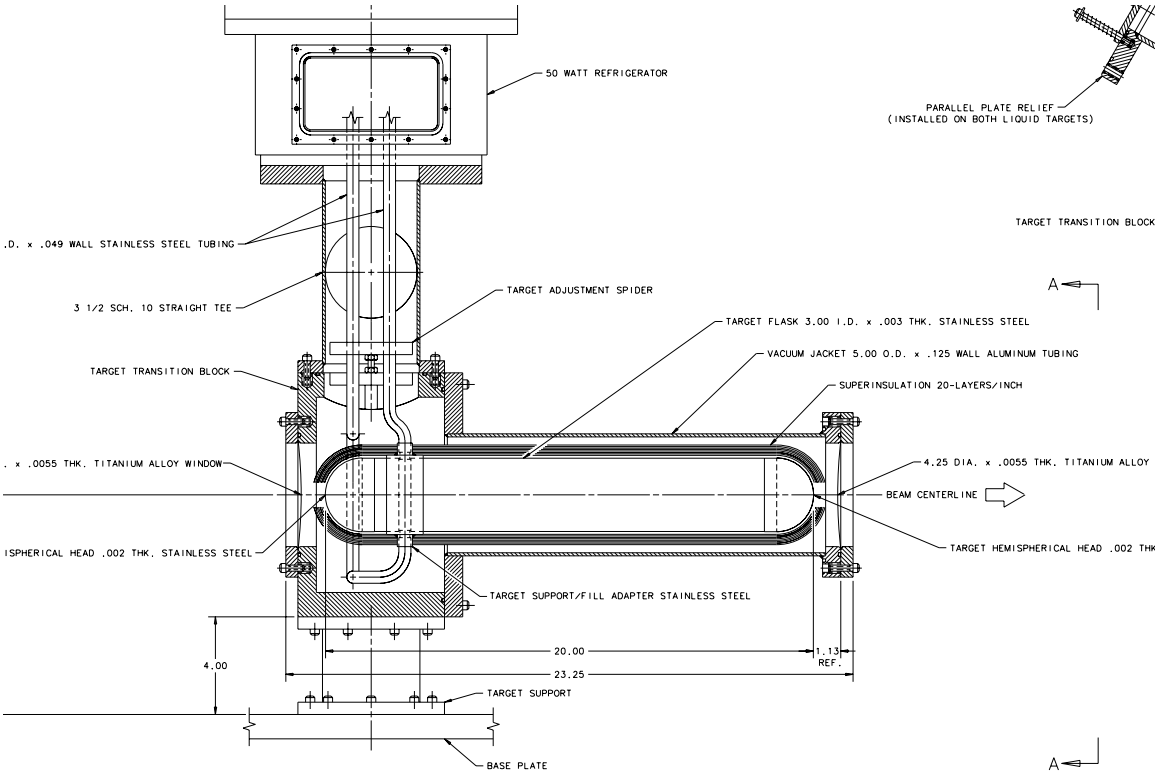

Figure 2.2: One of the three identical target flasks used in E866.

the air and other materials downstream of the target. Immediately downstream of the target, filling the aperture of the SM0 magnet, was a bag filled with helium to reduce background interactions in the vicinity of the targets.

The targets were cycled periodically to minimize the systematic uncertainties between the hydrogen and deuterium measurements. The programed sequence was 5 spills on the deuterium target followed by 1 spill on the empty target, 5 spills on the hydrogen target, and one more spill on the empty target. The target control computer counted only "good" spills – spills which the DAQ determined

had a sufficiently large number of protons. Upon receipt of the appropriate number of good spill signals, which were sent after the end of the spill, the target-control computer initiated the move to the next target in the sequence. The move was completed before the beginning of the next spill.

A set of four switches on the target table were engaged by a stationary roller mounted in front of the table. The positions of these switches corresponded to the beam striking the center of each of the targets, plus a fourth position where the targets were clear of the beam. When engaged, each switch completed a circuit which was read out by the DAQ, recording which target was in the beam. The switches were also tied into the beam interlock system, which required that one of the four switches be engaged for beam to be allowed to enter the target area. This ensured that the beam would not be able to hit the sides of the target flasks and cause a radiation hazard.

2.3 Spectrometer Magnets

The E866 spectrometer used three dipole magnets whose magnetic fields were oriented in the x direction (bending charged particles in the y direction). The two magnets closest to the targets were SM0 and SM12. These magnets were used to optimize the acceptance of the spectrometer for different ranges of dimuon masses. The SM12 magnet was used to focus dimuon pairs on the downstream detector elements. Access to higher-mass events, which tend to have larger opening angles,

was possible by using larger magnetic fields in SM12. This would ensure that such events were kept inside the aperture of the SM12 magnet and the detector stations.

The SM0 magnet was used to optimize the spectrometer for lower mass dimuon events in the low-mass data set. In this data set, the SM0 magnet was used to defocus (increase the opening angle of) the $\mu^+\mu^-$ pairs before they entered SM12. This increased the probability that the muons would miss the dump. More importantly, this increased the probability that the events would miss the dump cut used to eliminate beam-like muons, which were indistinguishable from the high flux of muons produced in the dump.

The SM3 magnet was located between the station-1 and station-2 detectors. It was used in the experiment to analyze the momentum of the muons by measuring the deflection it produced in the tracks. It was operated using a single current of 4230 A throughout the experiment.

2.4 Beam Dump and Hadronic Absorbing Wall

In order to prevent damage to the downstream detectors from the beam the target was followed by a large, water-cooled beam dump whose upstream face was located at $z \approx 173$ cm. The beam dump consisted of 255 cm of copper, which spanned -15.25 cm $\leq y \leq$ 15.25 cm at its thickest point. At its widest, the dump blocked the entire x-aperture of the magnet. The beam dump was nominally centered on

the z-axis, but had settled over the years and developed a small slope relative to SM12 such that it was approximately $0.2''$ low at $z = 68''$ and $0.4''$ low at $z = 530''$.

A large hadronic absorbing wall was located immediately downstream of the beam dump. The purpose of this wall was to fully attenuate the intense flux of hadrons produced in the target and the dump. The absorbing wall consisted of 61 cm of copper[2] in the most upstream section, followed by a 205.8 cm section of carbon, a 68.6 cm long section containing both carbon and polyethylene, and a 183 cm section of polyethylene. The configuration of the beam dump and absorbing wall is shown in figure 2.3.

2.5 Detector Stations

Four detector stations were responsible for triggering on dimuon events and tracking the muons which traversed the spectrometer. The first three detector stations consisted of hodoscope- and drift chamber-planes, while station-4 consisted of hodoscope- and proportional-tube planes. The fast response time of the hodoscopes was utilized to trigger on events with the expected dimuon signature, at which point the slower responding drift chambers could be read out. The proportional-tubes and hodoscopes at station-4 were used to provide some position information to the trigger, and discriminate against any hadrons which made

[2] There was a 7.6 cm gap between the copper and carbon sections of the absorbing wall in the region behind the dump.

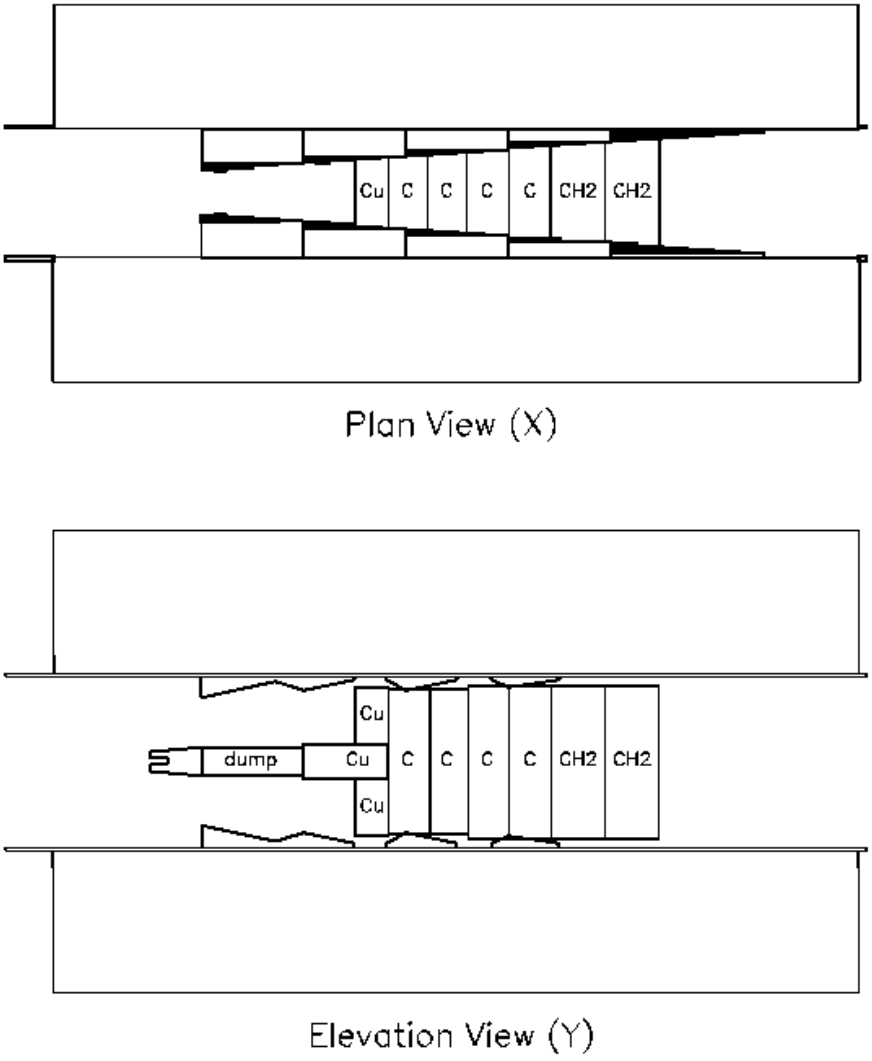

Figure 2.3: Side and elevation views of the absorbing wall and beam dump.

it through the absorbing wall.

2.5.1 Hodoscope Planes

Hodoscope planes were located at each of the four detector stations and were used to trigger on dimuon events. Each hodoscope plane was split into two half-planes of parallel scintillator paddles attached to photomultiplier tubes by plexiglass light guides. Stations 1, 3 and 4 each had two hodoscope planes, with their paddles oriented in the X and Y directions respectively. Station-2 had only one hodoscope plane, with its paddles oriented parallel to the floor. A vertical gap between the Y half-planes and the central X hodoscopes was inserted in order to avoid triggering on the high rate of beam-like muons from the decay of pions which were produced copiously in the dump. The design specifications of the hodoscope planes can be found in table 2.1. A more precise alignment of the hodoscopes was achieved by examining the distributions of positions of muon tracks at each hodoscope plane when a given hodoscope in that plane fired.

2.5.2 Drift Chambers

Each of the first three detector stations contained six drift-chamber planes, arranged in three pairs of planes with parallel wire orientations (referred to as "views"). Wires were oriented horizontally in the "Y" view, and at an angle of $+14^\circ$ and -14° with respect to the X axis in the "V" and "U" views, respec-

Table 2.1: Hodoscope specifications. Distances measured in inches.

detector	z position	# of counters	counter width	gap	Δx	Δy
Y1	769.78	16	2.5	0.38	47.50	40.75
X1	770.72	12	4.0	0.47	47.53	40.78
Y2	1114.94	16	3.0	0.66	64.625	48.625
X3	1822.00	12	8.68	1.0	105.18	92.00
Y3	1832.00	13	7.5	0.0	104.00	92.00
Y4	2035.50	14	8.0	0.0	116.00	100.00
X4	2131.12	16	7.125	0.0	126.00	114.00

tively. The wires in the second plane in each pair were offset by half the cell size of the drift chamber. The plane in each pair closest to the target was denoted as the "unprimed" plane, while the plane in the pair furthest from the target was denoted as the "primed" plane. These planes provide information on the X and Y intercept of the muon tracks at the detector station, with redundant information about the Y position.

The drift chambers were operated with a gas mixture of 49.7% argon, 49.6% ethane and 0.7% ethanol, mixed by volume at a constant temperature of 25°F. The anode wires at Station-1 were gold-plated tungsten wire. Stations 2 and 3 used silver-coated beryllium-copper wires as anodes. All of the anodes were 25 μm

in diameter. The cathode wires were all 62.5-μm silver-coated beryllium-copper wire. The drift chambers were operated at voltages between 1700 and 2200 volts. Typical drift velocities were $\approx$ 50 μm/ns. Drift chamber specifications can be found in table 2.2.

The signals from the drift chambers were read out by a fast amplifier and discriminator system. Single-hit time-to-digital converters (TDCs), which only record the first hit on the wire during an event, were used to measure the drift time. The combination of good hits together with their associated drift times in all three views result in a "triplet" hit in each station. The bank of the triplets was saved to provide information used later in reconstructing the muon tracks in the analysis.

2.5.3 Proportional Tubes

The detectors at station-4 provided both trigger-information and muon discrimination capabilities. Located downstream of the electromagnetic and hadronic calorimeters[3], station-4 consisted of two hodoscope planes (X4 and Y4) and three proportional-tube planes (PTY1, PTX and PTY2). Each of the proportional-tube planes had two layers of 1×1-inch cells. Adjacent layers were offset by half a cell to cover the dead region between adjacent cells. The proportional-tubes were

[3] The calorimeters were left over from a previous experiment. For E866, they were unnecessary and were only used to eliminate any hadrons which made it through the absorbing wall.

Table 2.2: Drift chamber specifications. Distances measured in inches.

detector	Z-position	# of wires	cell size	aperture(X×Y)	operating voltage
V1	724.69	200	0.25	48×40	+1700
V1′	724.94	200	0.25	48×40	+1700
Y1	740.81	160	0.25	48×40	+1700
Y1′	741.06	160	0.25	48×40	+1700
U1	755.48	200	0.25	48×40	+1700
U1′	755.73	200	0.25	48×40	+1700
V2	1083.40	160	0.388	66×51.2	−2000
V2′	1085.52	160	0.388	66×51.2	−2000
Y2	1093.21	128	0.40	66×51.2	−2000
Y2′	1095.33	128	0.40	66×51.2	−2000
U2	1103.25	160	0.388	66×51.2	−1950
U2′	1105.37	160	0.388	66×51.2	−1975
V3	1790.09	144	0.796	106×95.5	−2200
V3′	1792.84	144	0.796	106×95.5	−2150
Y3	1800.20	112	0.82	106×91.8	−2200
Y3′	1802.95	112	0.82	106×91.8	−2200
U3	1810.24	144	0.796	106×95.5	−2200
U3′	1812.99	144	0.796	106×95.5	−2200

Table 2.3: Proportional tube specifications. Distances measured in inches.

detector	Z-position	No.of wires	cell size	aperture X×Y
PTY1	2041.75	120	1.0	117×120
PTX	2135.875	135	1.0	135.4×121.5
PTY2	2200.75	143	1.0	141.5×143

operated using the same gas mixture used in the drift chambers. To reduce the probability of any hadrons making it through the calorimeters, a 3 foot wall of zinc and a 4 inch wall of lead were placed between the calorimeters and the station-4 detectors. Furthermore, 3 feet of concrete was placed between PTY1 and X4 and between PTX and PTY2. This provided a total of 16.6 hadronic-interaction lengths upstream of the Y4 plane. The only detectable particles which could reach the station-4 detectors were muons. Specifications of the proportional-tubes may be found in table 2.3.

2.6 Trigger

Despite the fact that the absorbing wall all but eliminated the rate of hadrons produced in the dump, the rates of single and dimuon events from both the target and dump were too large for the drift chambers to be read out on every muon which was detected. Therefore the information from the hodoscopes was used to

trigger on events which had the expected signature of a dimuon event originating in the target. The trigger was also configured to take prescaled samples of events which would be used later to reconstruct the combinatoric background.

The trigger system used in E866 was upgraded from that used for previous experiments [Gag 98]. The purpose of the upgrade was to increase the flexibility of the trigger, and to improve the acceptance of high p_T dimuon events. The main elements of the trigger system were the Trigger Matrix Modules and the Track Correlators. Figure 2.4 shows a diagram of the trigger electronics for the left hand side of the spectrometer.

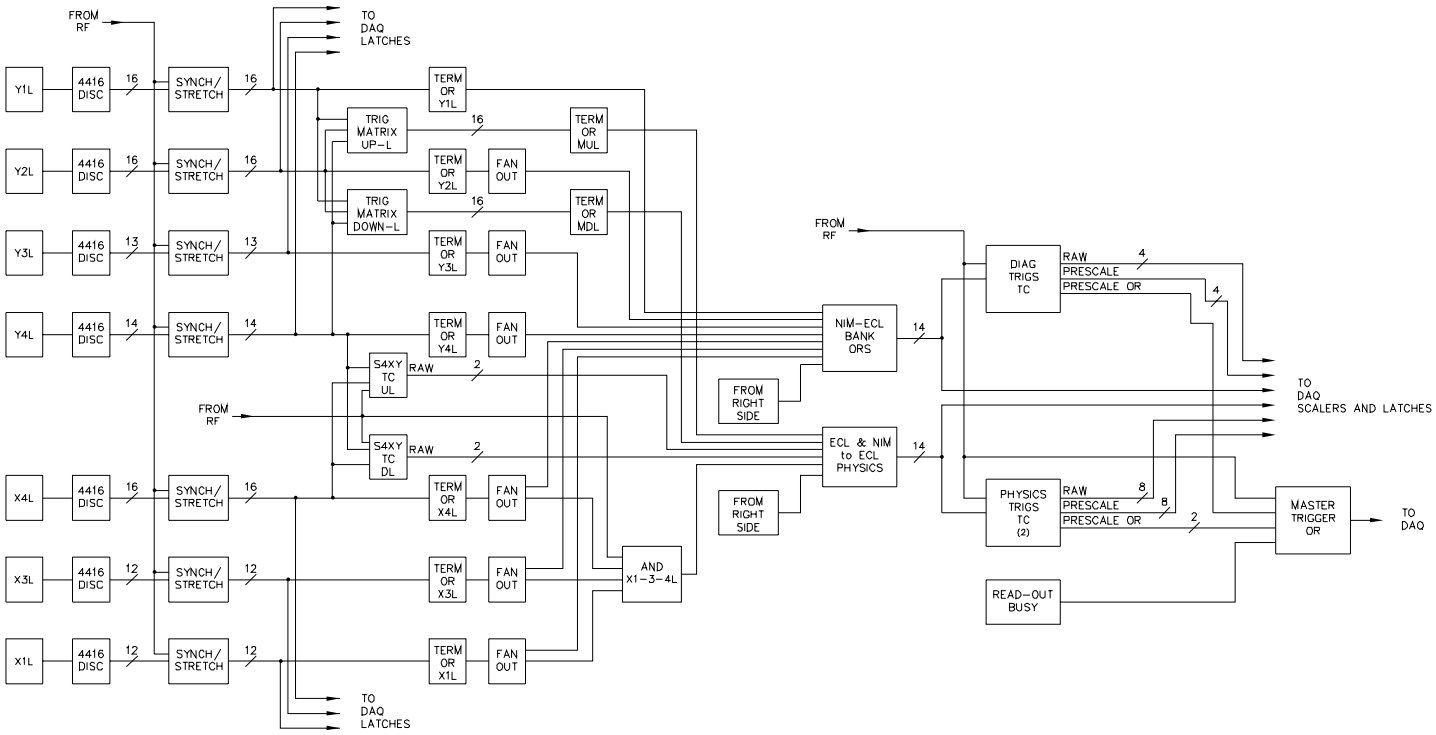

Figure 2.4: Block diagram of the E866 trigger. Only the inputs and electronics for the left side of the spectrometer are shown.

The Trigger Matrix Modules were responsible for determining whether a track was likely to be from a dimuon event which originated at the target. The outputs of the Y hodoscopes at stations 1, 2 and 4 were input into the Trigger Matrix Modules. The hit patterns registered by the hodoscopes were tested against a preselected set of hit patterns which corresponded to a muon from a dimuon event in the target traversing the spectrometer. These hit patterns where determined from Monte Carlo studies prior to the experiment. Some matrix elements had considerable rates of muons passing through them which actually originated in the dump. In order to take larger rates of target events, these matrix elements were turned off.

Four sets of Trigger Matrix Modules were used in the trigger system. These were referred to as matrix-up-left (MUL), matrix-down-left (MDL), matrix-up-right (MUR) and matrix-down-right (MDR). They corresponded to single muons on the left- or right-hand side of the spectrometer which went above or below the dump. These, along with the outputs of the Terminator/OR's and the Station-4 XY (S4XY) Track Correlators, were the inputs to the Track Correlators. The job of the Track Correlators was to filter the inputs and determine if a trigger should be fired and the event written to tape. There were three Track Correlators capable of triggering an event: Physics A, Physics B and Diagnostic.

Physics A (PhysA) was the main physics Track Correlator. Like all of the Track Correlators, it could handle four sets of trigger conditions. Table 2.4 shows

the triggers that were used in each of the data sets in this analysis. The triggers in each of the data sets performed the same functions. The PhysA1 trigger selected oppositely-charged muons which traversed opposite sides of the spectrometer, while the PhysA3 and PhysA4 triggers selected oppositely-charged muons which traversed the same side of the spectrometer. The PhysA2 trigger was the like-sign trigger. It selected same-sign muon pairs on opposite sides of the spectrometer.

In addition to the requirements on the charge and geometry of the muons applied by the matrix, the Track Correlators used in the low- and intermediate-mass data sets added constraints on the X and Y positions of the muons at station-4 (the S4xxx entries in the table.) These constraints were designed to veto events which populated areas where the dump dominated the event rate.

The Physics B (PhysB) track correlator was used to sample events which were used to monitor the efficiencies and systematics of the detector. An example of one of the many B triggers used in the experiment appears in table 2.5. The PhysB1 trigger was designed to read out any event with muons traveling along paths on opposite sides of the spectrometer, regardless of their relative sign. The PhysB2 trigger was often configured to trigger on events with a single muon traveling along one of the predetermined matrix roads that a muon in a dimuon event would follow. These data were used to extract the combinatoric background, as will be discussed later.

Table 2.4: Trigger configuration (PhysA). Configurations shown for the low-, intermediate- and high-mass data. The symbols "*", "+" and "!" correspond to logical AND, OR and NOT, respectively.

Mass Setting	Number	Prescale	Requirements
low	PhysA1	1	(MUL * MDR) + (MUR * MDL)
	PhysA2	4	(MUL * MUR) + (MDL * MDR)
	PhysA3	1	(MUL * MDL) * (S4UL2 * S4DL2)
	PhysA4	1	(MUR * MDR) * (S4UR2 * S4DR2)
int	PhysA1	1	((MUL * MDR) * (!S4DL1 + !S4UR1)) + ((MUR * MDL) * (!S4DR1 + !S4UL1))
	PhysA2	2,1	((MUL * MUR) * (!S4DL1 + !S4DR1)) + ((MDL * MDR) * (!S4UL1 + !S4UR1))
	PhysA3	1	((MUL * MDL) * (!S4UL1 + !S4DL1) * (S4UL2 * S4DL2))
	PhysA4	1	((MUR * MDR) * (!S4UR1 + !S4DR1) * (S4UR2 * S4DR2))
high	PhysA1	1	(MUL * MDR) + (MUR * MDL)
	PhysA2	4	(MUL * MUR) + (MDL * MDR)
	PhysA3	1	(MUL * MDL)
	PhysA4	1	(MUR * MDR)

Table 2.5: Trigger configuration (PhysB). An example of a PhysB trigger used in the high-mass data. The symbols "*", "+" and "!" correspond to logical AND, OR and NOT, respectively.

Mass Setting	Number	Prescale	Requirements
high	PhysB1	800	X134L * X134R
	PhysB2	1000	(MUL + MDL + MUR + MDR)
	PhysB3	-	-
	PhysB4	-	-

2.7 Data Acquisition System

The E866 data acquisition system (DAQ) was essentially an upgraded version of the system used in E789. The DAQ had three areas of responsibility: event readout, data archiving and online analysis. The backbone of the event readout was the Nevis Transport System. Upon receipt of a signal from one of the Track Correlators, a busy signal was raised which inhibited further triggers from being accepted. Simultaneously, the first word of the event was inserted onto the transport bus. Signals were sent to the TDC readouts on the drift chambers and the coincidence registers (CR's) on the hodoscopes. When signaled, the TDC's and CR's began digitizing their signals for insertion onto the bus. Each hodoscope and proportional-tube hit resulted in the insertion of an identifying word on the bus. The TDC's would also start a timer which would be terminated by the amplified

signal from the drift chamber. This provided a measurement of the drift time in the chamber, which was inserted onto the transport bus along with the number of the struck wire.

At this point, the data stream on the transport bus was fed into the Versa Module Eurocard (VME) based archiving system. During the 20s spill cycle, data were first transported to a pair of high-speed memory boards. Once one of the boards was full, it was drained into a large memory buffer while the other board was filled. Upon completion of the spill, the data were then formatted and sent down the VME pipeline to the tape archiving system. Here the data were written out to 8mm Exabyte tapes. Additionally, a fraction of the event data and all of the spill information (number of triggers fired, SEM counts, target position, etc...) were sent to the online monitoring systems.

The online monitoring system consisted of a database system interfaced to several graphical tools, and the E866 online analysis code. The database system allowed us to monitor the status of various components of the beamline and spectrometer. Graphical displays of the luminosity, magnet voltages, livetimes, etc..., gave an overall indication of the health of the spectrometer. The online analysis code analyzed the data that were sent to it via the VME pipeline. The histograms generated by the analysis code were accessible in real time by making use of PAW (Physics Analysis Workstation) [PAW] global sections. This allowed us to monitor the detector planes, watching for and correcting any inefficiencies

which might develop.

3 EVENT RECONSTRUCTION

By the time the experiment ended, approximately 250 GB of data had been recorded to tape. The data on these tapes represented the hits on each chamber and hodoscope plane for each event, the general characteristics of the beam in any given spill and the overall state of the spectrometer. The reconstruction of the kinematics of the events from these raw data required several steps. After configuring the analysis for the specific data set, the tracks were reconstructed from the chamber hits. Once the tracks had been found, their paths through the SM0 and SM12 magnets had to be reconstructed while accounting for energy loss and multiple scattering in the absorbing wall and beam dump. These procedures are outlined in greater detail below.

3.1 Data Sets

During the nine months starting in September 1996 in which FNAL E866/NuSea took data, over 360,000 continuum dimuon events were written to tape. These events were grouped into several sequentially numbered data sets which were differentiated by the polarities and currents used to energize the three spectrometer magnets. Each data set fell into one of three categories, defined by the mass range for which the spectrometer was optimized. These categories were referred to as the low-, intermediate- and high-mass data, corresponding to spectrometer

settings optimized for masses near the J/ψ, between the J/ψ and Υ masses, and near the Υ mass, respectively. Table 3.1 lists the data sets used in this analysis and the mass setting to which they belong. It also tabulates the currents used to power the spectrometer magnets, and whether the targets were filled with either the first or second sample of cryogenic liquids.

Table 3.1: Definition of the data sets. The SM3 magnet was operated at a single current of 4230 A, with the same polarity as the SM12 current.

mass setting	data set	SM0 current	SM12 current	target fill
low	5	-2100 A	2800 A	first
	10	2100 A	-2800 A	second
intermediate	9	0 A	2800 A	second
high	7	0 A	4000 A	first
	8	0 A	4000 A	second
	11	0 A	-4000 A	second

3.2 First Pass

Since only about $\sim 1\%$ of the events recorded to tape were due to a continuum dimuon event originating from the target, multiple analyses of the entire data sample were not feasible. It was therefore necessary to reduce this data sample to more manageable levels. A first pass analysis was performed which filtered out many

of the bad (non-dimuon) events in the data sample, while preserving almost all of the events we were interested in. The computing resources for this analysis were provided by the Fermilab Computing Division. A number of IBM workstations were linked together into four parallel computing clusters called "farms", which were able to process the complete data sample in approximately two months.

3.2.1 Track Reconstruction

The analysis began by reading in the configuration of the spectrometer from various files, some specified by the user and some loaded automatically based on the data set being analyzed. Once configured, the analysis code examined the hits in the drift chambers at stations 2 and 3 to find a set of candidate tracks. If four of the six planes in a station registered a hit, the position of that hit was considered a possible track reconstruction point. Points which were inconsistent with the trigger which fired were dropped. The remaining reconstruction points were iteratively combined to form track segments, so long as those segments were consistent with a single particle forming both points.

The track segments were then compared with hits in station 1 to reduce further the number of track segments. Each segment was first extended to the SM3 bend plane, located between stations 1 and 2. The charge and momentum of the particle was not yet known, so a window-of-interest at station 1 which pointed back to the target in the X direction was searched. If none of the hits at station 1 met the

search criteria, the track segment was discarded.

Once the track segment between stations 2 and 3 was connected with the station 1 reconstruction point (or points), the charge and momentum of the track were determined from the direction and size of the deflection of the track at SM3. The track segment was then extended back to station 4 to verify that it was indeed a muon. The concrete and lead shielding present at station 4 absorbed any hadrons and electrons which managed to penetrate the absorbing wall, but also caused any muons to multiple scatter. Since at this point the analysis knew the momentum of the track, a window consistent with the expected multiple scattering could be searched for hits in the five station 4 detectors. If the track fired less than three of the station 4 detectors, it was rejected on the grounds that it was not likely to be a muon.

3.2.2 Event Kinematics

At this point in the analysis, the charge, momenta and positions at the various detectors of the tracks in the event were known. It had also been determined at this point that each of the tracks was due to a muon. The tracks were then propagated back through the SM12 and SM0 magnetic fields, accounting for the energy lost in the hadronic absorbing wall and (if applicable) the dump. The paths of the tracks were reconstructed inside the magnetic field in 46-cm steps,

using field maps which had been measured prior to the experiment. A correction[1] was also made to compensate for the energy lost by the muon where the track passed through either the absorbing wall or the beam dump.

In addition to suffering energy loss inside the absorbing wall and dump, the muons also underwent multiple Coulomb scattering (MCS). The correction for this began by reconstructing the track back to an effective scattering bend plane (ZSCPLN) and recording its position and momentum there. The track was then completely analyzed, noting the deviations in X and Y from the nominal target center. A correction to the momentum vector at the ZSCPLN was calculated from these deviations, and the reconstruction of the track repeated from that point. This procedure was iterated until the track converged on the nominal center of the target.

The production of pions and other hadrons in the target contributed to a large rate of single muons in the spectrometer as they decayed between the target and dump. A significant fraction of these muons followed a beam-like trajectory through the dump and absorbing wall. Because there was no way to differentiate between one of these single muons and a muon which was a part of a valid dimuon event, these muons could cause ambiguities in the analysis that could not be resolved. To prevent this from happening, muons which passed through a 10.2 cm

[1]The most probable energy lost in a given section of absorbing wall or dump was parameterized versus the momentum of the track. This energy loss parameterization was used to estimate the energy lost by the muon.

horizontal band centered on the nominal beam position at the dump were eliminated from the event sample.

After the kinematics of the individual tracks were reconstructed at the target, they were combined to form dimuon pairs. Less than 0.08% of the reconstructed events contained more than two tracks. From the charge of the tracks and their momenta, the kinematics of the event were determined. Events which reconstructed to a mass $< 2.0\,\mathrm{GeV}$ were rejected on the grounds that the acceptance for such pairs arising from the target was zero[2]. Events whose uniterated vertex[3] indicated they were unlikely to have originated in the target were also cut. This cut was realized in terms of the z-coordinate of the uniterated vertex (ZUNIN), which was restricted to values less than 350 inches from the center of the target.

3.3 Second Pass

The goal of the first pass analysis was to reduce the data sample to a more manageable level. The purpose of the second-pass analysis was to reconstruct the kinematics of the events as accurately as possible, minimizing any systematic errors which would affect the cross sections. In the remainder of this chapter, we

[2] There was a problem in the application of this cut which applied to events with more than two tracks. If one of the pairs which could be combined from the tracks in the event was below the mass cut, the entire event was cut rather than the particular combination of tracks. Studies indicate that the error introduced by this is on the order of 0.1%, which is negligible compared to other uncertainties in the experiment.

[3] The position at which the tracks made their closest approach before the MCS corrections were made.

will discuss the differences between the algorithms the first- and second-pass analyses used to correct for multiple scattering and energy loss. We will also outline the procedures used to determine the strengths of the fields in the spectrometer magnets, and the position and angles of the beam at the target.

3.3.1 Multiple Scattering

The ZSCPLN was used to correct for the multiple scattering that the muons underwent in traversing the absorbing wall and beam dump as described above. The first pass-analysis used a single position for the ZSCPLN, which was empirically determined by minimizing the correlation between the mass of the dimuon pair and the mean ZUNIN. This approach ignored the additional scattering that events which passed through the dump were subject to. The second-pass analysis based the position of the ZSCPLN on the length of the dump which the muon penetrated. It was found that for every 1 cm the track traveled through the dump, the ZSCPLN should be moved upstream 0.7 cm.

The second pass analysis also employed a different technique for finding the optimal position of the ZSCPLN. Monte Carlo studies indicated that the correlation between the mass of the events and ZUNIN was due to energy loss fluctuations in the beam dump and hadronic absorber, rather than difficulties in reconstructing the track angles as had previously been believed. The ZSCPLN in the second-pass analysis was placed at the position which optimized the reconstruction of the

track angles at the target for Monte Carlo events. This resulted in a ZSCPLN located 12 m downstream of the target, near the end of the carbon section of the hadron absorber. The method used in the first pass analysis placed the ZSCPLN 22 m downstream of the target, well outside of the absorbing wall.

3.3.2 Energy Loss

As will be discussed below, determination of the strength of the magnetic fields from the data relied on an accurate reconstruction of the masses of the J/ψ and Υ resonances, and the ZUNIN distribution of the events. Deviations between the average energy lost by the muons and the parameterization used to correct for the energy loss in the analysis could cause systematic shifts in both mass and z-vertex reconstruction, and thus the measurement of the magnetic fields.

Every muon which passed through the spectrometer was subject to a large amount of energy loss in the absorbing wall and possibly the beam dump. A typical 200 GeV muon lost on average $\sim$ 2 GeV in the absorber. Figures 3.1 and 3.2 show the energy lost in traversing the beam dump and absorbing wall for muons with different incident momenta. The calculations were performed using the TRAMU muon transport program [Gin 86]. The large, non-Gaussian tail skews the mean to much larger energy losses than the most probable value. It was important to parameterize the energy loss in the reconstruction of the data with emphasis on accurate (on average) reconstruction of the kinematics of the

events rather than optimal resolution. Thus, the mean energy loss was used in this analysis.

Given the incident momentum of the muons on a specified material, the parameterization of the mean energy loss is a well defined problem. However, the incident momentum of the muons on the absorbing wall or dump was the quantity which we wished to estimate from our measurement of the momentum downstream of SM12 and some parameterization of the random distribution of energy loss inside the absorbing wall and dump. To further complicate the problem, muons which lost a large amount of momentum in the dump/absorber could be swept out of the acceptance. Muons with lower incident momenta would be more susceptible to this, introducing an acceptance effect into the parameterization of the energy loss.

Figure 3.3 shows the mean energy lost by muons in the $24''$ section of the absorbing wall according to the Monte Carlo (where we knew the energy lost by each muon thrown). We plot the mean energy loss versus the momentum incident upon the $24''$ of copper, and versus the momentum after the $24''$ of copper. The "after" parameterization is generally flatter than the "incident" parameterization. This is due to the fact that larger mean energy losses in the "incident" parameterization will be shifted to smaller values of p_{after}. It should be clear from the figure that this effect is important, especially at lower momenta where we have most of our statistics in the data.

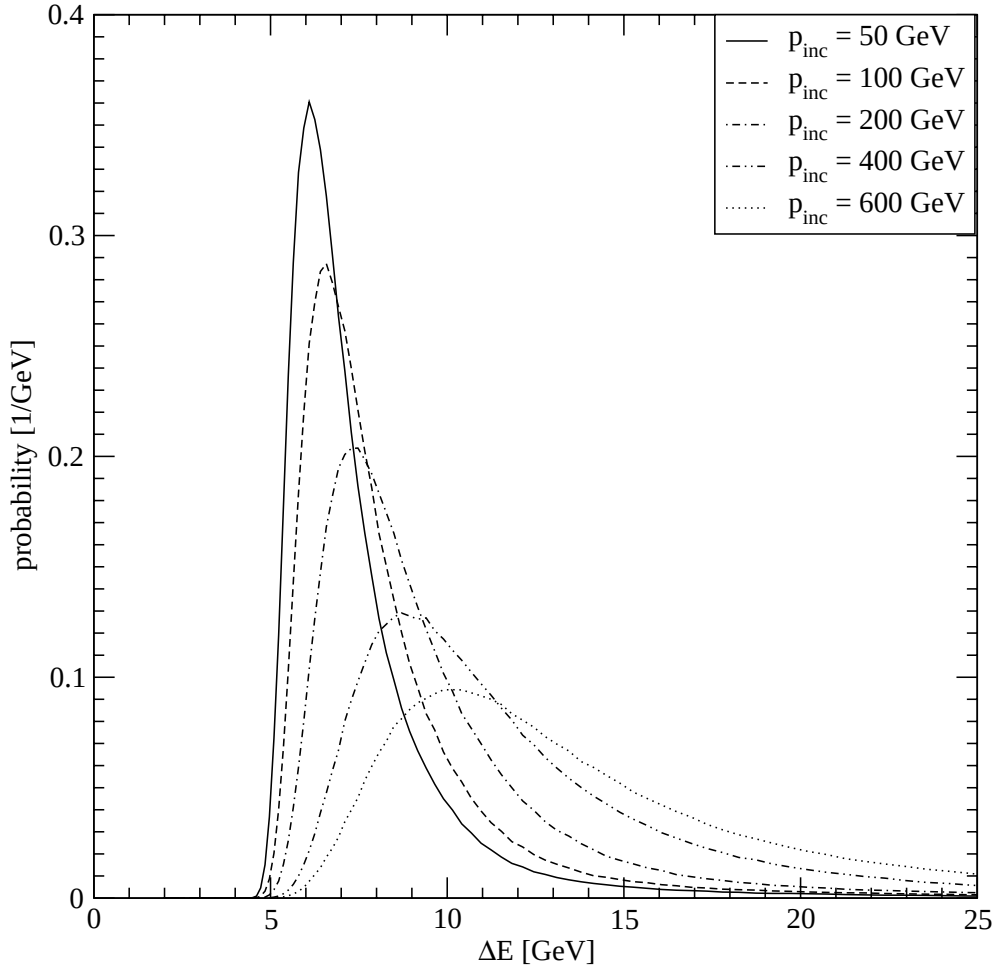

Figure 3.1: Energy loss distributions for muons passing through 144" of Cu (beam dump) for various incident energies.

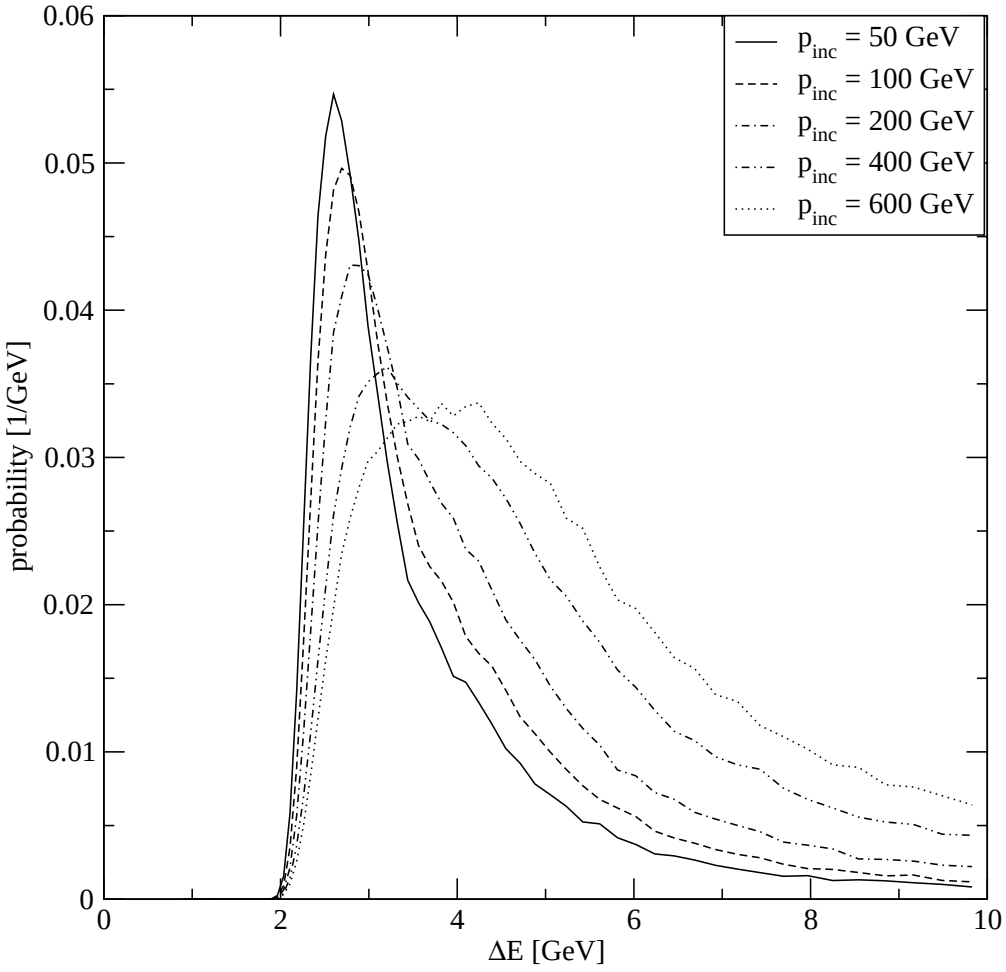

Figure 3.2: Energy loss distributions for muons passing through the entire absorbing wall – including the copper, graphite and polyethylene sections – for various incident energies.

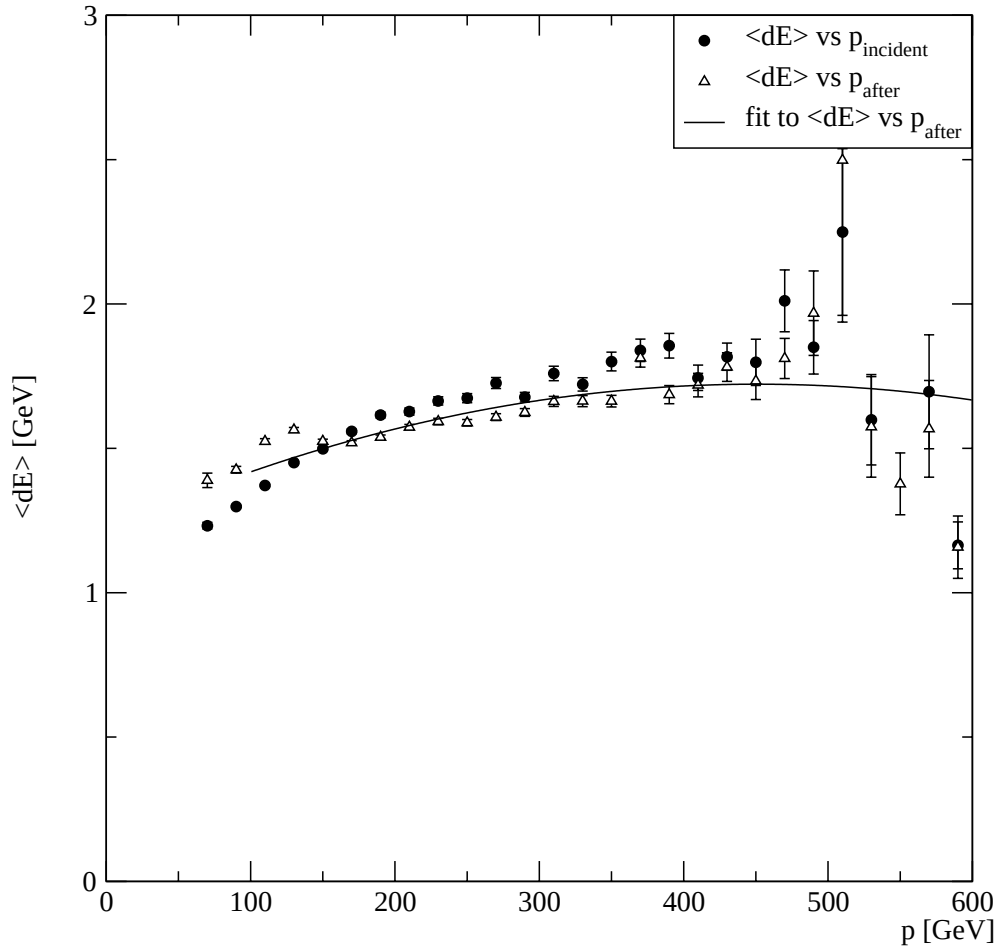

Figure 3.3: Mean energy loss for muons in the 24″ Cu section of the absorbing wall. Shown is the energy loss versus the momentum of the muon entering the section (circles) and the energy loss versus the momentum of the muon exiting the section (triangles). The solid line is the fit to the second set of points which was used in reconstructing the events.

Figure 3.3 also shows the fit to the energy loss in the 24″ copper section of the absorbing wall. The parameterizations which we used for all of the absorber sections in the high-mass data are given by

$$dE_{Cu} = 1.2202 + 0.2228 \times 10^{-2} p_{\text{after}} - 0.2472 \times 10^{-5} p_{\text{after}}^2$$

$$dE_{C} = 0.2461 + 0.3135 \times 10^{-3} p_{\text{after}} - 0.4362 \times 10^{-6} p_{\text{after}}^2$$

$$dE_{CH_2} = 0.1857 + 0.2073 \times 10^{-3} p_{\text{after}} - 0.3501 \times 10^{-6} p_{\text{after}}^2$$

where p_{after} is the momentum immediately downstream of the absorbing wall section being traced through. Deviations in the shape of this parameterization, but not intercept, were found for the low- and intermediate-mass data sets. When used to reconstruct Monte Carlo events, systematic shifts in the masses and ZUNIN of the events are held to acceptable levels.

3.3.3 Magnetic Fields

The magnetic fields in the three spectrometer magnets were measured prior to the installation of the absorbing wall. Measurements were made at each of the planned operating currents, except for the 4000 A setting of the SM12 magnet. This setting was not measured due to concerns over the structural integrity of certain parts of the magnet under the increased strain of higher magnetic forces. At the time, it was anticipated that the 2800 A setting of the SM12 field would be the largest current at which that magnet would be operated. Later during the experiment, the SM12 magnet was successfully operated at the 4000 A setting,

providing the largest and cleanest sample of continuum dimuon events in the E866 data sample.

The magnet map used in the high-mass data utilized a measurement of the SM12 field from a previous experiment. However, the upstream portion of the magnet was reconfigured for E866. This region of the magnet map relied on an OPERA [Ope 94] calculation of the magnetic field, matched to the field map in the known region of the magnet. A similar procedure had to be performed to determine the magnetic fields in the beam dump, where it was not possible to measure the fields.

Although the shapes of the magnetic fields were well determined, the absolute strengths of the fields were uncertain at the $\sim 1\%$ level. Monte Carlo studies indicated that this level of uncertainty in the SM0 and SM12 magnets could be a significant source of uncertainty in the acceptance of the spectrometer, especially near its low mass edge. Figure 3.4 shows the ratio of Monte Carlo events generated with magnetic fields differing by 5% using a fast version of the E866 Monte Carlo. The relative acceptance falls by nearly 40% over the given mass range. A systematic uncertainty of $\sim 1\%$ in the SM12 field would correspond to a $\sim 8\%$ point-to-point systematic uncertainty in the acceptance, which would have been unacceptable given the precision of our data. Furthermore, systematic shifts in the SM3 field would cause systematic shifts in the reconstructed kinematics of the events. Such shifts were a problem, considering the steeply-falling nature of the

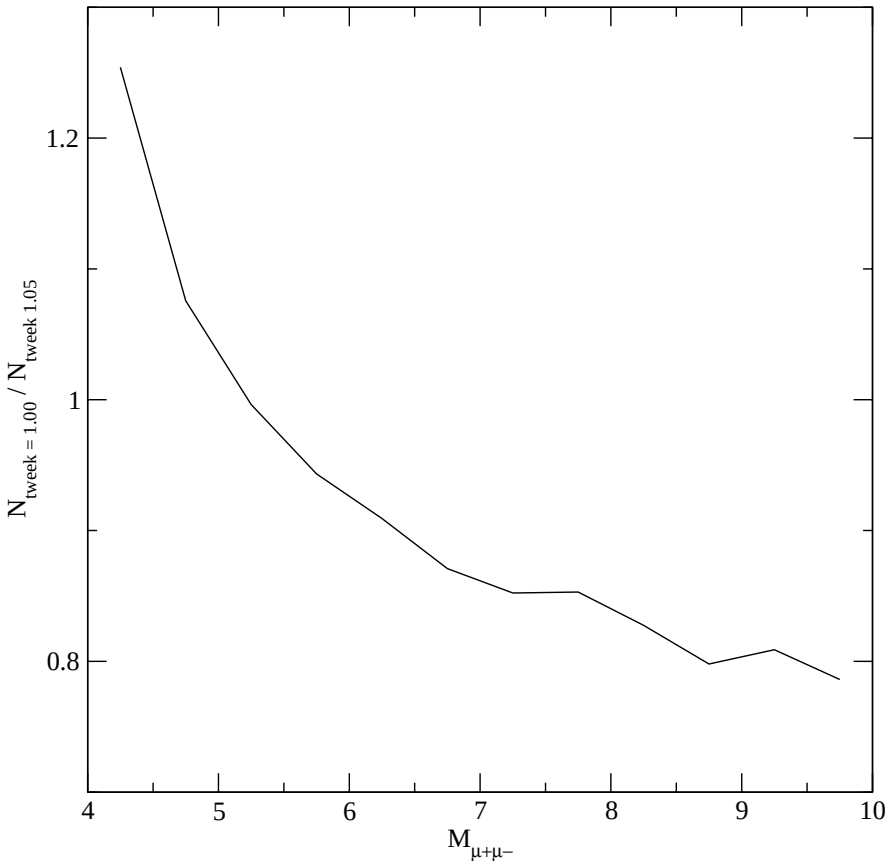

Figure 3.4: Ratio of Monte Carlo events generated with the nominal SM12 field to those generated with the SM12 field augmented by 5%. The ratio is shown for $0.5 \leq x_F < 0.55$.

cross section we were trying to measure.

The general procedure for determining the absolute field strengths from the data, once the impact of the energy loss parameterization had been limited, was as follows. We began by fitting the masses of any resonances (J/ψ, Υ) in the mass spectrum to a Gaussian plus a quadratic background, noting the reconstructed mass of the peaks. We also estimated the mean of the ZUNIN distribution. Deviations of these quantities from the nominal position of the target and the published

resonance masses indicated an incorrect value for the SM12 and SM3 fields respectively. The data set was then re-analyzed with a multiplicative constant – referred to as a tweek (*sic.*) – applied to each of the magnetic fields to try to compensate. This was performed iteratively until the resonance masses converged to their published values, and ZUNIN was centered on the nominal target position.

The procedure outlined above was essentially the procedure used to determine the tweeks on the SM12 and SM3 magnets in the high-mass data. It is a slight simplification, since a shift in the SM3 magnet would also have caused a shift in the ZUNIN of the events due to the increased momentum and resulting decrease in the deflection of the muon by SM12. The one important change to note was that only events which missed the dump were studied. Muons which hit the dump went through a somewhat uncertain amount of material, contributing an uncertainty to the amount of energy loss which should have been corrected for. Additionally, the ZUNIN of the events with one track in the dump was largely determined by the other track in the event. This reduced the sensitivity of ZUNIN to the magnetic field in SM12.

Additional problems arose in the analysis of the low and intermediate mass data sets. In the intermediate-mass data set, we had only a limited number of events to work with. The reconstructed Υ mass, the only resonance available in that data set, was too uncertain to provide an accurate assessment of the SM3 tweek. Therefore, the value found in the high mass analysis was used for SM3,

and the usual procedure of finding the SM12 tweek using the ZUNIN distribution performed.

A similar problem occurred in the low-mass data set, where we had an extra magnetic field (SM0) to worry about. In principle, since we could resolve both the J/ψ and ψ' resonances, we had the extra information needed to tune the SM0 field. In practice, the ψ' mass was relatively insensitive to the SM3 field, for a reasonable set of tweeks. Once again, the SM3 field tweek from the high-mass data was used in this data set. The SM0 tweek was found from the fits to the J/ψ mass, and the usual ZUNIN fitting procedure used to extract the SM12 tweek.

The procedures described above provided an estimate of the average field strength in a given data set. It also provided a way to estimate the systematic uncertainties on the tweeks by studying the impact of a given change in tweek on the ZUNIN distribution and the resonance masses. Uncertainties in the mass and vertex fits could then be translated into uncertainties in the magnetic fields. Once the uncertainties in the magnetic fields were determined, the corresponding acceptance uncertainty could be calculated by running the Monte Carlo using different input fields. We will describe this in greater detail in the next chapter.

Figure 3.5 shows the J/ψ and Υ mass regions from the low- and high-mass data, when reconstructed using the optimal magnetic field tweeks. The reconstructed J/ψ and Υ masses of 3.095 and 9.461 GeV compare quite well with the published values of 3.097 and 9.46 GeV [Gro 00]. The intrinsic widths of the res-

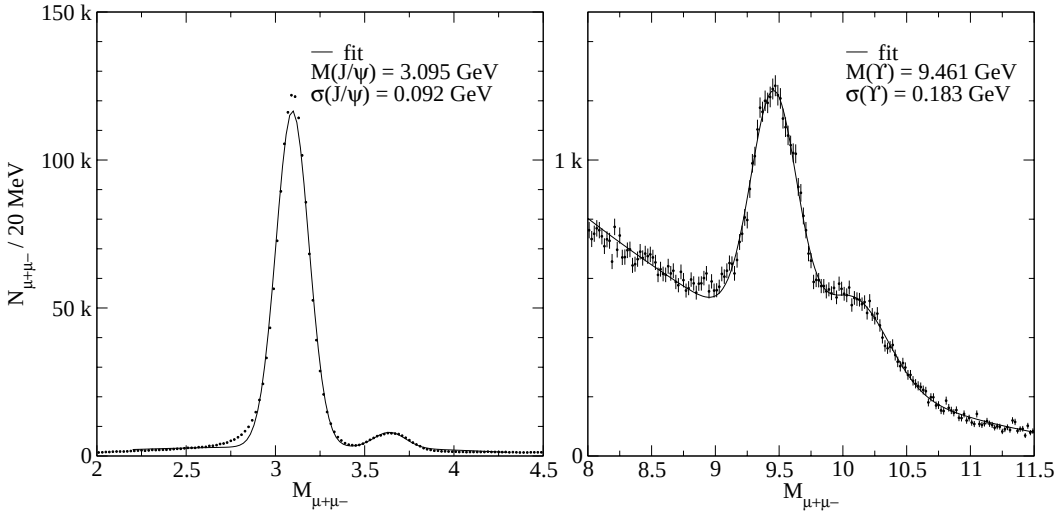

Figure 3.5: Reconstructed masses of the J/ψ and Υ resonance for the low- and high-mass data sets. Data from both targets are included.

onances (which are best expressed in keV), are smeared out by energy loss and multiple scattering in the absorbing wall and dump – our mass resolution is 92 MeV at the J/ψ mass and 183 MeV near the Υ. Figure 3.6 shows a fit to the ZUNIN distribution of the continuum dimuon regions, where the data has been summed over all data sets. In practice, fits to the ZUNIN distributions and resonance regions were performed separately in each data set. The deviations of the fits from their expected values amount to uncertainties of only $\pm 0.10\%$ and $\pm 0.15\%$ in the SM0/12 and SM3 tweeks, respectively.

One other source of systematic error in the tweeks was uncovered using the Monte Carlo. When Monte Carlo events were retracked through the reconstruction algorithm, the momentum found at the SM3 bend plane was $\sim 0.06\%$ larger than that which was actually generated by the Monte Carlo. Thus, the correct

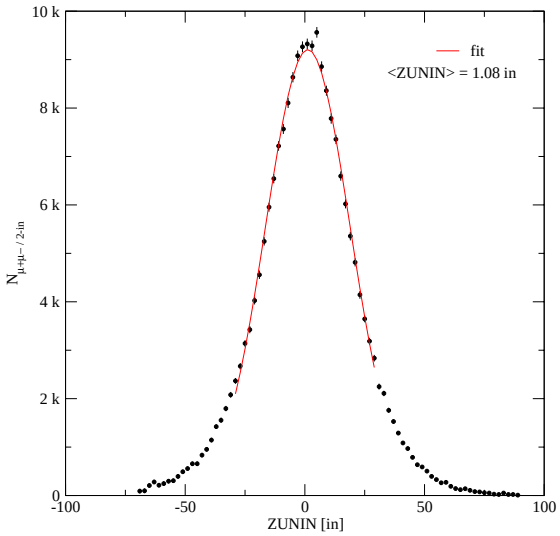

Figure 3.6: Distribution of empty-target-background subtracted events vs the uniterated z-vertex (ZUNIN), summed over both targets and all data sets.

field tweeks were subject to a small offset which had to be accounted for to obtain a more accurate simulation of the spectrometer. The origin of this effect was unclear. It may have been due to slight differences between the actual and simulated geometry of the apparatus, resolution effects coupled to the single bend plane approximation used for SM3, or some combination of these and other issues. This additional source of systematic uncertainty in the SM3 field does not contribute significantly to the overall size of the systematic uncertainties in the acceptance.

In table 3.2 we list the tweeks found for each mass setting using the previously described procedures. Studies of the stability of the mean ZUNIN and Υ masses versus data set and run number in the high-mass data suggest that a single value for the SM3 field tweek is reasonable. These studies also indicated that the SM12 field was reliably stable, and a single value was used for each data set within a

Table 3.2: Field strengths for each data set.

Mass setting	Data set	SM0 tweek	SM12 tweek	SM3 tweek
low	5	1.0140 ± 0.0010	1.0068 ± 0.0010	1.0049 ± 0.0015
	10	1.0140 ± 0.0010	1.0068 ± 0.0010	1.0049 ± 0.0015
int	9	N/A	1.0093 ± 0.0010	1.0049 ± 0.0015
high	7	N/A	0.9865 ± 0.0010	1.0049 ± 0.0015
	8	N/A	0.9865 ± 0.0010	1.0049 ± 0.0015
	11	N/A	0.9865 ± 0.0010	1.0049 ± 0.0015

given mass setting.

3.3.4 Beam Position and Angles

The position of the beam was determined by fitting the distribution of the x and y vertices of the raw data at the target position. The uniterated x and y positions of the two tracks in the event were averaged together to yield the x and y vertices. Run-to-run variations in beam position were found to be negligible for our purposes.

The beam angle was found through an iterative process involving the Monte Carlo. In principle, the Y component (and similarly the X component) of the beam angle could be found from just the data by looking at the muon momentum

vectors $\theta_y^{dimuon} = (p_y^+ + p_y^-)/(p^+ + p^-)$. However, asymmetries in the dump cut in the first pass analysis limited the accuracy of this technique. An independent test of the validity of the beam angle extracted from the data was to check the ϕ_p distribution in the data against that of the Monte Carlo. Since we know that the ϕ_p distribution must be isotropic, and having generated an isotropic distribution in the Monte Carlo, any difference between the distribution in the data versus the Monte Carlo could only result from a difference in the beam angle between the experiment and the Monte Carlo. The beam angles were improved by minimizing these differences, and we estimate that the uncertainty in the beam angle contributes no more than 5% (~ 0.7 GeV) of the transverse momentum of an average event.

4 ANALYSIS

The differential cross section is defined as the number of interactions per target particle leading to an event with kinematics between Ω and $\Omega + \delta\Omega$ per number of incident particles per unit area. We express this as

$$\frac{d\sigma}{d\Omega} = \frac{N/\Delta\Omega}{N_T(\bar{N}_i/A)}. \tag{4.1}$$

where N is the number of dimuon events from the target, N_T the number of target particles in the path of the beam, $\bar{N}_i$ the mean number of protons incident on the target and A the cross sectional area of the beam.

The simple expression in equation 4.1 is somewhat misleading, since we did not measure the number of *pp* and *pd* interactions which led to a dimuon event directly. Instead, we measured the yields of oppositely charged muon pairs from the interaction of a proton beam with target flasks containing liquid H_2 and D_2. These yields were subject to contamination by background events originating from the interaction of the beam with the SWIC and the front and back faces of the target flasks, and from the random coincidence of two uncorrelated muons produced in the same beam bucket. The yields were also subject to losses due to the acceptance of the spectrometer and inefficiencies in the detection of the muons. Equation 4.1 also relies on quantities such as the number of target particles and incident protons, which were also not directly measured, and the cross sectional area of the beam, which was not measured with any great precision.

Fortunately, we can rewrite equation 4.1 entirely in terms of quantities which were directly measured, while eliminating terms which were not measured well. We define the number of dimuons, corrected for backgrounds, as $N_{\mu^+\mu^-}$. This can be related to the number of interactions in equation 4.1 by

$$N = \frac{N_{\mu^+\mu^-}}{\alpha\epsilon} = \frac{N^{\text{target}}_{\mu^+\mu^-} - N^{\text{background}}_{\mu^+\mu^-}}{\alpha\epsilon} \tag{4.2}$$

where α is the geometric acceptance of the spectrometer, defined as the probability that both tracks in a given event would traverse all of the active detector elements of the spectrometer and survive all data cuts, ϵ is the efficiency with which the given event was detected, and the "target" and "background" superscripts refer to events which originated in the liquid target and background events respectively. The number of target particles can be expressed in the usual way:

$$N_T = N_A \, \rho \, L \, A \tag{4.3}$$

where N_A is Avogadro's number, ρ is the density of cryogenic liquid, L is the length of the target, and A is the cross sectional area of the beam.

To get the mean number of incident protons, we need to average over the attenuated flux in the target. The number of protons at any point along the length z of the target can be expressed in terms of the incident number of protons and the hadronic absorption length λ, as

$$N_i(z) = N_p e^{-z/\lambda}. \tag{4.4}$$

Averaging over the total length of the target L yields

$$\bar{N}_i = \frac{1}{L}\int_0^L N_i(z)\,dz = \frac{N_p\lambda}{L}(1 - e^{-L/\lambda}). \tag{4.5}$$

Substituting equations 4.2-4.5 into equation 4.1 results in an expression for the differential cross section:

$$\frac{d\sigma}{d\Omega} = \frac{N_{\mu^+\mu^-}}{\mathcal{L}\alpha\epsilon\Delta\Omega}, \tag{4.6}$$

where we have grouped several of the factors in the denominator into a single quantity, called the luminosity, given by

$$\mathcal{L} = N_A\rho\lambda(1 - e^{-L/\lambda})N_p. \tag{4.7}$$

We will now explain in detail how each of the quantities in equation 4.6 was determined.

4.1 Event Yields

The total event sample produced by the second pass analysis contained several questionable events. These included backgrounds from uncorrelated muon pairs and correlated pairs originating outside of the target volume, events which were reconstructed by the analysis but were not responsible for the trigger which caused the DAQ to read out, and events which occupied regions of the spectrometer which complicated the reconstruction of their kinematics. These events were either filtered out of the second pass event sample, or independently binned and subtracted

from it, to obtain the event yields used to calculate the cross sections. The same set of cuts were used on the Monte Carlo events used to calculate the acceptance. Simulations showed that contributions from the interactions of secondary hadrons produced in the target were negligible.

In order to avoid the J/ψ and Υ resonances, we selected events within the mass range $4.2 \leq M_{\mu^+\mu^-} \leq 8.7$ GeV, and events with masses $M > 10.85$ GeV. As the acceptance above the Υ resonance was quite small in the low and intermediate mass data sets, we only used the high mass data in that region. Due to uncertainties in the magnetic fields, data from the intermediate mass setting below 6.2 GeV were also discarded. Figure 4.1 shows the total E866 mass spectrum, with the contributions from the low-, intermediate- and high-mass data sets in their respective allowed mass ranges. The resonance regions have been retained, but all other cuts were applied. The number of events surviving all cuts is shown in table 4.1.

4.1.1 Target Flask Background

One of the larger sources of contamination was due to the beam interacting with the SWIC ($\approx$ 188 cm upstream of the target) and the walls of the target flasks which contained the cryogenic liquids. Figure 4.2 shows the yields from the cryogenic liquid and empty target flasks plotted versus ZUNIN. The SWIC is clearly visible in the empty target distributions, and much of the contamination was re-

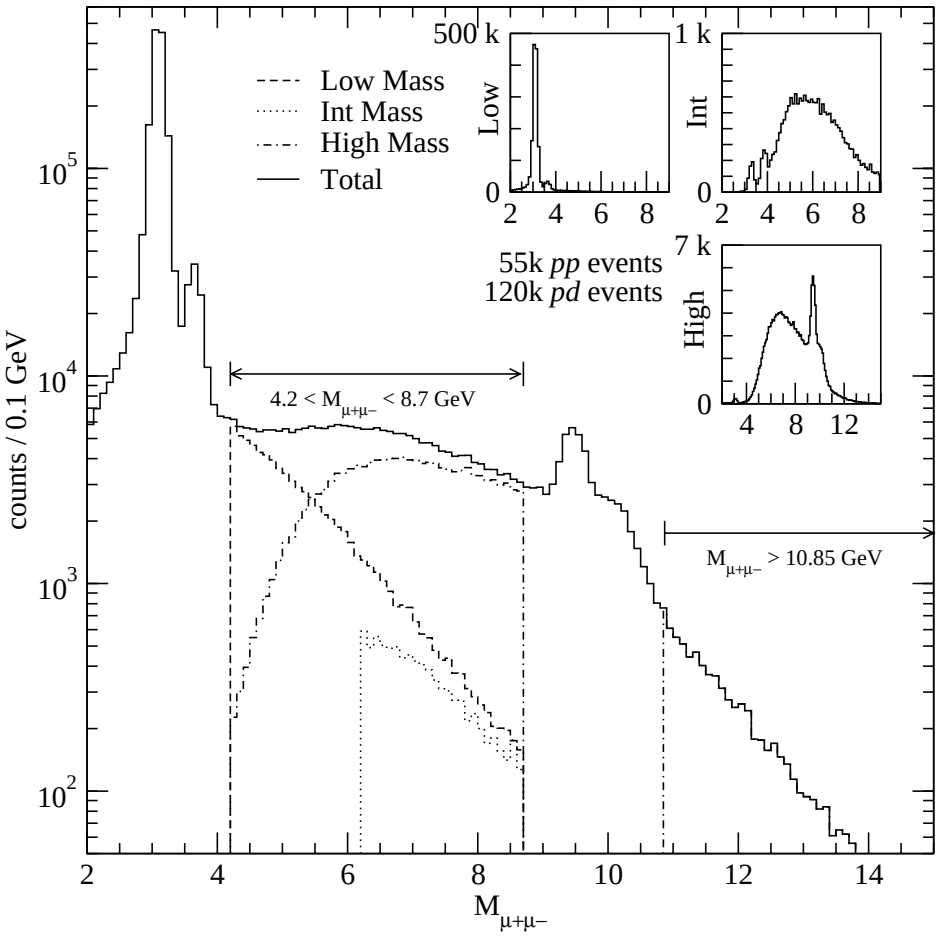

Figure 4.1: Total E866 mass spectrum surviving all cuts. The contribution of the low, intermediate and high mass data sets superimposed in their respective allowed mass ranges. Inset figures show the low, intermediate and high mass data sets on a linear scale over their entire mass range.

Table 4.1: Number of events in each data set which survived all data cuts.

Set	H_2 target	D_2 target	Empty target
5	17217	36962	699
7	9548	21030	425
8	20049	44129	1007
9	1768	4966	63
10	1658	3509	60
11	4850	10545	230
total	55090	121241	2484

moved by simply applying cuts (ZUNIN $> -50''$ in the low mass data, and ZUNIN $> -60''$ in the intermediate and high mass data). Events with ZUNIN $> 60''$ in the low mass data, and ZUNIN $> 90''$ in the intermediate and high mass data were also rejected, as they were likely to have originated in material downstream of the target.

The remaining background from the target flask was measured during the experiment, allowing us to subtract it from our event yields. A correction was made to the empty target yields based on the uniterated z-vertex of the event to account for the $\approx 7\%$ and $\approx 14\%$ attenuation of the beam between the front and back end caps of the flasks containing liquid hydrogen and liquid deuterium. This

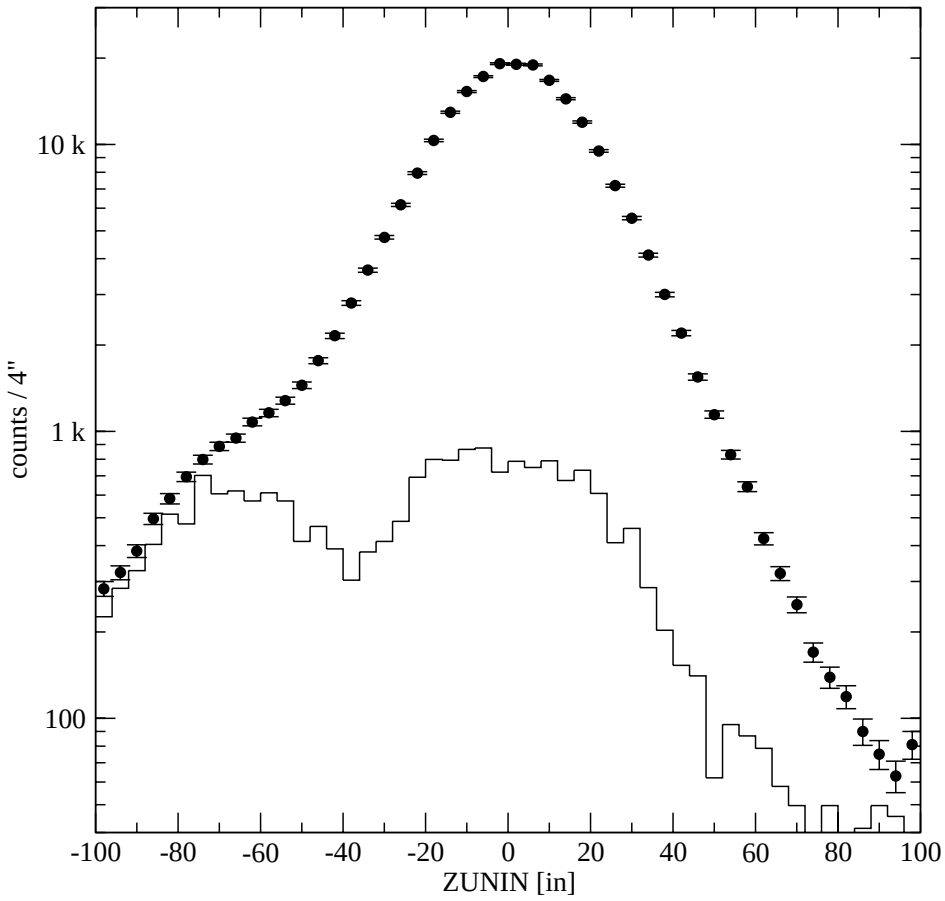

Figure 4.2: Comparison of ZUNIN distributions from the sum of the liquid hydrogen and deuterium targets (circles) to the contribution from the empty target (histogram), as calculated for deuterium.

correction was given by

$$N_{\mu^+\mu^-}^{empty} = \begin{cases} N_{empty} \times e^{-L/\lambda}, & \text{if ZUNIN} > 0 \\ \\ N_{empty}, & \text{if ZUNIN} < 0 \end{cases} \tag{4.8}$$

where we corrected events which appeared to come from downstream of the nominal target position $z > 0$ by the attenuation of the cryogenic liquid appropriate to the target.

4.1.2 Combinatoric Background

Another important background source was the random coincidence of oppositely charged, uncorrelated muons produced in the target in the same beam bucket. The numbers and kinematic distributions of these random events were estimated using event samples triggered on the like-sign (PhysA2) and single-muon (PhysB2) triggers. These random events were typically confined to masses below 5 to 6 GeV and were only important in the low- and intermediate-mass data sets, the latter being a non-issue due to the 6-GeV cut in the intermediate mass.

The single-muon trigger was used to trigger on what appeared to be single muons from the target traversing one of the matrix elements. Due to the high rate of such events from the target, these triggers were prescaled when in use during normal run conditions. Single-muon event samples were taken either during the normal course of the data collection or in special low-intensity runs. The resulting event samples were subjected to the same analysis chain as the opposite-sign data.

The single muons were then randomly combined with other single muons to form an uncorrelated dimuon event. This produced a sample of random dimuon events which, when properly normalized, could be subtracted from the data sample. Figure 4.3 compares the total dimuon yield in the data (summed over both targets and the high and low mass data sets) to the combinatoric background. The low mass data set contributes the largest contamination – approximately 5% of its total yield was due to randoms.

The normalization of the randoms was accomplished by comparing a subset of the randoms (those with two muons with the same charge), to events which satisfied the like-sign trigger in the data. These like-sign events were analyzed in the same way as any other event, except that one of the tracks was reflected about $y = 0$ when the kinematics of the events were calculated. Figure 4.4 shows the real like-sign events compared to the combinatoric like-sign events, scaled to match the real like-signs.

4.1.3 Trigger Cuts

For any given event, the possibility existed that the muons which fired the trigger and resulted in the event being read out by the DAQ were not the same muons which were reconstructed by the analysis. The easiest way for this to occur was to have a single, beam-like muon fire a set of hodoscopes, one of which was outside of the matrix, while simultaneously a second, low-momentum muon fired the missing

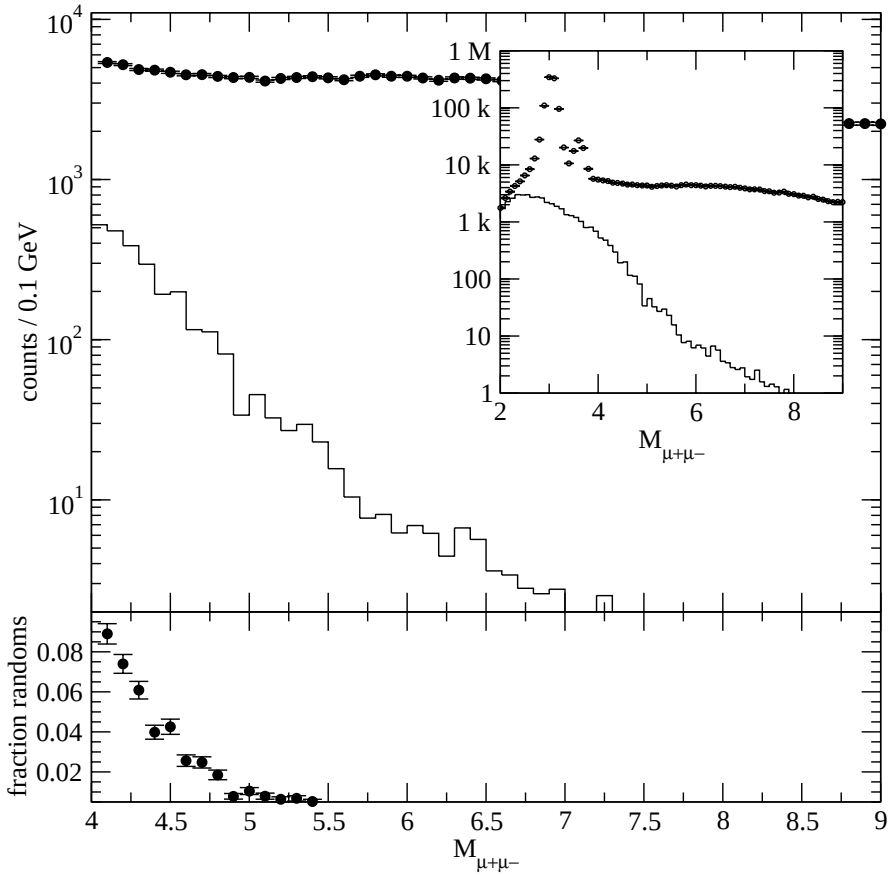

Figure 4.3: Comparison of the total E866 dimuon yield (dots) to the combinatoric background (histogram). The top panel shows the unsubtracted mass distributions, with the inset showing the same distributions down to 2 GeV. The bottom panel shows the fractional contribution of randoms vs. mass.

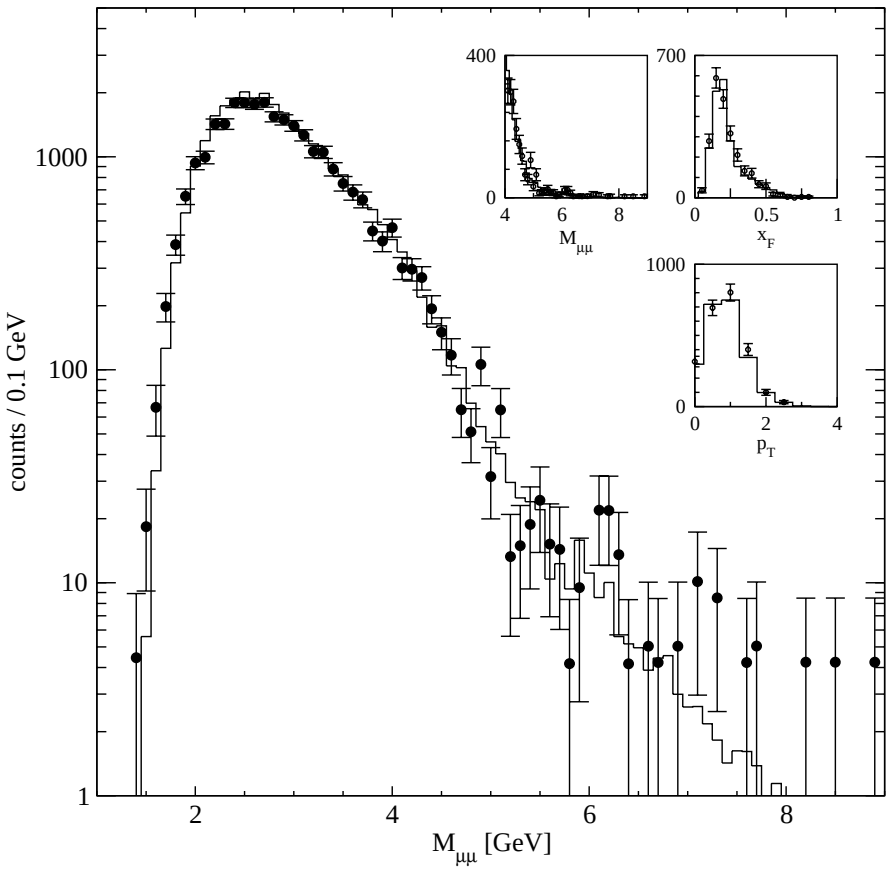

Figure 4.4: Comparison of like-sign distributions measured in the data (dots) to the like-sign distributions measured using the specialized trigger discussed in the text (histogram). The data and combinatoric like-signs are summed over the low and high mass data sets and both targets. The inset figures show the mass, x_F and p_T like-sign distributions over the mass range used in this analysis.

matrix element. When combined with a second, uncorrelated, oppositely charged muon which fired a valid matrix element, this would appear to be a high p_T continuum dimuon event. We therefore had to check that the muons in each dimuon event satisfied the trigger condition which had caused the reading out of that event. This was done by comparing the reconstructed positions of the muons at each hodoscope plane to the aperture of the hodoscopes in the trigger which fired. If the track was outside that aperture (which was widened slightly so that we would not lose events due to chamber resolution effects), it was discarded. Events which fired PhysA2 (the like-sign trigger) were binned separately from events which fired the other PhysA triggers.

In addition to the trigger cuts outlined above, comparisons of the data and Monte Carlo suggested that there was a problem with the trigger hardware corresponding to certain matrix elements. To first order, the acceptance of the spectrometer should be left-right symmetric. A separate analysis [Bro 01], which studied events from the dump in the high mass data, noticed that several matrix elements yielded much more data relative to Monte Carlo on one side of the spectrometer than the other. This discrepancy was much larger than could be explained by left-right asymmetries in the spectrometer, and thus these matrix elements were suspect. Similar studies were performed for the target data, confirming that there was a problem with several matrix-elements. These matrix elements, which tended to be at the edge of the acceptance where the statistics

were generally poor, were eliminated from study.

4.1.4 Event Geometry

Several events which passed through all of the second pass cuts occupied regions of the spectrometer which complicated the reconstruction of their kinematics, or were judged to raise questions about their origins. Events which had a muon which appeared beam-like (tracks with $|\theta_y^{target}| < 0.006$ or tracks which were on the wrong side of the dump given their charge) were discarded. Such tracks could have originated from the decay of a hadron produced in the dump, and also followed a trajectory which skimmed the edge of the dump, calling into question the amount of energy lost by the track.

Another problematic class of events was found by studying the Monte Carlo. The energy lost by tracks in the Monte Carlo was plotted versus the x position of the tracks at SM3. Tracks near the edge of the acceptance, $|x_{SM3}| > 24''$, had significantly more energy loss in them than tracks with $|x_{SM3}| < 24''$. The source of this excess energy loss was the walls and teeth of the SM12 magnet, indicating that this class of tracks passed through a region of the magnetic field which was highly uncertain.

As discussed in the previous chapter, energy-loss fluctuations and multiple coulomb scattering cause the events to appear to reconstruct away from the actual interaction point in the target. To limit the fluctuation of energy loss and the

Table 4.2: Spill quality cuts. Events were kept if they obeyed the inequality.

	mass setting		
Cut	low	intermediate	high
SEM	> 150	> 100	> 100
IC3	> 5000	> 5000	> 5000
AMONSB / AMON	> 0.9	> 0.9	> 0.9
DUTY	> 25	> 50	> 25

effects of multiple scattering in the data, and to provide additional discrimination against events which originated outside the target volume, we required the event to reconstruct to within $2.5''$ of the nominal transverse position of the beam.

4.1.5 Spill Quality Cuts

During each beam spill, a number of quantities were monitored which told us the overall quality of the data being collected. These included the intensity of the beam (SEM and IC3), the luminosity of the target (AMON), the live-time of the spectrometer (AMONSB/AMON) and the beam duty factor (DUTY). Table 4.2 lists the spill quality cuts which were required for each spectrometer setting.

4.2 Luminosity

The intensity of the beam in each spill was measured with the SEM6 counter on the Meson East beam line. This recorded a SEM count which was proportional to the number of protons in the spill. The SEM6 counter was calibrated during special calibration runs where a thin copper foil was inserted into the beam and a SEM count accumulated during a number of spills. By studying the rate of the 1368 keV γ's emitted by the ^{24}Na produced in the interaction, the number of protons incident on the foil could be deduced, and the SEM response calibrated. These calibrations rely upon a measurement of the ^{24}Na production cross section [Bak 84] of 3.90 ± 0.11 mb[1].

Table 4.3 shows the results of several calibration measurements dating back to the original E605 experiment. Based on these measurements (taking the more recent measurements with greater weight), we estimate a SEM response of $(0.79 \pm 0.051) \times 10^8$ protons / SEM[Bro 97]. The uncertainty in the normalization was determined by adding the uncertainty due to the ^{24}Na cross section in quadrature with the standard deviation of the measurements in table 4.3.

Studies of the linearity of the SEM response were also performed by comparing the SEM counts to the luminosity as measured by the AMON and WMON detectors, and comparing to a redundant measurement of the beam intensity using the

[1] Although reference [Bak 84] measures the ^{24}Na cross section using 400-GeV protons, it is generally believed that the cross section is independent of energy.

Table 4.3: Measured SEM calibrations on the Meson East beam dating back to 1984.

Date	Protons	Protons/SEM $\times 10^8$
01/26/84	2.8E13	.83
02/11/85	6.9E12	.78
03/25/85	2.0E12	.85
05/06/85	2.0E12	.90
07/25/85	9.9E13	.80
08/29/85	9.6E13	.80
11/10/87	3.4E13	.79
11/16/87	2.4E13	.77
02/11/88	3.6E13	.78
10/29/96	1.7E12	.885
10/29/96	8.5E11	.915
12/20/96	5.1E13	.76
08/15/97	5.0E11	.86
08/29/97	2.0E11	.77

ion chambers. These studies showed the SEM response was linear with increasing beam intensity, but subject to a constant offset which varied from run to run. These offsets, shown in table 4.4, were subtracted from the SEM counts before calculating how many protons were incident on the target in each spill.

Both the density and attenuation lengths of the targets depended upon the exact composition of the targets. Therefore, assays of the cryogenic liquids were performed using samples taken when the target flasks were emptied for the Christmas shutdown (end of data set 7) and at the end of the planned run (end of data set 11). The cryogenic liquids used in the first fill had negligible amounts of contaminants. The same was true for the liquid hydrogen in the second fill. However, two separate analyses of the second fill's liquid deuterium showed a significant HD contamination. Table 4.5 shows the measured contamination and the estimated nucleon content in the target.

In order to determine the target densities, the vapor pressures of the cryogenic targets were measured and periodically recorded. The high circulation rate of the liquids, combined with the comparatively low beam current ensured that the cryogenic liquids did not boil during the spill which would have reduced the densities of the targets. Table 4.6 shows the mean target pressure for selected data sets in the experiment.

Cryogenic data tables [Rod 73] were used to calculate the target densities from the average vapor pressures. Taking the pressure P to be measured in psi, and

Table 4.4: Offsets to the SEM counters which were subtracted from each spill. I_{run} is the run number.

Starting run	Ending run	SEM offset
1551	1588	27
1589	1620	$1.479 \times I_{\text{run}} - 2436$
1631	1690	28
1879	1884	28
1886	1887	155
1888	——	275
1889	1944	375
1945	2020	130
2021	2046	0
2049	2053	98
2056	2078	100
2079	2115	30

Table 4.5: Percent molecular and atomic abundance of second deuterium fill.

Molecule	percent abundance (first analysis)	percent abundance (second analysis)
D_2	94.13 ± 0.58	92.7 ± 0.8
HD	5.82 ± 0.58	6.89 ± 0.69
H_2	0.05 ± 0.01	0.147 ± 0.015
other	–	–
Atom	estimated abundance	
D	97.00 ± 0.6	
H	3.00 ± 0.6	

Table 4.6: Target pressures (in psi) for selected data sets.

Data set	hydrogen	deuterium
5	14.97	14.92
7	15.04	14.96
8	15.11	15.17
11	15.15	15.21

density ρ in g/cm^3, the expression for the density of hydrogen is given by

$$\frac{1}{\rho_h} = 62.473\,\{0.2115 + 1.171 \times 10^{-3}P - 1.109 \times 10^{-5}P^2\}, \tag{4.9}$$

and that for deuterium by

$$\rho_d = 4.028 \times 10^{-3}\{43.291 - 3.4176\frac{P}{14.6959} + 0.5783(\frac{P}{14.6959})^2\} \tag{4.10}$$

These result in densities which vary from data set to data set by no more than $\sim 2\%$, which is negligible compared to the 6.5% uncertainty in the beam normalization. From the measured pressures, the densities of the hydrogen and deuterium targets were determined to be

$$\rho_h = 0.0706\,\mathrm{g/cm^3}$$

$$\rho_d = 0.1630\,\mathrm{g/cm^3}.$$

As reported in the particle data book [Gro 00], the hadronic interaction lengths for hydrogen and deuterium are 50.8 g/cm^2 and 54.7 g/cm^2 respectively. To ex-

press these lengths in terms of the physical length, as opposed to the "thickness" of the target, we need to divide by the density of the targets. For the cryogenics used in the first fill, and the liquid hydrogen from the second fill, this is all we needed to do. For the liquid deuterium from the second fill, however, we needed to correct for the hydrogen contamination by taking the weighted average. The resulting hadronic absorption lengths are

$$\begin{aligned} \lambda_{lh2} &= 719.5\,\mathrm{cm} \\ \lambda_{ld2}^{(1\mathrm{st})} &= 335.6\,\mathrm{cm} \\ \lambda_{ld2}^{(2\mathrm{nd})} &= 340.6\,\mathrm{cm} \end{aligned}$$

where the superscripts indicate either the first or second fill. The total integrated luminosities for each data set and the entire data sample are shown in table 4.7.

4.3 Trigger Efficiencies

In order to properly measure the efficiencies of the hodoscopes, it was necessary to use a sample of events which were triggered independently of the hodoscopes being measured. Because we only use the information from the Y hodoscopes in the experiment, events which triggered on the X hodoscopes could provide this independent measurement. Unfortunately, the rate of events which satisfied the X134L·X134R trigger (a muon on either side of the spectrometer) was prohibitively high to take along with the physics data. Therefore, several specialized runs were taken periodically to determine the efficiencies of the Y hodoscopes. A specialized

Table 4.7: Integrated luminosities in the E866 data sets.

Data Set	Integrated H_2 Luminosity (nucleon/nb)	Integrated D_2 Luminosity (nucleon/nb)
5	4.74×10^6	1.04×10^7
7	1.97×10^7	4.34×10^7
8	4.04×10^7	8.95×10^7
9	2.95×10^6	6.65×10^6
10	4.72×10^5	1.03×10^6
11	1.03×10^7	2.28×10^7
Total	7.86×10^7	1.74×10^8

trigger required that five hodoscope planes on one side of the spectrometer were hit. Reconstructed single muon tracks which fired at least six hodoscopes (one in each plane) were then studied to determine the efficiency of the hodoscope in the seventh plane. The typical efficiencies measured were $\sim 97\%$. However, these specialized runs did not measure the efficiencies near the edge of the acceptance with sufficient precision. To increase the statistics in these regions, we used events from the full data set. Although these events introduced a bias from the trigger to the efficiency measurement, they did probe the edge of the acceptance with far more statistics. The efficiencies measured here were checked against those of the specialized runs and found to be largely consistent.

4.4 Chamber Efficiencies

In order to study the efficiency of each detector plane, we began with a sample of tracks which would have been reconstructed regardless of whether or not the particular detector plane being studied had fired or not. This was possible due to the redundant tracking information at each station. Each plane was divided into quadrants, and the ratio of the number of tracks which fired in a given quadrant to the total number of tracks passing through the quadrant was used to estimate the efficiency of the drift chamber.

The use of single-hit TDC's in the DAQ electronics introduced an additional source of inefficiency. A second charged particle which passed through a drift cell

Table 4.8: Rate-dependence correction factors for the E866 data. Each event is weighted by $1 - SEM \times R_i$, where i is the target.

Mass Setting	R_d	F	$R_h = R_d/F$
Low	-0.2035×10^{-4}	1.51	$-.1348 \times 10^{-4}$
Intermediate	-0.4976×10^{-5}	1.18	$-.4152 \times 10^{-5}$
High	-0.2696×10^{-5}	1.78	$-.1515 \times 10^{-5}$

following the first particle in an event would not have its position recorded to tape, resulting in the event being more difficult to reconstruct. This effect would have a definite dependence on the event rate, and therefore the beam intensity.

To correct for the rate dependence, the number of reconstructed events per unit beam intensity (measured in terms of SEM counts) was plotted versus the beam intensity and fit to a straight line. The fits for hydrogen and deuterium were constrained by the relative number of extra drift chamber hits in an average event $F = \frac{N_d^{\text{extra}}}{N_h^{\text{extra}}}$ for each target [Tow 99]. This meant that only one parameter, the slope R_d of the efficiency-versus-intensity plot for deuterium, needed to be determined for each mass setting. Figure 4.5 shows the fit for the high mass data, and table 4.8 shows the corrections obtained by reference [Tow 99].

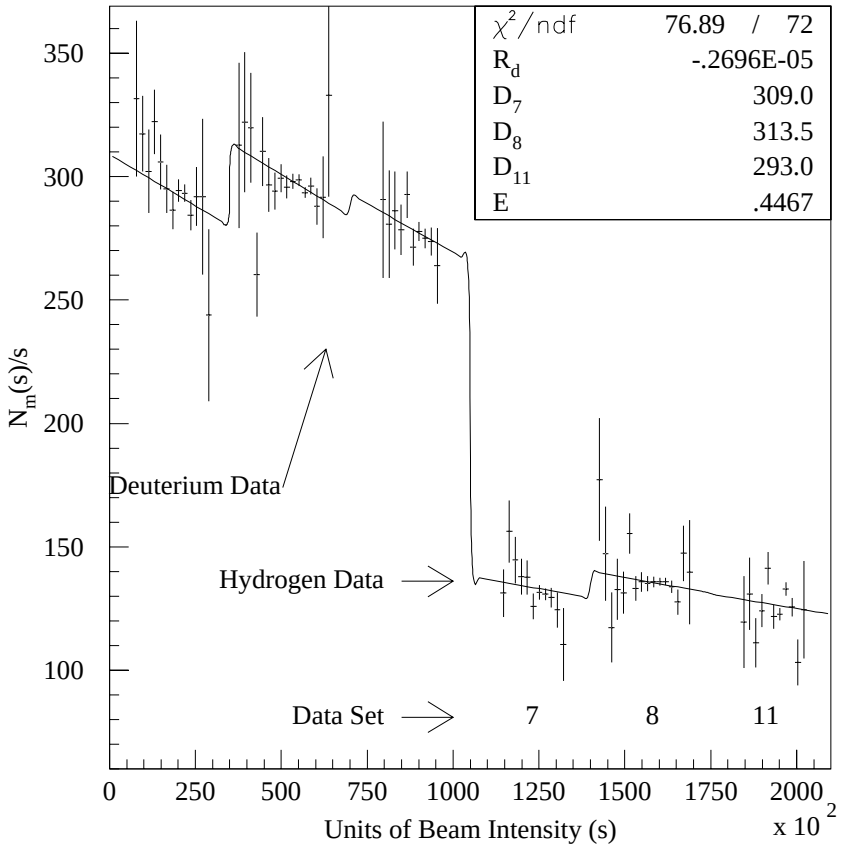

Figure 4.5: Dimuon yield (N_m) per unit beam intensity (s) versus beam intensity for the high mass data, as given in reference [Tow 99].

4.5 Monte Carlo and Acceptance

The acceptance of the spectrometer was a complicated function involving the detector geometry, the magnitudes of the magnetic fields in each of the three spectrometer magnets, the efficiencies of the detectors and trigger, and the various physical processes which muons traversing the spectrometer were subject to. This level of complexity required the use of a Monte Carlo simulation to determine the acceptance of the spectrometer.

The E866 Monte Carlo consisted of custom routines designed to simulate the production of dimuon events, the passage of the resulting muons through the spectrometer, and the detector response to their passage. The output of the Monte Carlo was a file whose format was identical to that produced by the DAQ during the experiment. This enabled us to analyze the Monte Carlo events with the exact same analysis chain as the real data, minimizing any systematic differences between the data and Monte Carlo.

To further minimize these differences, the Monte Carlo was configured to simulate as closely as possible the state of the spectrometer while it was taking data, the physical processes the muons were subject to in passing through the spectrometer, and the physical processes giving rise to the dimuon events. In chapter 3 we discussed how we obtain information about the state of the spectrometer (magnetic fields, detector alignments and efficiencies, etc...). We will discuss how

events were generated in the Monte Carlo, the simulation of the physical processes the resulting muons were subject to, and the final set of calculations needed to compute the acceptance of the spectrometer.

4.5.1 Event Generation

In order to generate a continuum dimuon event, we had to sample the six kinematic variables $M_{\mu^+\mu^-}$, x_F, p_T, ϕ_p, ϕ_d, and θ_d from distributions which closely approximate the actual differential cross section $d^6\sigma/dMdx_F dp_T d\theta_d d\phi_p d\phi_d$. *A priori* we know the cross section differential in the angular variables goes like,

$$\frac{d^3\sigma}{d\theta_d d\phi_d d\phi_p} \propto 1 + \cos^2(\theta_d) \tag{4.11}$$

since there is no preferred direction in the experiment to give a ϕ dependence, and the virtual photon in a $q\bar{q}$ annihilation is produced transversely polarized as predicted by QED and confirmed by experiment [Con 89, McG 99, Cha 99, Bro 01].

Next-to-leading order calculations of the doubly-differential cross section $d^2\sigma/dMdx_F$ agree well with existing measurements of the deuterium and nuclear cross sections, but problems arise in QCD in calculating the full triple differential cross section $d^3\sigma/dMdx_F dp_T$. Therefore, an empirical form [Kap 78] for the p_T dependence of the cross section was used

$$\frac{d^3\sigma_{\text{empirical}}}{dMdx_F dp_T} \propto \frac{1}{p_T^0} \frac{10 p_T/p_T^0}{(1+(p_T/p_T^0)^2)^6} \times \frac{d^2\sigma_{\text{NLO}}}{dMdx_F} \tag{4.12}$$

where $p_T^0 = 2.8$ GeV was fit to both the hydrogen and deuterium data, and the MRST 98 [MRST 98] partons were used in the NLO calculations of $d^2\sigma/dMdx_F$.

4.5.2 Physics Simulation and Detector Response

Once an event had been sampled from the above distributions, the kinematics of each muon were calculated and boosted into the lab frame, and the event vertex sampled from

$$P(z) = \frac{1}{\lambda}\frac{e^{-z/\lambda}}{1 - e^{-L/\lambda}}. \tag{4.13}$$

Inside the target, the very small amount of multiple scattering the muons were subject to was simulated. This multiple scattering was found to be negligible.

After the effects on the muons in the target had been simulated, the muon's positions were extrapolated to the point at which the SM0/SM12 field began. The same magnetic field maps which were used in the analysis as well as the overall field strengths as computed from the data were used here. The muons were propagated through the magnetic field one at a time in 5 cm steps. At each step in the field, the magnetic field kick was calculated, using

$$dp_x = -q\ dz\, B_y \tag{4.14}$$

$$dp_y = q\ dz\, B_x \tag{4.15}$$

which neglected only the small z component of the force[2].

[2]To be precise, we computed the changes in the x and y components of the muon's momentum,

In addition to the simulation of the magnetic fields, the effects of the beam dump and absorbing wall had to be included. Multiple scattering was simulated in each 5 cm step of the dump and absorbing wall, using the *gmols* routine from the standard GEANT [GEANT] simulation package. This was the only case where a GEANT routine was used in the Monte Carlo. Multiple scattering was also simulated in the materials found in the helium bags which filled SM0 and SM12 downstream of the absorber, the air and helium the muons had to pass through, the hodoscope and drift chamber planes, and the bulk material at station 4.

The energy lost by muons traversing the spectrometer was sampled from a set of fast lookup tables generated using Von Ginniken's TRAMU program [Gin 86]. Twelve tables for muons with incident momenta between 10 and 600 GeV were interpolated to obtain the energy loss for muons of arbitraty momenta. This number was then scaled from the length of material assumed in the table to the step size of 5 cm, and subtracted from the muon's momenta in each step. A new energy loss was sampled once the muon had traversed the length of material specified by the energy loss routines. This greatly simplified the energy-loss simulation in the dump, where the total length of material the muon would pass through was not known beforehand. The only other places where energy loss was simulated was in the teeth and walls of the SM12 magnet, and the hadronic and EM calorimeters

then applied momentum conservation to calculate the final z component of the momentum. It can be shown that this causes a systematic error in the momentum at each step which is negligible over the entire magnetic field.

at station 4. A precise simulation of the energy loss was unnecessary here, so a constant energy loss was subtracted in these materials.

Equation 4.6 indicates separate corrections for the acceptance of the spectrometer and detector efficiencies. In reality, though, the Monte Carlo simulated detector inefficiencies based on the measurements described above. Thus, the acceptance calculations contained the efficiency corrections. Only the rate-dependent inefficiencies were corrected for separately.

4.5.3 Acceptance Calculation

Once a sufficient number of Monte Carlo events had been recorded, they were subjected to the same analysis chain and cuts described in chapters 3 and 4. The only difference was that spill quality cuts were not applied to the Monte Carlo. Once we had filtered the Monte Carlo event sample, the acceptance in any given bin could be calculated as the ratio of the number of surviving Monte Carlo events in that bin divided by the total number of events generated in that bin

$$\alpha(M, x_F, p_T) = \frac{N_{\rm MC}^{\rm acc}(M, x_F, p_T)}{N_{\rm MC}^{\rm gen}(M, x_F, p_T)}. \tag{4.16}$$

Calculating the number of accepted and generated Monte Carlo events in each bin would have been a straightforward counting exercise, save for two reasons. First, comparisons of the data to the Monte Carlo revealed differences on the order of 10 to 15% which we wished to eliminate[3]. Second, in order to eliminate the

[3]These differences were consistent with the observed differences between the measured cross

systematic error between the hydrogen and deuterium cross sections introduced by finite Monte Carlo statistics in the acceptance calculation, the same sample of Monte Carlo events were used to calculate the acceptance for hydrogen and deuterium. Since the event sample had been generated using either a hydrogen or deuterium target, the events had to be reweighted by the cross section appropriate to the target being calculated.

Differences between the data and Monte Carlo were reduced by reweighting the Monte Carlo events as a function of M, x_F and p_T. These functions were determined by polynomial fits to the ratios of the data divided by the Monte Carlo. Furthermore, the p_T cross section was seen to vary as a function of M and x_F. This correlation was dealt with by fitting p_T^0 in each bin, resulting in the empirical form

$$p_T^0(M, x_F) = 1.21 + 0.350M - 0.0182M^2 + 1.37x_F + 2.60x_F^2 \tag{4.17}$$

which was the same for both targets, within the uncertainties in the fit parameters. The resulting weighting functions for the Monte Carlo were consistent with the differences observed between the measured cross sections and the double-differential cross section tables used to generate the Monte Carlo.

Monte Carlo events which had been generated using hydrogen as the target were reweighted with the deuterium cross section and vertex distribution when

sections, and the NLO calculations upon which the Monte Carlo generator was based.

calculating the deuterium cross section. Thus, the deuterium yield calculated from a hydrogen Monte Carlo event sample was given by

$$N_{\mathrm{D2MC}} = \sum_{i=1}^{N_{\mathrm{H2MC}}} \frac{d^3\sigma_{pd}(M^i, x_F^i, p_T^i)}{d^3\sigma_{pp}(M^i, x_F^i, p_T^i)} \times \left(\frac{e^{-z/\lambda_{\mathrm{D2}}}}{e^{-z/\lambda_{\mathrm{H2}}}} \right) \tag{4.18}$$

Hydrogen yields were calculated from deuterium Monte Carlo samples in a similar manner:

$$N_{\mathrm{H2MC}} = \sum_{i=1}^{N_{\mathrm{D2MC}}} \frac{d^3\sigma_{pp}(M^i, x_F^i, p_T^i)}{d^3\sigma_{pd}(M^i, x_F^i, p_T^i)} \times \left(\frac{e^{-z/\lambda_{\mathrm{H2}}}}{e^{-z/\lambda_{\mathrm{D2}}}} \right). \tag{4.19}$$

This procedure was carried out for both the accepted and generated events, maintaining the relative normalization of the thrown and accepted Monte Carlo, and equation 4.16 was used to compute the acceptance.

Figures 4.6 and 4.7 compare the data and Monte Carlo for several reconstructed pair- and detector-quantities, summed over both targets and averaged over all data sets. The agreement between the data and Monte Carlo is quite good for most physics and detector distributions. The discrepancies in the single track momentum distributions, which occur at larger momenta where the statistics are poor, are thought to be due to beam-alignment problems. The other major discrepancy is in the ZUNIN distributions. This is partly due to a slightly wider ZUNIN distribution in the Monte Carlo than is observed in the data, but mainly due to the centroids of the data and Monte Carlo distributions not being precisely aligned[4].

[4]This is a major component of the estimated systematic errors discussed below.

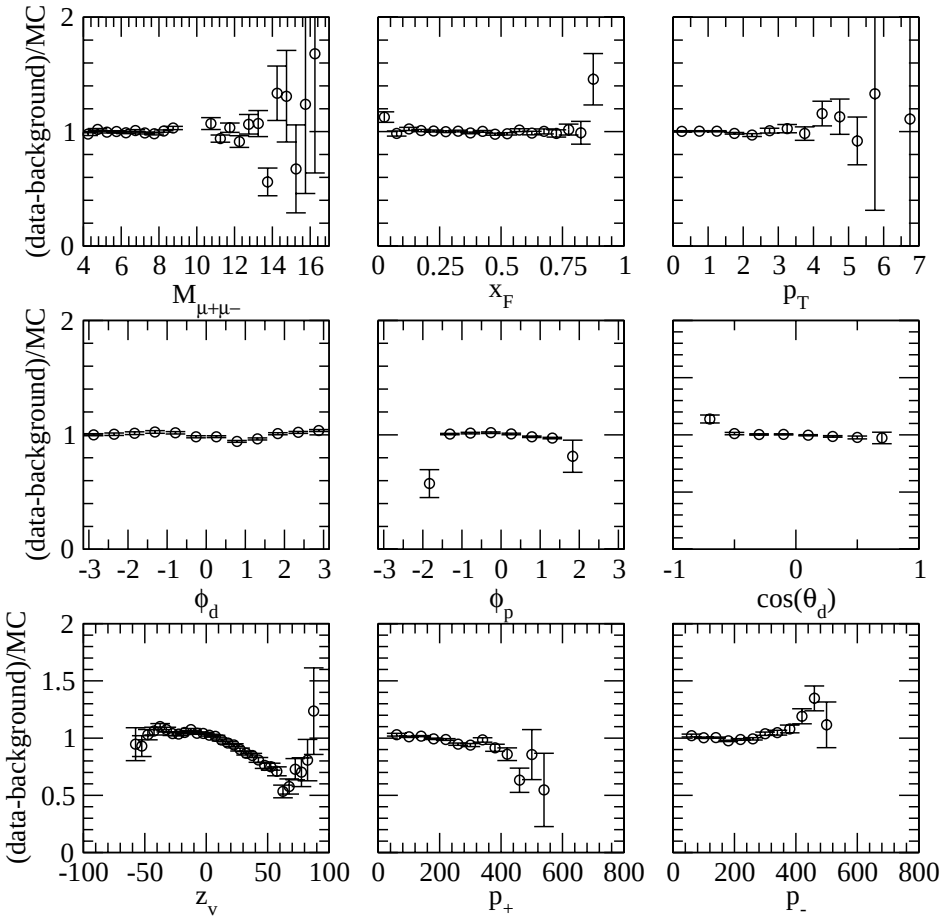

Figure 4.6: Ratios of data and Monte Carlo yields for several "pair" quantities (mass, x_F, p_T, ϕ_d, ϕ_p, $cos(\theta_d)$ and ZUNIN) and the positive and negative track momenta. Data averaged over all targets and data sets.

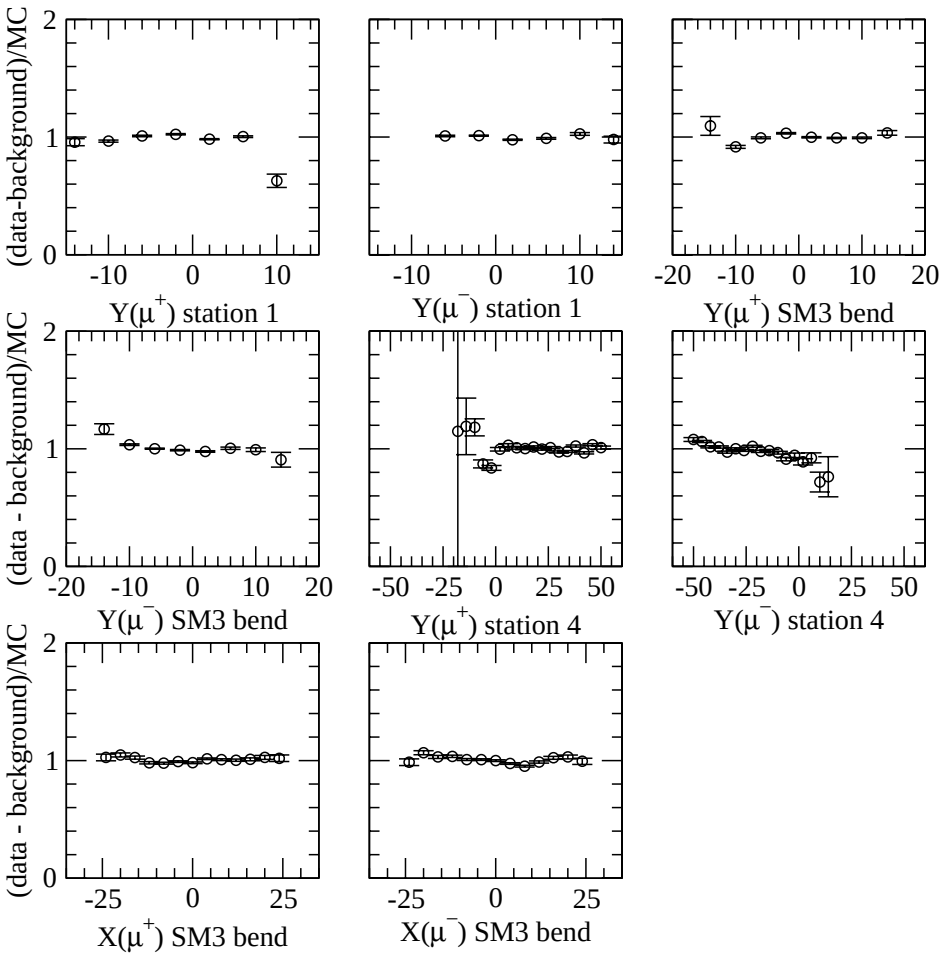

Figure 4.7: Ratios of data and Monte Carlo yields for the distributions of positive and negative tracks projected onto the station 1 hodoscope-, SM3 bend- and station 4 hodoscope-planes. Data averaged over all targets and data sets.

4.6 Combining the Data

Once all of the data were binned and subjected to all of the corrections described above, we had a measurement of the triple-differential cross sections $d^3\sigma(pp)/dMdx_Fdp_T$ and $d^3\sigma(pd)/dMdx_Fdp_T$ for each of the six data sets used in the analysis. For the purposes of the following discussion, we denote the measured cross section in a given M, x_F, p_T bin as $\sigma_i \pm \delta\sigma_i \pm \Delta\sigma_i$, where i represents the data set, $\delta\sigma_i$ is the statistical uncertainty and $\Delta\sigma_i$ is the systematic uncertainty.

The results from the six data sets were first combined into three results corresponding to each mass setting. We used the weighted average

$$\sigma \pm \delta\sigma = \frac{\sum_i \sigma_i \omega_i}{\sum_i \omega_i} \pm \sqrt{\frac{1}{\sum_i \omega_i}} \tag{4.20}$$

where the weights were given by $\omega_i = \frac{1}{(\delta\sigma_i)^2}$. After the average cross section for each mass setting was calculated, the three mass settings were combined into a single result, again using equation 4.20. This procedure neglected the systematic uncertainties between data sets and mass settings, which were sufficiently small so that the average was not affected much by the omission. Also, it would not have been appropriate to use the systematic uncertainties in computing the averages, as most of the systematic uncertainty in the cross sections were (by design) common to the hydrogen and deuterium measurements.

4.6.1 Systematic Uncertainties

Computing the systematic uncertainty in the combined cross section was a fairly straightforward exercise in error propagation. The standard error propagation formula for an expression $f(x_1, x_2, ..., x_N)$ is given by

$$(\Delta f)^2 = \sum_{i=1}^{N} \left(\frac{\delta f}{\delta x_i} \right)^2 (\Delta x_i)^2 . \tag{4.21}$$

From this formula, it can be shown that the systematic uncertainty in equation 4.20 is given by

$$(\Delta \sigma)^2 = \frac{\sum_i \omega_i^2 (\Delta \sigma_i)^2}{\left(\sum_i \omega_i\right)^2} \tag{4.22}$$

where the ω_i are the statistical weights used in the weighted average. One need only compute the systematic uncertainty in each data set (mass setting) $\Delta\sigma_i$.

Recalling equation 4.6, the systematic uncertainty on a given cross section measurement will, by equation 4.21, be given by

$$\left(\frac{\Delta \sigma_i}{\sigma_i} \right)^2 = \left(\frac{\Delta \alpha_i}{\alpha_i} \right)^2 + \left(\frac{\Delta \epsilon_i}{\epsilon_i} \right)^2 + \left(\frac{\Delta \mathcal{L}_i}{\mathcal{L}_i} \right)^2 + \left(\frac{\Delta N_{\mu^+\mu^-}}{N_{\mu^+\mu^-}} \right)^2 \tag{4.23}$$

We must be careful here, however. The uncertainty in the luminosity $\Delta\mathcal{L}$, for instance, is dominated by a $\pm 6.5\%$ uncertainty in the beam normalization. This uncertainty is common to all data sets and mass settings. It would not be appropriate to treat it as an independent 6.5% uncertainty in each measurement. We also assume that the uncertainties in detector efficiencies $\Delta\epsilon$ are common to each

data set in a given mass setting, since events with similar kinematics will occupy similar regions of the spectrometer. We discuss how the systematic uncertainties were treated below.

4.6.2 Uncorrelated Systematic Uncertainties

The systematic uncertainties, not including the ±6.5% normalization uncertainty, fell into three categories: uncorrelated uncertainties, uncorrelated uncertainties which are common to a given mass setting, and correlated uncertainties which are common to a given mass setting. In general, we treated these systematic uncertainties separately. In the end they were combined in quadrature to estimate the total systematic uncertainty on the averaged cross sections.

The only uncorrelated systematic uncertainty which was not shared between the data sets in a given mass setting was the uncertainty in the acceptance due to the statistical uncertainty in the Monte Carlo. The uncertainty in each mass setting due to this statistical uncertainty was therefore estimated to be, according to the prescription of equation 4.22

$$\left(\Delta\sigma_{\alpha,stat}\right)^2 = \frac{\sum_i \omega_i^2 \left(\Delta\sigma_i^{\alpha,\mathrm{stat}}\right)^2}{\left(\sum_i \omega_i\right)^2} \tag{4.24}$$

where $\Delta\sigma_i^{\alpha,\mathrm{stat}} = \frac{\Delta\alpha_i^{\mathrm{stat}}}{\alpha_i}\sigma_i$ is the uncertainty in the i^{th} measurement due to the statistical uncertainty in the acceptance $\Delta\alpha_i$.

The next step combined all of the uncorrelated uncertainties which were com-

mon to a given mass setting. These included the uncertainties in the acceptance in each mass setting, calculated above, and the uncertainties in the detector efficiencies. Again we use equation 4.22

$$\left(\Delta\sigma_{\text{uncorrelated}}\right)^2 = \frac{\sum_i \omega_i^2 \left\{\left(\Delta\sigma_\alpha\right)^2 + \left(\Delta\epsilon_{\text{hodo}}\right)^2 + \left(\Delta\epsilon_{\text{chamber}}\right)^2 + \left(\Delta\epsilon_{\text{trig}}\right)^2\right\}}{\left(\sum_i \omega_i\right)^2} \quad (4.25)$$

where the sum is now over all mass settings instead of all data sets in a given mass setting.

The remaining source of systematic uncertainty was the uncertainty in the acceptance due to uncertainties in the magnetic-field tweeks as measured in chapter 3. Unlike the previous sources of uncertainties we have discussed, we expect this uncertainty to be at least partially correlated from mass setting to mass setting – the SM3 tweek was wholly determined by measurements from the high mass data.

An estimation of the size of this uncertainty in any given mass setting was performed using a Monte Carlo based on the code described above, modified to propagate a given event through the spectrometer multiple times with different settings of the magnetic fields. In this modified Monte Carlo, all random processes, such as energy loss, multiple scattering and detector resolutions and efficiencies, were turned off. The result was a highly correlated sample of Monte Carlo events where any differences in reconstructed yields were due solely to acceptance effects.

4.6.3 Correlated Systematic Uncertainties

The systematic uncertainty in the acceptance due to the uncertainties in the magnetic field in any given mass setting could then be estimated by

$$\left(\frac{\Delta\alpha_{\text{tweek}}}{\alpha}\right) \approx 2\,|\frac{N_{\text{nominal}+\delta} - N_{\text{nominal}}}{N_{\text{nominal}+\delta} + N_{\text{nominal}}}|. \tag{4.26}$$

Here, N_{nominal} represented the number of Monte Carlo events subjected to the nominal magnetic field tweeks in traversing the spectrometer which survived the standard analysis chain. Similarly, $N_{\text{nominal}+\delta}$ were the number of Monte Carlo events subjected to a set of augmented magnetic fields in traversing the spectrometer, which were again subjected to the standard analysis chain. The field tweeks in this case were all augmented by the estimates of their uncertainties[5], which should result in the maximum possible uncertainty.

This results in a systematic uncertainty in the cross section for each mass setting given by

$$\Delta\sigma_i^{\alpha,\text{tweek}} = \left(\frac{\Delta\alpha_{\text{tweek}}}{\alpha}\right)\sigma_i. \tag{4.27}$$

To estimate the uncertainty in the total cross section, we depart from the prescription given by equation 4.22. We do this, because equation 4.22 is based on the assumption that the systematic uncertainties obey Gaussian statistics. This

[5] In the case of the low mass data, the SM12 and SM3 field tweeks were augmented by their systematic uncertainties while the SM0 field tweek was reduced by its uncertainty. This resulted in the maximum possible systematic uncertainty in the acceptance for that spectrometer configuration.

is a good assumption for many of the sources of uncorrelated systematic uncertainties. Here it is not. Therefore we treat the systematic uncertainty $\Delta\sigma_i^{\alpha,\text{tweek}}$ as a potentially "missing" or "excess" cross section for each mass setting, for which we wish to obtain an average estimate for the total cross section. We take

$$\Delta\sigma_{\text{correlated}} = \frac{\sum_i \omega_i \Delta\sigma_i^{\alpha,\text{tweek}}}{\sum_i \omega_i} \tag{4.28}$$

where once again the ω_i are the statistical weights of the given mass setting. Finally, we add the correlated and uncorrelated systematic uncertainties in quadrature to obtain an estimate for the total systematic uncertainty

$$\Delta\sigma = \sqrt{\left(\Delta\sigma_{\text{uncorrelated}}\right)^2 + \left(\Delta\sigma_{\text{correlated}}\right)^2}. \tag{4.29}$$

4.6.4 Integrating the Data

After the data were combined using equation 4.20, we integrated the triple-differential cross sections over p_T to obtain the double-differential cross sections $d^2\sigma(pp)/dMdx_F$ and $d^2\sigma(pd)/dMdx_F$. The integrated cross sections were given by

$$M^3\frac{d^2\sigma}{dMdx_F} = M^3\sum_i^N \left(\frac{d^3\sigma}{dMdx_F dp_T}\right)_i \Delta p_{T,i} + f(M, x_F; \alpha) \tag{4.30}$$

where the sum is over all N p_T bins whose widths are denoted $\Delta p_{T,i}$ and $f(M, xF; \alpha)$ represents a correction explained below. The statistical and systematic uncertainties[6] on the integrated cross sections were calculated using the usual error prop-

[6]Correlated and uncorrelated systematic uncertainties were first treated separately, then combined in quadrature to obtain the total systematic uncertainty.

agation in equation 4.23 – in other words, the uncertainties (multiplied by Δp_T) were added in quadrature.

The correction in the integral $f(M, x_F; \alpha)$ accounted for the fact that the acceptance of the spectrometer could not reach the full kinematic limit in p_T. For each bin in mass and x_F, the triple-differential cross sections were integrated only over the range in p_T where the acceptance was nonzero. Where the acceptance was nonzero, and all data sets lacked events, we made an estimate of the missing cross section $f(M, x_F; \alpha)$. The estimate was based on the empirical p_T distribution given in equation 4.12 and the parameterization of p_T^0 given in equation 4.17, extrapolated from the largest nonzero p_T bin to infinity.

The resulting corrections were well below 1% over much of the kinematic range covered. Only at larger masses did the correction to the cross sections approach 5%. While the empirical form for the p_T dependence of the cross section does a fairly good job of reproducing the data, it tends to underestimate the tail of the distribution. Given this, and the uncertainties in the parameterization of p_T^0, we estimate that the correction $f(M, x_F; \alpha)$ is uncertain by about $\pm 15\%$. This uncertainty was added in quadrature to the systematic uncertainties in the final result.

5 RESULTS

Fermilab Experiment 866 has measured continuum dimuon production cross sections in 800-GeV pp and pd interactions. These data, which are presented below, represent the most extenive study of the differential pp cross to date, while the pd data offer better precision over a broader range of x_F than previous measurements have achieved. In this chapter we tabulate and plot the double- and triple-differential cross sections, while deferring a discussion of the results until the next chapter.

5.1 FNAL E866/NuSea Results – $M^3 d^2\sigma/dMdx_F$

The scaling form $M^3 d^2\sigma/dMdx_F$ for the hydrogen and deuterium cross sections are tabulated below in tables 5.1 and 5.2. The data are tabulated in mass and $x_F \equiv \frac{2p_L}{\sqrt{s}}$ bins. The mass and x_F ranges are shown in the tables, as are the mean mass, x_F and p_T in each bin. The data in the tables are plotted in figures 5.1 through 5.16, and compared to NLO calculations of the cross sections using different sets of parton distributions.

Table 5.1: Scaling form $M^3 d^2\sigma/dMdx_F$ (in units of nb GeV^2 / nucleon) for the hydrogen cross section. Statistical and point-to-point systematic uncertainties are shown separately. The normalization is subject to an uncertainty of $\pm 6.5\%$.

Mass [GeV]	$< M >$	$< x_F >$	$< p_T >$	$-0.05 \leq x_F < 0.05$	Stat. Error	Syst. Error
4.20 - 4.70	4.64	0.046	0.65	7.92e+01	5.60e+01	1.06e+01
4.70 - 5.20	5.01	0.044	0.36	1.23e+01	6.75e+00	1.11e+00
5.20 - 5.70	5.45	0.039	0.48	3.01e+01	1.81e+01	3.84e+00
5.70 - 6.20	6.07	0.036	1.10	4.02e+01	1.47e+01	3.06e+00
6.20 - 6.70	6.46	0.029	0.93	1.08e+01	3.52e+00	5.38e-01
6.70 - 7.20	6.89	0.019	0.68	7.46e+00	2.07e+00	2.78e-01
7.20 - 7.70	7.54	0.024	0.84	6.17e+00	2.56e+00	4.24e-01
7.70 - 8.20	8.04	0.028	0.94	5.50e+00	9.03e-01	1.91e-01
8.20 - 8.70	8.46	0.016	0.85	3.70e+00	4.69e-01	1.07e-01
10.85 - 11.85	10.86	0.047	1.43	8.02e+00	8.02e+00	8.85e-01
Mass [GeV]	$< M >$	$< x_F >$	$< p_T >$	$0.05 \leq x_F < 0.10$	Stat. Error	Syst. Error
4.20 - 4.70	4.46	0.083	0.77	2.67e+01	2.76e+00	7.73e-01
4.70 - 5.20	4.90	0.080	0.76	1.54e+01	2.28e+00	7.09e-01
5.20 - 5.70	5.43	0.083	0.86	1.06e+01	2.83e+00	1.03e+00
5.70 - 6.20	5.95	0.083	0.94	1.24e+01	2.59e+00	7.74e-01
6.20 - 6.70	6.48	0.078	0.98	6.37e+00	1.82e+00	4.82e-01
6.70 - 7.20	6.93	0.076	0.86	6.13e+00	2.08e+00	2.29e-01
7.20 - 7.70	7.50	0.080	0.98	6.60e+00	1.95e+00	4.68e-01
7.70 - 8.20	7.95	0.078	1.04	4.17e+00	5.43e-01	2.23e-01
8.20 - 8.70	8.44	0.077	1.03	3.71e+00	4.83e-01	1.75e-01
10.85 - 11.85	11.17	0.081	1.15	3.46e+00	1.51e+00	7.66e-02

Table 5.1: continued

Mass [GeV]	$< M >$	$< x_F >$	$< p_T >$	$0.10 \leq x_F < 0.15$	Stat. Error	Syst. Error
4.20 - 4.70	4.43	0.129	0.91	2.34e+01	1.38e+00	5.31e-01
4.70 - 5.20	4.92	0.127	0.90	1.59e+01	1.26e+00	4.18e-01
5.20 - 5.70	5.41	0.130	0.92	1.54e+01	1.58e+00	5.82e-01
5.70 - 6.20	5.95	0.128	0.91	1.26e+01	1.45e+00	3.60e-01
6.20 - 6.70	6.44	0.130	1.04	9.98e+00	1.22e+00	2.94e-01
6.70 - 7.20	6.97	0.130	0.99	6.86e+00	1.05e+00	3.05e-01
7.20 - 7.70	7.46	0.128	1.10	5.06e+00	4.80e-01	1.84e-01
7.70 - 8.20	7.95	0.127	1.10	4.56e+00	3.67e-01	1.47e-01
8.20 - 8.70	8.44	0.127	1.12	3.11e+00	2.61e-01	9.49e-02
10.85 - 11.85	11.22	0.129	1.10	1.36e+00	3.42e-01	5.81e-02
Mass [GeV]	$< M >$	$< x_F >$	$< p_T >$	$0.15 \leq x_F < 0.20$	Stat. Error	Syst. Error
4.20 - 4.70	4.43	0.177	1.00	1.92e+01	9.66e-01	1.21e+00
4.70 - 5.20	4.94	0.177	0.96	1.45e+01	7.20e-01	2.55e-01
5.20 - 5.70	5.43	0.177	1.02	1.20e+01	9.89e-01	2.71e-01
5.70 - 6.20	5.91	0.178	1.02	8.96e+00	7.88e-01	1.99e-01
6.20 - 6.70	6.45	0.179	1.02	8.04e+00	8.68e-01	3.04e-01
6.70 - 7.20	6.96	0.179	1.06	6.22e+00	4.59e-01	1.98e-01
7.20 - 7.70	7.46	0.177	1.12	4.82e+00	2.98e-01	1.18e-01
7.70 - 8.20	7.94	0.176	1.12	3.61e+00	2.45e-01	9.41e-02
8.20 - 8.70	8.44	0.176	1.19	3.00e+00	1.98e-01	6.28e-02
10.85 - 11.85	11.18	0.178	1.09	1.08e+00	2.41e-01	7.37e-02
11.85 - 12.85	12.23	0.177	1.37	1.25e+00	5.62e-01	1.54e-01
12.85 - 14.85	13.31	0.185	1.24	1.17e+01	1.03e+01	3.13e-01

Table 5.1: continued

Mass [GeV]	$< M >$	$< x_F >$	$< p_T >$	$0.20 \leq x_F < 0.25$	Stat. Error	Syst. Error
4.20 - 4.70	4.43	0.226	1.02	1.68e+01	6.71e-01	2.97e-01
4.70 - 5.20	4.93	0.225	1.02	1.26e+01	6.54e-01	2.35e-01
5.20 - 5.70	5.43	0.225	1.00	9.38e+00	5.79e-01	1.77e-01
5.70 - 6.20	5.95	0.228	1.05	8.45e+00	5.19e-01	2.48e-01
6.20 - 6.70	6.46	0.228	0.99	7.22e+00	3.73e-01	1.88e-01
6.70 - 7.20	6.95	0.227	1.09	5.18e+00	2.72e-01	1.09e-01
7.20 - 7.70	7.45	0.227	1.12	3.91e+00	2.28e-01	1.13e-01
7.70 - 8.20	7.94	0.225	1.16	3.73e+00	1.97e-01	8.98e-02
8.20 - 8.70	8.44	0.224	1.19	2.76e+00	1.89e-01	6.10e-02
10.85 - 11.85	11.22	0.231	1.45	7.48e-01	1.34e-01	4.23e-02
11.85 - 12.85	12.33	0.226	1.33	2.02e+00	7.89e-01	6.25e-01
12.85 - 14.85	13.22	0.226	1.04	2.36e+00	1.82e+00	3.90e-01
Mass [GeV]	$< M >$	$< x_F >$	$< p_T >$	$0.25 \leq x_F < 0.30$	Stat. Error	Syst. Error
4.20 - 4.70	4.44	0.274	1.04	1.23e+01	5.17e-01	2.79e-01
4.70 - 5.20	4.95	0.276	1.04	1.01e+01	4.91e-01	1.74e-01
5.20 - 5.70	5.44	0.276	1.04	7.25e+00	4.24e-01	2.03e-01
5.70 - 6.20	5.94	0.277	1.01	7.53e+00	3.04e-01	1.93e-01
6.20 - 6.70	6.45	0.276	1.04	5.64e+00	2.62e-01	1.49e-01
6.70 - 7.20	6.94	0.276	1.09	4.46e+00	2.09e-01	8.33e-02
7.20 - 7.70	7.43	0.275	1.12	3.31e+00	1.77e-01	7.80e-02
7.70 - 8.20	7.94	0.276	1.17	2.93e+00	1.67e-01	5.92e-02
8.20 - 8.70	8.44	0.275	1.26	2.69e+00	1.53e-01	5.86e-02
10.85 - 11.85	11.23	0.278	1.19	6.93e-01	1.09e-01	5.55e-02
11.85 - 12.85	12.29	0.282	1.31	4.83e-01	1.71e-01	5.21e-02
12.85 - 14.85	13.31	0.278	1.57	4.68e-01	3.33e-01	5.77e-02

Table 5.1: continued

Mass [GeV]	$< M >$	$< x_F >$	$< p_T >$	$0.30 \leq x_F < 0.35$	Stat. Error	Syst. Error
4.20 - 4.70	4.45	0.324	1.03	1.00e+01	4.63e-01	2.09e-01
4.70 - 5.20	4.95	0.325	1.01	8.85e+00	4.15e-01	2.02e-01
5.20 - 5.70	5.45	0.326	1.02	6.91e+00	3.03e-01	1.89e-01
5.70 - 6.20	5.95	0.325	1.02	5.86e+00	2.31e-01	1.21e-01
6.20 - 6.70	6.44	0.324	1.03	4.72e+00	1.98e-01	8.29e-02
6.70 - 7.20	6.94	0.325	1.11	4.03e+00	1.78e-01	1.01e-01
7.20 - 7.70	7.45	0.325	1.15	3.37e+00	1.50e-01	7.64e-02
7.70 - 8.20	7.93	0.325	1.17	2.51e+00	1.41e-01	4.85e-02
8.20 - 8.70	8.43	0.325	1.19	2.22e+00	1.33e-01	4.33e-02
10.85 - 11.85	11.32	0.326	1.27	6.56e-01	8.22e-02	5.27e-02
11.85 - 12.85	12.26	0.328	1.12	9.65e-01	4.94e-01	4.78e-02
12.85 - 14.85	13.30	0.329	1.31	4.92e-01	1.78e-01	4.26e-02
Mass [GeV]	$< M >$	$< x_F >$	$< p_T >$	$0.35 \leq x_F < 0.40$	Stat. Error	Syst. Error
4.20 - 4.70	4.46	0.374	1.02	7.82e+00	4.14e-01	2.43e-01
4.70 - 5.20	4.95	0.376	1.04	6.54e+00	3.20e-01	2.26e-01
5.20 - 5.70	5.45	0.375	1.02	5.87e+00	3.87e-01	4.67e-01
5.70 - 6.20	5.96	0.375	0.99	4.78e+00	2.64e-01	1.63e-01
6.20 - 6.70	6.45	0.375	1.05	3.86e+00	1.62e-01	6.75e-02
6.70 - 7.20	6.94	0.375	1.10	3.30e+00	1.48e-01	9.22e-02
7.20 - 7.70	7.44	0.376	1.17	2.67e+00	1.21e-01	8.27e-02
7.70 - 8.20	7.95	0.375	1.13	2.21e+00	1.24e-01	6.03e-02
8.20 - 8.70	8.44	0.374	1.16	1.90e+00	1.09e-01	4.06e-02
10.85 - 11.85	11.32	0.375	1.15	4.27e-01	7.23e-02	5.12e-03
11.85 - 12.85	12.26	0.374	1.29	3.45e-01	6.23e-02	1.31e-02
12.85 - 14.85	13.43	0.377	1.31	3.77e-01	1.91e-01	1.30e-02

Table 5.1: continued

Mass [GeV]	$< M >$	$< x_F >$	$< p_T >$	$0.40 \leq x_F < 0.45$	Stat. Error	Syst. Error
4.20 - 4.70	4.46	0.424	0.99	6.45e+00	3.68e-01	2.25e-01
4.70 - 5.20	4.97	0.423	1.01	5.32e+00	2.50e-01	1.52e-01
5.20 - 5.70	5.46	0.424	0.97	4.13e+00	1.93e-01	1.28e-01
5.70 - 6.20	5.95	0.425	1.01	3.76e+00	1.53e-01	8.14e-02
6.20 - 6.70	6.45	0.424	1.02	3.20e+00	1.24e-01	8.05e-02
6.70 - 7.20	6.95	0.424	1.12	2.50e+00	1.16e-01	6.28e-02
7.20 - 7.70	7.45	0.424	1.12	2.04e+00	1.02e-01	5.64e-02
7.70 - 8.20	7.94	0.424	1.15	1.64e+00	9.63e-02	5.20e-02
8.20 - 8.70	8.44	0.424	1.20	1.50e+00	9.25e-02	5.29e-02
10.85 - 11.85	11.28	0.423	1.36	3.63e-01	4.95e-02	8.00e-03
11.85 - 12.85	12.24	0.424	1.29	2.46e-01	5.32e-02	2.24e-02
12.85 - 14.85	13.46	0.429	1.41	6.71e-01	5.45e-01	2.18e-02
Mass [GeV]	$< M >$	$< x_F >$	$< p_T >$	$0.45 \leq x_F < 0.50$	Stat. Error	Syst. Error
4.20 - 4.70	4.46	0.473	0.95	4.20e+00	2.80e-01	1.27e-01
4.70 - 5.20	4.95	0.475	0.99	3.55e+00	2.12e-01	9.38e-02
5.20 - 5.70	5.46	0.475	0.99	3.22e+00	1.54e-01	6.59e-02
5.70 - 6.20	5.95	0.474	0.97	2.54e+00	1.20e-01	5.07e-02
6.20 - 6.70	6.44	0.474	1.03	1.89e+00	9.63e-02	3.76e-02
6.70 - 7.20	6.94	0.474	1.09	1.88e+00	9.42e-02	5.12e-02
7.20 - 7.70	7.43	0.474	1.06	1.50e+00	8.66e-02	5.23e-02
7.70 - 8.20	7.94	0.473	1.08	1.21e+00	8.03e-02	2.65e-02
8.20 - 8.70	8.44	0.474	1.24	8.83e-01	7.12e-02	2.05e-02
10.85 - 11.85	11.29	0.472	1.24	2.50e-01	4.24e-02	8.17e-03
11.85 - 12.85	12.33	0.471	1.18	1.74e-01	4.25e-02	6.59e-03
12.85 - 14.85	13.49	0.474	0.90	9.36e-02	3.83e-02	8.91e-03

Table 5.1: continued

Mass [GeV]	$< M >$	$< x_F >$	$< p_T >$	$0.50 \leq x_F < 0.55$	Stat. Error	Syst. Error
4.20 - 4.70	4.48	0.524	1.04	2.81e+00	2.42e-01	1.13e-01
4.70 - 5.20	4.97	0.524	1.01	2.56e+00	1.76e-01	1.14e-01
5.20 - 5.70	5.46	0.523	1.01	2.28e+00	1.23e-01	6.86e-02
5.70 - 6.20	5.94	0.524	1.00	1.83e+00	9.65e-02	6.27e-02
6.20 - 6.70	6.45	0.525	1.03	1.51e+00	7.93e-02	3.54e-02
6.70 - 7.20	6.93	0.523	1.07	1.27e+00	7.58e-02	3.37e-02
7.20 - 7.70	7.44	0.523	1.07	9.84e-01	7.11e-02	2.33e-02
7.70 - 8.20	7.94	0.523	1.14	9.85e-01	7.06e-02	2.27e-02
8.20 - 8.70	8.45	0.523	1.18	8.52e-01	6.21e-02	1.93e-02
10.85 - 11.85	11.23	0.527	1.14	1.84e-01	3.27e-02	1.28e-03
11.85 - 12.85	12.16	0.525	1.24	7.93e-02	2.51e-02	2.80e-03
12.85 - 14.85	13.46	0.524	1.12	1.69e-01	7.29e-02	1.30e-02
14.85 - 16.85	14.87	0.531	0.77	1.80e+00	1.80e+00	6.50e-01
Mass [GeV]	$< M >$	$< x_F >$	$< p_T >$	$0.55 \leq x_F < 0.60$	Stat. Error	Syst. Error
4.20 - 4.70	4.46	0.571	0.97	1.45e+00	1.61e-01	6.48e-02
4.70 - 5.20	4.96	0.575	0.97	1.57e+00	1.20e-01	6.31e-02
5.20 - 5.70	5.45	0.573	0.91	1.44e+00	9.82e-02	3.99e-02
5.70 - 6.20	5.96	0.573	0.89	1.16e+00	7.25e-02	3.03e-02
6.20 - 6.70	6.44	0.573	1.00	1.15e+00	7.83e-02	2.50e-02
6.70 - 7.20	6.94	0.572	1.06	8.69e-01	6.05e-02	1.99e-02
7.20 - 7.70	7.42	0.573	1.09	7.86e-01	5.48e-02	1.84e-02
7.70 - 8.20	7.94	0.572	1.16	6.01e-01	5.13e-02	2.25e-02
8.20 - 8.70	8.44	0.573	1.03	5.52e-01	5.05e-02	1.82e-02
10.85 - 11.85	11.26	0.570	1.16	1.16e-01	2.27e-02	4.33e-03
11.85 - 12.85	12.21	0.576	1.03	9.16e-02	2.83e-02	6.40e-03

Table 5.1: continued

Mass [GeV]	$< M >$	$< x_F >$	$< p_T >$	$0.55 \leq x_F < 0.60$	Stat. Error	Syst. Error
12.85 - 14.85	13.28	0.570	1.14	2.50e-01	2.02e-01	5.16e-03
Mass [GeV]	$< M >$	$< x_F >$	$< p_T >$	$0.60 \leq x_F < 0.65$	Stat. Error	Syst. Error
4.20 - 4.70	4.49	0.622	0.95	1.41e+00	1.74e-01	8.92e-02
4.70 - 5.20	4.96	0.623	0.94	9.66e-01	1.14e-01	5.80e-02
5.20 - 5.70	5.46	0.622	0.93	8.05e-01	8.03e-02	3.26e-02
5.70 - 6.20	5.96	0.623	0.95	7.15e-01	5.35e-02	2.29e-02
6.20 - 6.70	6.43	0.623	1.02	6.39e-01	5.76e-02	2.27e-02
6.70 - 7.20	6.93	0.624	1.02	6.79e-01	5.35e-02	2.52e-02
7.20 - 7.70	7.44	0.623	1.02	5.44e-01	6.51e-02	3.05e-02
7.70 - 8.20	7.93	0.624	1.03	3.85e-01	4.04e-02	1.19e-02
8.20 - 8.70	8.45	0.624	1.08	3.08e-01	3.93e-02	1.04e-02
10.85 - 11.85	11.24	0.625	1.13	1.09e-01	3.33e-02	6.55e-03
11.85 - 12.85	12.18	0.620	1.34	6.14e-02	2.93e-02	5.11e-03
12.85 - 14.85	13.16	0.609	0.67	2.48e-02	1.13e-02	2.18e-03
Mass [GeV]	$< M >$	$< x_F >$	$< p_T >$	$0.65 \leq x_F < 0.70$	Stat. Error	Syst. Error
4.20 - 4.70	4.47	0.673	0.97	6.90e-01	1.18e-01	6.38e-02
4.70 - 5.20	4.97	0.670	0.90	5.91e-01	7.45e-02	3.13e-02
5.20 - 5.70	5.45	0.670	0.88	6.39e-01	7.28e-02	3.90e-02
5.70 - 6.20	5.95	0.673	0.89	4.48e-01	6.71e-02	1.74e-02
6.20 - 6.70	6.46	0.671	0.92	3.80e-01	5.04e-02	1.68e-02
6.70 - 7.20	6.94	0.669	1.03	2.48e-01	3.91e-02	1.40e-02
7.20 - 7.70	7.43	0.673	1.06	1.97e-01	4.09e-02	1.65e-02
7.70 - 8.20	7.95	0.670	1.08	2.21e-01	3.71e-02	1.27e-02
8.20 - 8.70	8.43	0.669	1.07	1.04e-01	2.42e-02	5.03e-03
10.85 - 11.85	11.30	0.674	1.22	5.25e-02	1.52e-02	2.79e-03

Table 5.1: continued

Mass [GeV]	$< M >$	$< x_F >$	$< p_T >$	$0.65 \leq x_F < 0.70$	Stat. Error	Syst. Error
11.85 - 12.85	12.42	0.679	1.27	3.87e-02	2.09e-02	3.70e-03
12.85 - 14.85	13.77	0.677	0.83	9.03e-02	4.41e-02	3.04e-03
Mass [GeV]	$< M >$	$< x_F >$	$< p_T >$	$0.70 \leq x_F < 0.75$	Stat. Error	Syst. Error
4.20 - 4.70	4.53	0.720	0.80	5.31e-01	1.26e-01	4.75e-02
4.70 - 5.20	5.01	0.720	0.90	4.21e-01	8.97e-02	2.60e-02
5.20 - 5.70	5.45	0.719	0.94	2.44e-01	3.87e-02	1.16e-02
5.70 - 6.20	5.94	0.723	1.04	2.68e-01	4.36e-02	2.31e-02
6.20 - 6.70	6.45	0.720	1.00	2.04e-01	4.72e-02	1.62e-02
6.70 - 7.20	6.93	0.720	0.86	1.62e-01	2.65e-02	1.24e-02
7.20 - 7.70	7.41	0.726	1.00	1.78e-01	3.30e-02	1.06e-02
7.70 - 8.20	7.95	0.719	1.07	3.54e-01	1.61e-01	1.21e-02
8.20 - 8.70	8.42	0.717	1.13	1.05e-01	2.43e-02	1.05e-02
10.85 - 11.85	11.28	0.728	1.30	3.61e-02	2.34e-02	4.30e-04
12.85 - 14.85	13.14	0.723	1.33	3.83e-01	2.72e-01	4.21e-02
Mass [GeV]	$< M >$	$< x_F >$	$< p_T >$	$0.75 \leq x_F < 0.80$	Stat. Error	Syst. Error
4.20 - 4.70	4.48	0.770	1.01	3.20e-01	1.11e-01	5.33e-02
4.70 - 5.20	4.96	0.767	0.84	4.98e-01	2.48e-01	3.98e-02
5.20 - 5.70	5.45	0.768	0.65	1.28e-01	2.67e-02	9.63e-03
5.70 - 6.20	5.95	0.771	0.96	1.76e-01	4.18e-02	1.37e-02
6.20 - 6.70	6.43	0.769	0.82	9.89e-02	2.22e-02	5.33e-03
6.70 - 7.20	6.94	0.767	0.83	8.01e-02	2.43e-02	5.63e-03
7.20 - 7.70	7.45	0.773	0.97	1.09e-01	4.14e-02	1.91e-02
7.70 - 8.20	7.93	0.772	1.42	1.04e-01	3.55e-02	9.37e-03
8.20 - 8.70	8.47	0.776	0.80	7.31e-02	2.44e-02	6.20e-03
10.85 - 11.85	11.39	0.765	1.52	6.65e-02	4.97e-02	5.74e-03

Table 5.2: Scaling form $M^3 d^2\sigma/dMdx_F$ (in units of nb GeV^2 / nucleon) for the deuterium cross section. Statistical and point-to-point systematic uncertainties are shown separately. The normalization is subject to an uncertainty of $\pm$6.5%.

Mass [GeV]	$< M >$	$< x_F >$	$< p_T >$	$-0.05 \leq x_F < 0.05$	Stat. Error	Syst. Error
4.70 - 5.20	4.94	0.044	0.96	4.50e+01	2.77e+01	5.70e-01
5.20 - 5.70	5.40	0.039	0.55	1.81e+01	8.30e+00	2.00e+00
5.70 - 6.20	6.10	0.037	1.04	1.21e+01	4.70e+00	1.46e+00
6.20 - 6.70	6.48	0.022	1.03	1.25e+01	2.75e+00	9.14e-01
6.70 - 7.20	6.95	0.025	0.90	9.76e+00	1.73e+00	4.41e-01
7.20 - 7.70	7.49	0.027	0.97	7.15e+00	2.47e+00	1.12e+00
7.70 - 8.20	8.01	0.024	0.99	5.62e+00	6.72e-01	2.47e-01
8.20 - 8.70	8.45	0.017	0.97	4.32e+00	4.32e-01	2.15e-01
10.85 - 11.85	11.12	0.012	0.44	8.71e-01	3.58e-01	1.75e-02
Mass [GeV]	$< M >$	$< x_F >$	$< p_T >$	$0.05 \leq x_F < 0.10$	Stat. Error	Syst. Error
4.20 - 4.70	4.48	0.084	0.78	2.78e+01	2.08e+00	7.52e-01
4.70 - 5.20	4.92	0.081	0.83	2.18e+01	1.73e+00	7.37e-01
5.20 - 5.70	5.43	0.084	0.77	1.73e+01	2.55e+00	1.11e+00
5.70 - 6.20	5.97	0.080	0.98	1.30e+01	1.81e+00	6.84e-01
6.20 - 6.70	6.46	0.079	0.94	7.82e+00	1.18e+00	4.34e-01
6.70 - 7.20	6.90	0.080	0.90	6.23e+00	1.32e+00	4.38e-01
7.20 - 7.70	7.50	0.082	0.91	6.18e+00	1.21e+00	5.15e-01
7.70 - 8.20	7.97	0.078	1.03	4.18e+00	3.05e-01	2.02e-01
8.20 - 8.70	8.45	0.076	1.03	3.58e+00	2.51e-01	1.58e-01
10.85 - 11.85	11.21	0.085	0.98	1.84e+00	6.56e-01	7.84e-03

Table 5.2: continued

Mass [GeV]	$< M >$	$< x_F >$	$< p_T >$	$0.10 \leq x_F < 0.15$	Stat. Error	Syst. Error
4.20 - 4.70	4.44	0.130	0.91	2.64e+01	9.63e-01	4.98e-01
4.70 - 5.20	4.93	0.128	0.86	1.72e+01	7.96e-01	3.55e-01
5.20 - 5.70	5.42	0.129	0.92	1.45e+01	1.01e+00	4.16e-01
5.70 - 6.20	5.93	0.130	0.98	1.02e+01	7.86e-01	2.91e-01
6.20 - 6.70	6.45	0.129	0.93	8.98e+00	8.55e-01	2.84e-01
6.70 - 7.20	6.97	0.130	1.04	7.18e+00	6.49e-01	2.73e-01
7.20 - 7.70	7.49	0.128	1.07	5.91e+00	4.46e-01	1.97e-01
7.70 - 8.20	7.95	0.129	1.13	4.92e+00	2.49e-01	1.82e-01
8.20 - 8.70	8.45	0.127	1.13	3.86e+00	1.87e-01	1.02e-01
10.85 - 11.85	11.20	0.126	1.17	1.44e+00	3.19e-01	1.55e-01
11.85 - 12.85	12.03	0.135	1.72	2.12e+00	1.04e+00	9.62e-02

Mass [GeV]	$< M >$	$< x_F >$	$< p_T >$	$0.15 \leq x_F < 0.20$	Stat. Error	Syst. Error
4.20 - 4.70	4.43	0.177	1.03	2.17e+01	6.01e-01	4.30e-01
4.70 - 5.20	4.93	0.177	1.00	1.68e+01	5.27e-01	3.45e-01
5.20 - 5.70	5.43	0.177	0.97	1.17e+01	6.14e-01	2.86e-01
5.70 - 6.20	5.92	0.178	1.00	1.05e+01	5.32e-01	2.30e-01
6.20 - 6.70	6.46	0.179	1.08	7.81e+00	4.77e-01	2.93e-01
6.70 - 7.20	6.98	0.179	1.08	6.90e+00	3.01e-01	2.73e-01
7.20 - 7.70	7.44	0.176	1.11	5.35e+00	2.25e-01	1.52e-01
7.70 - 8.20	7.95	0.176	1.15	4.46e+00	1.73e-01	1.29e-01
8.20 - 8.70	8.43	0.176	1.16	3.63e+00	1.41e-01	7.58e-02
10.85 - 11.85	11.24	0.178	1.11	1.17e+00	2.06e-01	5.42e-02
11.85 - 12.85	12.06	0.166	0.91	5.16e-01	1.91e-01	5.58e-02
12.85 - 14.85	13.13	0.195	1.25	1.82e+00	1.79e+00	5.40e-02

Table 5.2: continued

Mass [GeV]	$< M >$	$< x_F >$	$< p_T >$	$0.20 \leq x_F < 0.25$	Stat. Error	Syst. Error
4.20 - 4.70	4.44	0.225	1.04	1.82e+01	4.23e-01	3.32e-01
4.70 - 5.20	4.93	0.225	1.01	1.35e+01	4.00e-01	2.44e-01
5.20 - 5.70	5.43	0.226	1.00	1.03e+01	3.93e-01	2.06e-01
5.70 - 6.20	5.94	0.227	1.03	8.80e+00	3.40e-01	2.30e-01
6.20 - 6.70	6.46	0.229	1.05	7.77e+00	2.64e-01	1.91e-01
6.70 - 7.20	6.95	0.227	1.09	5.87e+00	1.87e-01	1.15e-01
7.20 - 7.70	7.43	0.226	1.11	4.73e+00	1.55e-01	1.16e-01
7.70 - 8.20	7.94	0.226	1.18	4.06e+00	1.35e-01	1.02e-01
8.20 - 8.70	8.45	0.225	1.17	3.35e+00	1.24e-01	6.75e-02
10.85 - 11.85	11.17	0.227	1.25	7.07e-01	7.43e-02	1.97e-02
11.85 - 12.85	12.31	0.226	1.23	5.63e-01	1.38e-01	4.95e-02
12.85 - 14.85	13.19	0.229	0.85	3.61e-01	1.48e-01	2.88e-02
Mass [GeV]	$< M >$	$< x_F >$	$< p_T >$	$0.25 \leq x_F < 0.30$	Stat. Error	Syst. Error
4.20 - 4.70	4.44	0.275	1.01	1.46e+01	3.45e-01	2.39e-01
4.70 - 5.20	4.94	0.275	1.03	1.15e+01	3.20e-01	1.97e-01
5.20 - 5.70	5.45	0.276	1.02	9.32e+00	2.96e-01	2.30e-01
5.70 - 6.20	5.95	0.277	1.01	7.72e+00	1.98e-01	2.19e-01
6.20 - 6.70	6.45	0.276	1.02	6.47e+00	1.72e-01	1.68e-01
6.70 - 7.20	6.95	0.276	1.08	5.15e+00	1.39e-01	8.95e-02
7.20 - 7.70	7.44	0.275	1.15	4.11e+00	1.21e-01	9.33e-02
7.70 - 8.20	7.94	0.276	1.19	3.29e+00	1.08e-01	6.60e-02
8.20 - 8.70	8.45	0.275	1.20	2.85e+00	1.01e-01	5.41e-02
10.85 - 11.85	11.23	0.275	1.19	8.09e-01	6.51e-02	2.10e-02
11.85 - 12.85	12.23	0.278	1.04	3.41e-01	8.92e-02	2.38e-02
12.85 - 14.85	13.42	0.270	1.29	4.11e-01	2.70e-01	2.52e-02

Table 5.2: continued

Mass [GeV]	$< M >$	$< x_F >$	$< p_T >$	$0.30 \leq x_F < 0.35$	Stat. Error	Syst. Error
4.20 - 4.70	4.44	0.323	1.04	1.13e+01	3.26e-01	2.56e-01
4.70 - 5.20	4.95	0.325	1.05	8.45e+00	2.57e-01	1.86e-01
5.20 - 5.70	5.45	0.325	1.00	8.01e+00	2.07e-01	1.77e-01
5.70 - 6.20	5.95	0.325	1.02	6.21e+00	1.54e-01	1.53e-01
6.20 - 6.70	6.45	0.325	1.07	5.23e+00	1.30e-01	8.99e-02
6.70 - 7.20	6.95	0.325	1.10	4.45e+00	1.16e-01	8.46e-02
7.20 - 7.70	7.44	0.325	1.15	3.57e+00	9.93e-02	7.96e-02
7.70 - 8.20	7.93	0.325	1.22	2.98e+00	9.51e-02	5.55e-02
8.20 - 8.70	8.44	0.325	1.19	2.48e+00	8.81e-02	4.77e-02
10.85 - 11.85	11.29	0.326	1.11	5.01e-01	4.47e-02	2.97e-02
11.85 - 12.85	12.17	0.326	1.18	5.05e-01	1.10e-01	3.74e-02
12.85 - 14.85	13.41	0.328	1.16	3.18e-01	1.06e-01	1.92e-02
Mass [GeV]	$< M >$	$< x_F >$	$< p_T >$	$0.35 \leq x_F < 0.40$	Stat. Error	Syst. Error
4.20 - 4.70	4.45	0.375	1.00	7.97e+00	2.55e-01	1.80e-01
4.70 - 5.20	4.96	0.374	1.01	6.47e+00	1.93e-01	1.81e-01
5.20 - 5.70	5.46	0.375	0.99	5.90e+00	1.58e-01	9.73e-02
5.70 - 6.20	5.95	0.374	1.02	4.91e+00	1.20e-01	8.34e-02
6.20 - 6.70	6.44	0.374	1.06	4.08e+00	1.03e-01	6.99e-02
6.70 - 7.20	6.94	0.374	1.10	3.50e+00	9.44e-02	9.94e-02
7.20 - 7.70	7.44	0.374	1.16	2.92e+00	8.24e-02	1.01e-01
7.70 - 8.20	7.94	0.375	1.15	2.51e+00	8.00e-02	1.10e-01
8.20 - 8.70	8.44	0.374	1.18	2.08e+00	7.96e-02	8.28e-02
10.85 - 11.85	11.27	0.375	1.16	5.13e-01	4.04e-02	4.33e-03
11.85 - 12.85	12.29	0.376	1.17	2.05e-01	3.65e-02	1.12e-02
12.85 - 14.85	13.31	0.378	1.08	1.94e-01	4.76e-02	1.20e-02

Table 5.2: continued

Mass [GeV]	$< M >$	$< x_F >$	$< p_T >$	$0.35 \leq x_F < 0.40$	Stat. Error	Syst. Error
14.85 - 16.85	15.48	0.390	1.64	2.40e-01	1.77e-01	1.76e-01
Mass [GeV]	$< M >$	$< x_F >$	$< p_T >$	$0.40 \leq x_F < 0.45$	Stat. Error	Syst. Error
4.20 - 4.70	4.45	0.423	1.03	6.09e+00	2.22e-01	1.68e-01
4.70 - 5.20	4.96	0.424	0.99	5.09e+00	1.58e-01	1.59e-01
5.20 - 5.70	5.46	0.424	0.99	4.28e+00	1.22e-01	1.29e-01
5.70 - 6.20	5.95	0.424	1.00	3.78e+00	9.71e-02	1.10e-01
6.20 - 6.70	6.45	0.424	1.02	3.12e+00	8.00e-02	7.37e-02
6.70 - 7.20	6.93	0.424	1.08	2.60e+00	7.43e-02	6.73e-02
7.20 - 7.70	7.44	0.424	1.12	2.10e+00	6.57e-02	4.68e-02
7.70 - 8.20	7.94	0.425	1.13	1.86e+00	6.46e-02	6.32e-02
8.20 - 8.70	8.44	0.424	1.18	1.63e+00	6.21e-02	4.68e-02
10.85 - 11.85	11.26	0.425	1.17	4.33e-01	3.40e-02	1.10e-02
11.85 - 12.85	12.23	0.427	1.27	2.70e-01	3.32e-02	1.10e-02
12.85 - 14.85	13.56	0.426	1.15	1.39e-01	2.81e-02	6.47e-03
14.85 - 16.85	15.59	0.434	1.29	4.24e-01	2.41e-01	1.20e-01
Mass [GeV]	$< M >$	$< x_F >$	$< p_T >$	$0.45 \leq x_F < 0.50$	Stat. Error	Syst. Error
4.20 - 4.70	4.46	0.473	1.00	4.49e+00	2.03e-01	3.45e-01
4.70 - 5.20	4.96	0.474	0.97	3.68e+00	1.31e-01	1.16e-01
5.20 - 5.70	5.46	0.474	1.01	3.07e+00	9.86e-02	6.13e-02
5.70 - 6.20	5.95	0.474	0.99	2.75e+00	7.76e-02	5.63e-02
6.20 - 6.70	6.44	0.475	1.02	2.29e+00	6.88e-02	5.10e-02
6.70 - 7.20	6.94	0.474	1.07	1.91e+00	6.02e-02	4.62e-02
7.20 - 7.70	7.44	0.473	1.16	1.57e+00	5.62e-02	3.89e-02
7.70 - 8.20	7.93	0.474	1.13	1.33e+00	5.24e-02	2.79e-02
8.20 - 8.70	8.44	0.474	1.08	1.21e+00	7.74e-02	1.68e-02

Table 5.2: continued

Mass [GeV]	$< M >$	$< x_F >$	$< p_T >$	$0.45 \leq x_F < 0.50$	Stat. Error	Syst. Error
10.85 - 11.85	11.31	0.476	1.19	3.62e-01	3.11e-02	1.06e-02
11.85 - 12.85	12.26	0.475	1.09	2.01e-01	2.96e-02	7.79e-03
12.85 - 14.85	13.43	0.471	1.08	1.01e-01	2.71e-02	4.90e-03
14.85 - 16.85	16.62	0.466	0.96	7.46e-02	7.46e-02	2.04e-02
Mass [GeV]	$< M >$	$< x_F >$	$< p_T >$	$0.50 \leq x_F < 0.55$	Stat. Error	Syst. Error
4.20 - 4.70	4.46	0.523	0.97	3.08e+00	1.60e-01	1.55e-01
4.70 - 5.20	4.97	0.525	0.99	2.57e+00	1.11e-01	1.79e-01
5.20 - 5.70	5.46	0.524	0.95	2.08e+00	7.41e-02	7.49e-02
5.70 - 6.20	5.95	0.524	0.97	1.95e+00	6.28e-02	5.96e-02
6.20 - 6.70	6.45	0.524	0.97	1.66e+00	5.34e-02	3.90e-02
6.70 - 7.20	6.95	0.524	1.07	1.29e+00	4.83e-02	3.00e-02
7.20 - 7.70	7.44	0.523	1.05	1.16e+00	4.65e-02	2.67e-02
7.70 - 8.20	7.93	0.523	1.11	9.72e-01	4.40e-02	3.70e-02
8.20 - 8.70	8.44	0.524	1.16	8.48e-01	4.03e-02	2.75e-02
10.85 - 11.85	11.30	0.522	1.14	2.00e-01	2.14e-02	8.15e-03
11.85 - 12.85	12.27	0.527	1.03	1.23e-01	2.46e-02	8.66e-03
12.85 - 14.85	13.55	0.524	1.19	8.12e-02	1.94e-02	3.91e-03
Mass [GeV]	$< M >$	$< x_F >$	$< p_T >$	$0.55 \leq x_F < 0.60$	Stat. Error	Syst. Error
4.20 - 4.70	4.47	0.572	1.04	2.17e+00	1.37e-01	9.50e-02
4.70 - 5.20	4.97	0.574	0.96	1.75e+00	8.45e-02	6.55e-02
5.20 - 5.70	5.45	0.574	1.00	1.51e+00	6.37e-02	4.53e-02
5.70 - 6.20	5.95	0.574	0.96	1.29e+00	4.89e-02	2.80e-02
6.20 - 6.70	6.44	0.573	1.02	1.07e+00	4.29e-02	2.27e-02
6.70 - 7.20	6.94	0.572	1.02	9.56e-01	3.99e-02	2.22e-02
7.20 - 7.70	7.44	0.573	1.08	7.75e-01	3.52e-02	1.78e-02

Table 5.2: continued

Mass [GeV]	$< M >$	$< x_F >$	$< p_T >$	$0.55 \leq x_F < 0.60$	Stat. Error	Syst. Error
7.70 - 8.20	7.93	0.573	1.04	6.78e-01	3.54e-02	2.12e-02
8.20 - 8.70	8.44	0.573	1.10	6.17e-01	3.44e-02	2.01e-02
10.85 - 11.85	11.26	0.574	1.12	1.48e-01	1.71e-02	2.14e-03
11.85 - 12.85	12.35	0.574	1.23	1.11e-01	1.96e-02	5.64e-03
12.85 - 14.85	13.51	0.572	1.11	6.24e-02	1.77e-02	8.75e-03
14.85 - 16.85	15.19	0.597	0.56	6.89e-03	6.89e-03	2.44e-03
Mass [GeV]	$< M >$	$< x_F >$	$< p_T >$	$0.60 \leq x_F < 0.65$	Stat. Error	Syst. Error
4.20 - 4.70	4.48	0.624	1.01	1.13e+00	9.93e-02	5.28e-02
4.70 - 5.20	4.96	0.623	0.92	1.07e+00	6.80e-02	4.01e-02
5.20 - 5.70	5.47	0.624	0.90	8.64e-01	4.54e-02	3.58e-02
5.70 - 6.20	5.96	0.622	0.94	7.77e-01	4.28e-02	2.64e-02
6.20 - 6.70	6.45	0.623	0.92	6.47e-01	3.39e-02	2.70e-02
6.70 - 7.20	6.94	0.622	0.99	5.81e-01	3.25e-02	1.73e-02
7.20 - 7.70	7.44	0.624	1.08	4.47e-01	3.15e-02	1.69e-02
7.70 - 8.20	7.96	0.622	1.03	4.30e-01	3.25e-02	1.30e-02
8.20 - 8.70	8.45	0.625	1.09	3.49e-01	2.76e-02	9.92e-03
10.85 - 11.85	11.28	0.621	1.19	9.51e-02	1.42e-02	3.28e-03
11.85 - 12.85	12.33	0.621	1.21	8.06e-02	1.61e-02	6.38e-03
12.85 - 14.85	13.38	0.622	1.25	2.90e-02	7.26e-03	1.73e-03
14.85 - 16.85	15.89	0.623	3.48	4.67e-02	4.67e-02	1.78e-01
Mass [GeV]	$< M >$	$< x_F >$	$< p_T >$	$0.65 \leq x_F < 0.70$	Stat. Error	Syst. Error
4.20 - 4.70	4.48	0.669	0.95	5.85e-01	7.05e-02	5.31e-02
4.70 - 5.20	4.96	0.670	0.93	6.19e-01	4.74e-02	3.13e-02
5.20 - 5.70	5.47	0.673	0.90	5.69e-01	3.99e-02	2.79e-02
5.70 - 6.20	5.96	0.673	0.88	4.49e-01	2.94e-02	1.59e-02

Table 5.2: continued

Mass [GeV]	$< M >$	$< x_F >$	$< p_T >$	$0.65 \leq x_F < 0.70$	Stat. Error	Syst. Error
6.20 - 6.70	6.45	0.673	1.02	4.01e-01	2.91e-02	1.33e-02
6.70 - 7.20	6.95	0.673	0.99	3.65e-01	2.89e-02	1.63e-02
7.20 - 7.70	7.44	0.671	1.11	2.81e-01	2.54e-02	1.25e-02
7.70 - 8.20	7.93	0.671	1.10	2.44e-01	3.18e-02	1.53e-02
8.20 - 8.70	8.43	0.670	1.06	1.91e-01	2.09e-02	9.33e-03
10.85 - 11.85	11.33	0.674	0.97	5.01e-02	1.46e-02	3.46e-03
11.85 - 12.85	12.26	0.675	0.95	4.39e-02	1.34e-02	4.85e-03
12.85 - 14.85	13.52	0.679	0.95	2.01e-02	8.56e-03	5.89e-03
Mass [GeV]	$< M >$	$< x_F >$	$< p_T >$	$0.70 \leq x_F < 0.75$	Stat. Error	Syst. Error
4.20 - 4.70	4.50	0.721	1.03	3.58e-01	6.46e-02	3.68e-02
4.70 - 5.20	4.96	0.722	0.91	3.17e-01	3.93e-02	2.03e-02
5.20 - 5.70	5.47	0.722	0.87	2.08e-01	2.19e-02	1.06e-02
5.70 - 6.20	5.94	0.723	0.82	2.31e-01	3.15e-02	1.44e-02
6.20 - 6.70	6.43	0.723	0.90	1.88e-01	2.83e-02	1.72e-02
6.70 - 7.20	6.95	0.722	0.98	1.69e-01	1.82e-02	8.32e-03
7.20 - 7.70	7.45	0.722	1.00	1.35e-01	1.79e-02	7.68e-03
7.70 - 8.20	7.93	0.721	0.98	1.00e-01	1.42e-02	5.09e-03
8.20 - 8.70	8.42	0.722	0.98	8.28e-02	1.37e-02	4.85e-03
10.85 - 11.85	11.28	0.719	1.16	3.11e-02	7.74e-03	3.80e-03
11.85 - 12.85	12.25	0.733	0.74	3.29e-02	1.42e-02	3.08e-03
12.85 - 14.85	13.68	0.717	1.73	4.94e-03	4.94e-03	1.78e-03
Mass [GeV]	$< M >$	$< x_F >$	$< p_T >$	$0.75 \leq x_F < 0.80$	Stat. Error	Syst. Error
4.20 - 4.70	4.47	0.777	1.20	1.89e-01	6.62e-02	2.48e-02
4.70 - 5.20	4.95	0.773	0.90	1.52e-01	2.82e-02	1.37e-02
5.20 - 5.70	5.44	0.769	0.75	1.02e-01	1.62e-02	6.22e-03

Table 5.2: continued

Mass [GeV]	$< M >$	$< x_F >$	$< p_T >$	$0.75 \leq x_F < 0.80$	Stat. Error	Syst. Error
5.70 - 6.20	5.98	0.770	0.83	1.19e-01	2.45e-02	8.09e-03
6.20 - 6.70	6.45	0.772	0.90	1.27e-01	5.28e-02	8.69e-03
6.70 - 7.20	6.92	0.769	0.93	8.04e-02	1.20e-02	6.24e-03
7.20 - 7.70	7.47	0.769	0.83	4.95e-02	1.09e-02	5.26e-03
7.70 - 8.20	7.88	0.769	1.06	6.40e-02	1.42e-02	6.45e-03
8.20 - 8.70	8.44	0.775	0.93	3.33e-02	1.06e-02	1.48e-03
10.85 - 11.85	11.30	0.770	1.01	1.36e-02	6.22e-03	2.71e-03
11.85 - 12.85	12.30	0.765	1.35	2.08e-02	1.20e-02	3.21e-03
12.85 - 14.85	13.59	0.773	0.61	1.09e-02	1.09e-02	4.06e-03

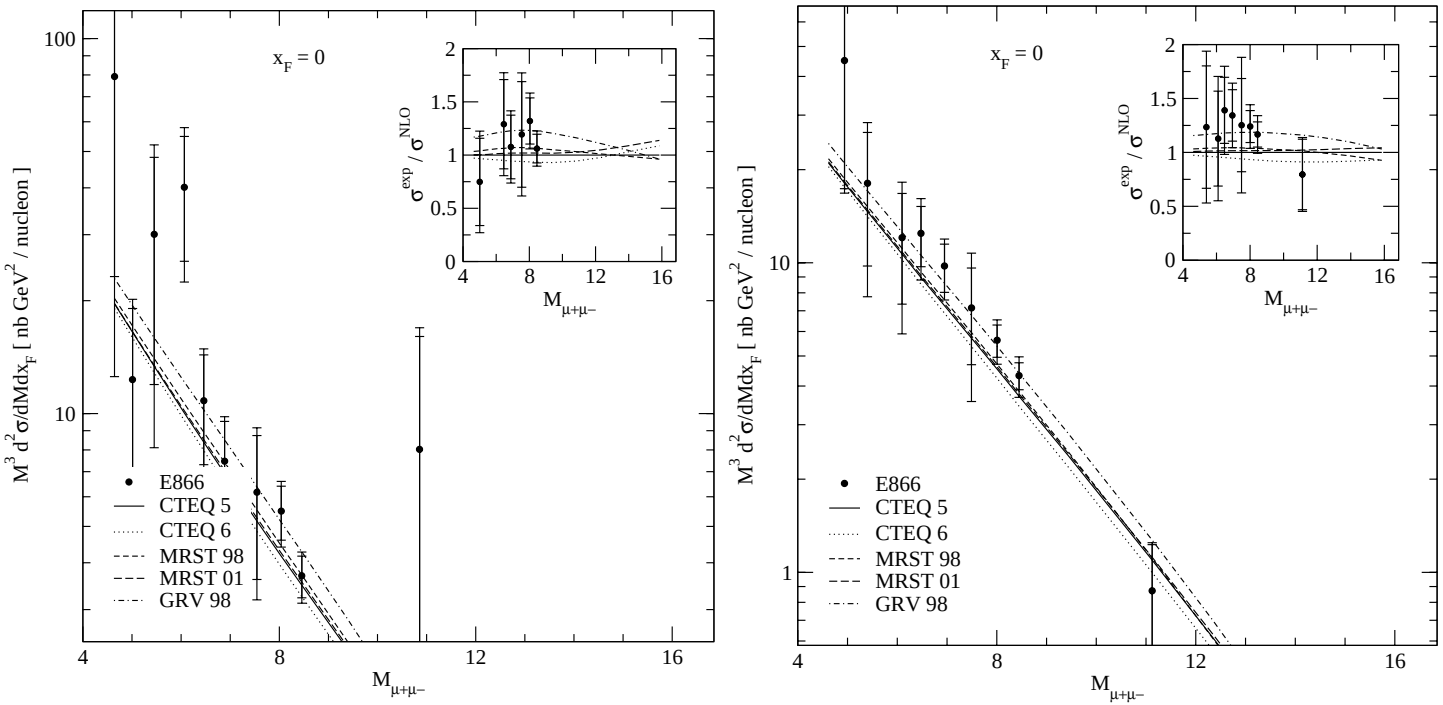

Figure 5.1: Scaling form $M^3 d^2\sigma/dMdx_F$ of the hydrogen (left) and deuterium (right) cross sections for $-0.05 \leq x_F < 0.05$. The data are compared to NLO calculations based on several different sets of parton distributions. The inset shows the ratio of the experimentally measured cross sections to NLO calculations based on the CTEQ 5 partons.

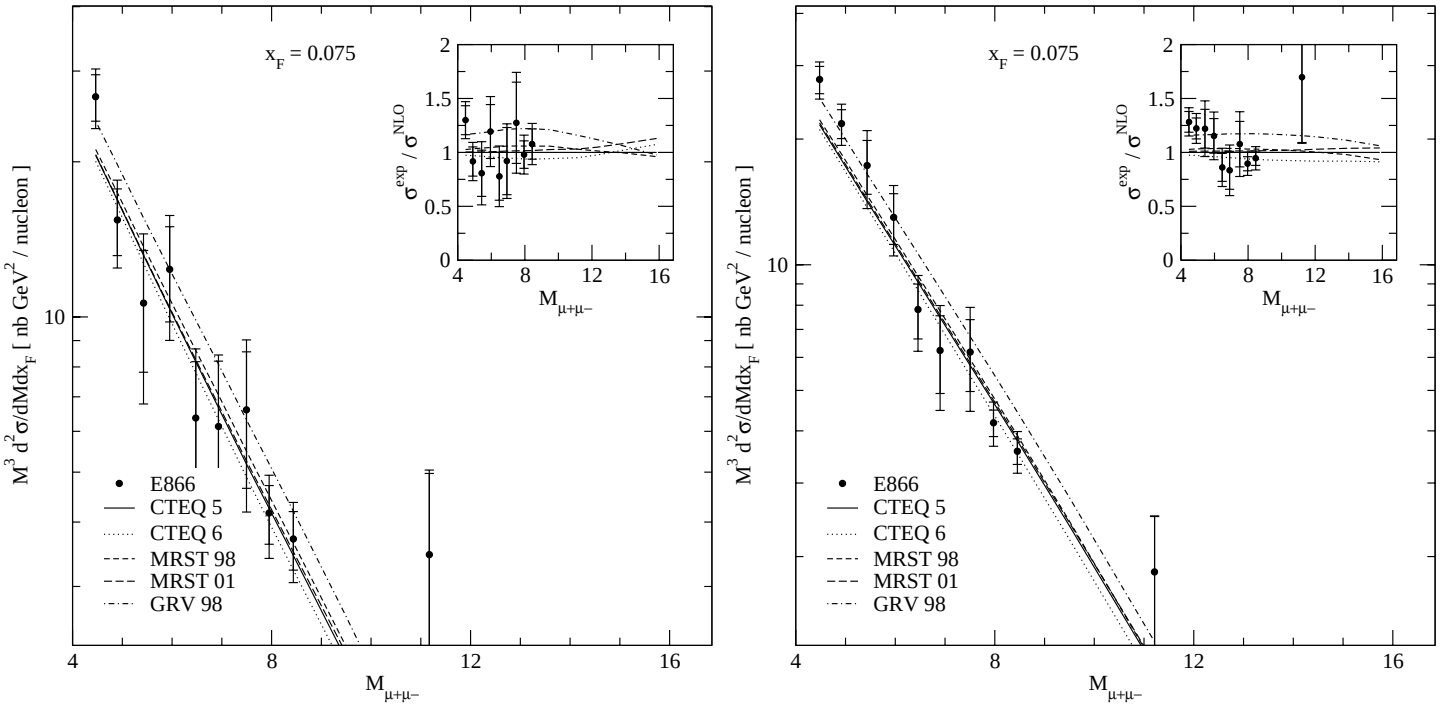

Figure 5.2: Scaling form $M^3 d^2\sigma/dMdx_F$ of the hydrogen (left) and deuterium (right) cross sections for $0.05 \leq x_F < 0.1$. The data are compared to NLO calculations based on several different sets of parton distributions. The inset shows the ratio of the experimentally measured cross sections to NLO calculations based on the CTEQ 5 partons.

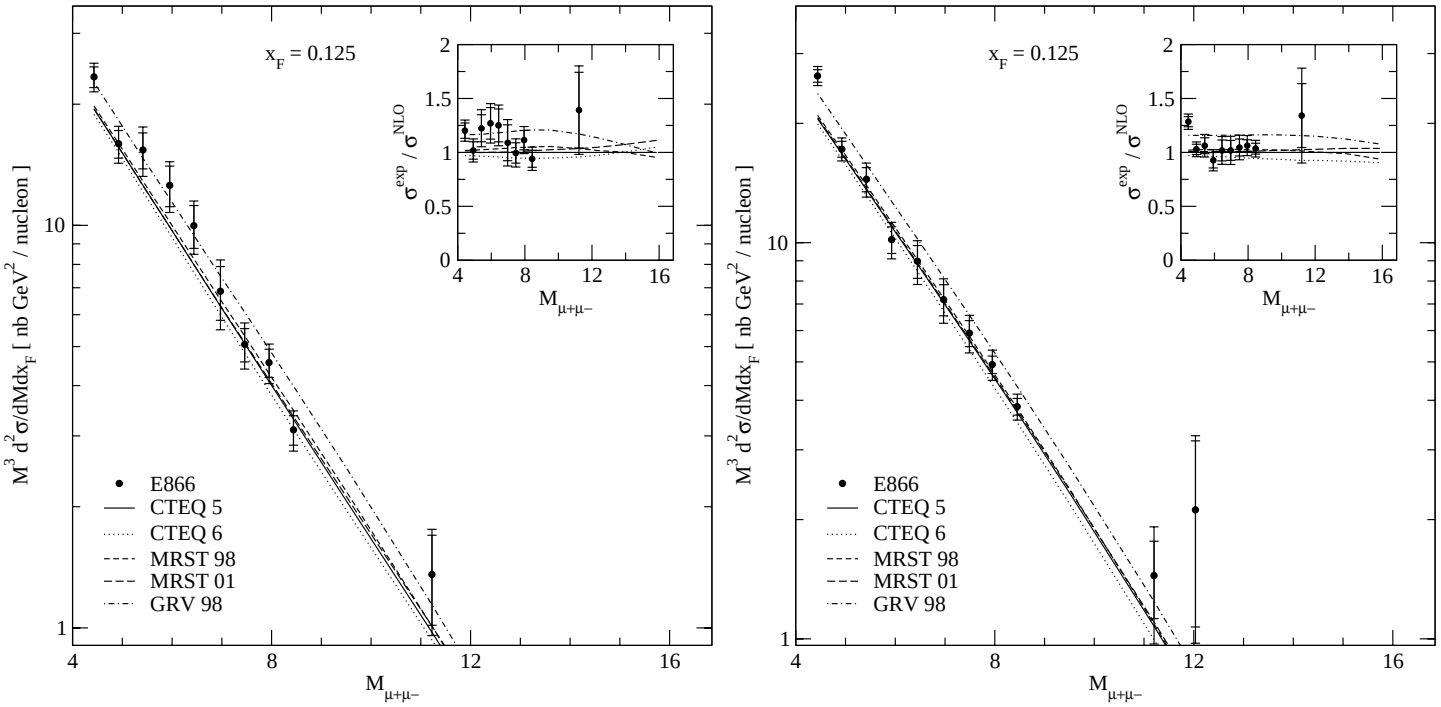

Figure 5.3: Scaling form $M^3 d^2\sigma/dMdx_F$ of the hydrogen (left) and deuterium (right) cross sections for $0.1 \leq x_F < 0.15$. The data are compared to NLO calculations based on several different sets of parton distributions. The inset shows the ratio of the experimentally measured cross sections to NLO calculations based on the CTEQ 5 partons.

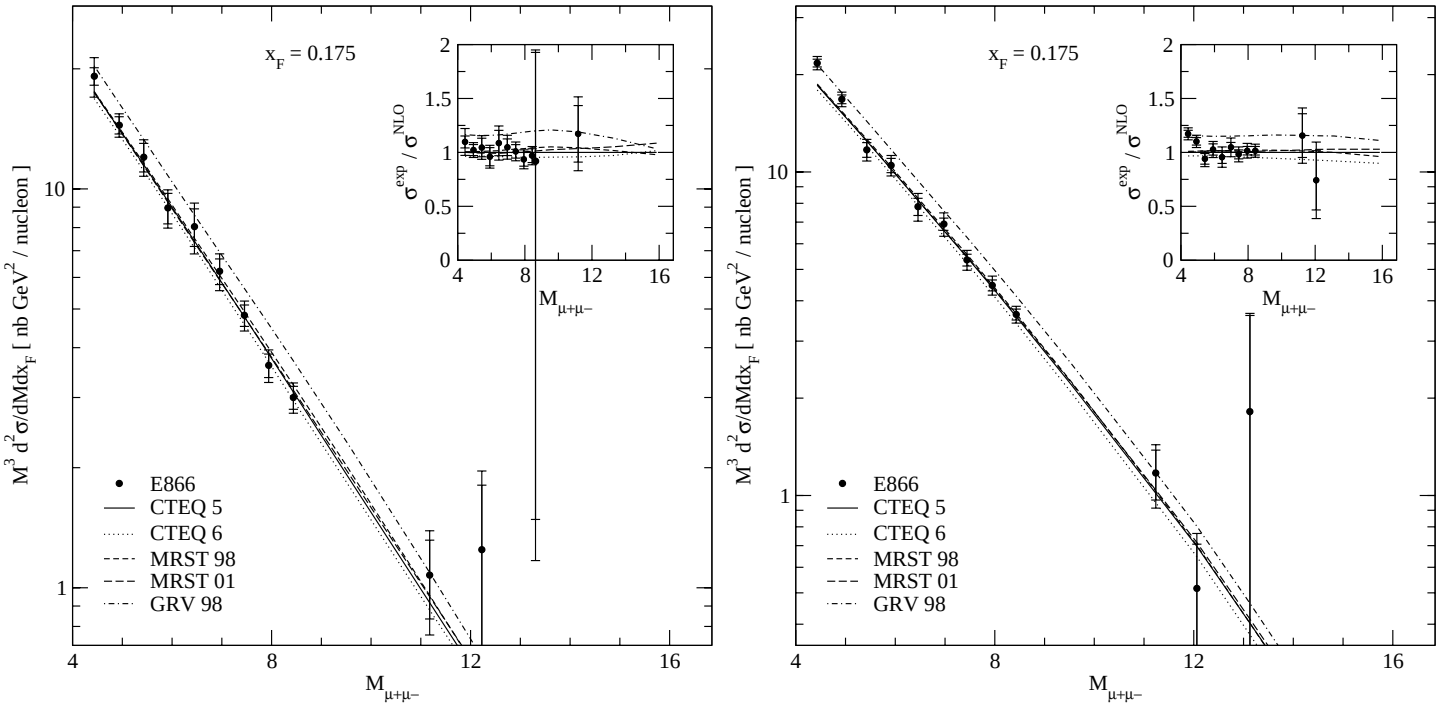

Figure 5.4: Scaling form $M^3 d^2\sigma/dMdx_F$ of the hydrogen (left) and deuterium (right) cross sections for $0.15 \leq x_F < 0.2$. The data are compared to NLO calculations based on several different sets of parton distributions. The inset shows the ratio of the experimentally measured cross sections to NLO calculations based on the CTEQ 5 partons.

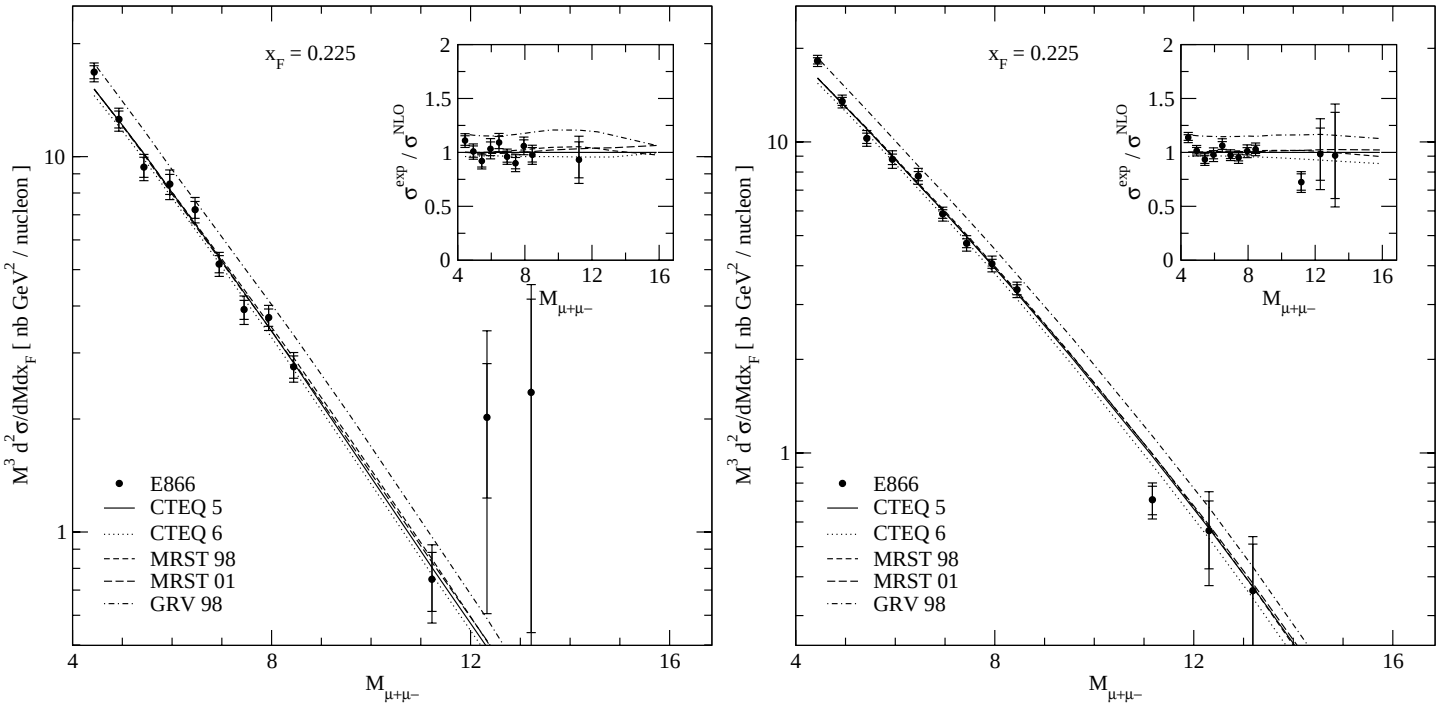

Figure 5.5: Scaling form $M^3 d^2\sigma/dMdx_F$ of the hydrogen (left) and deuterium (right) cross sections for $0.2 \leq x_F < 0.25$. The data are compared to NLO calculations based on several different sets of parton distributions. The inset shows the ratio of the experimentally measured cross sections to NLO calculations based on the CTEQ 5 partons.

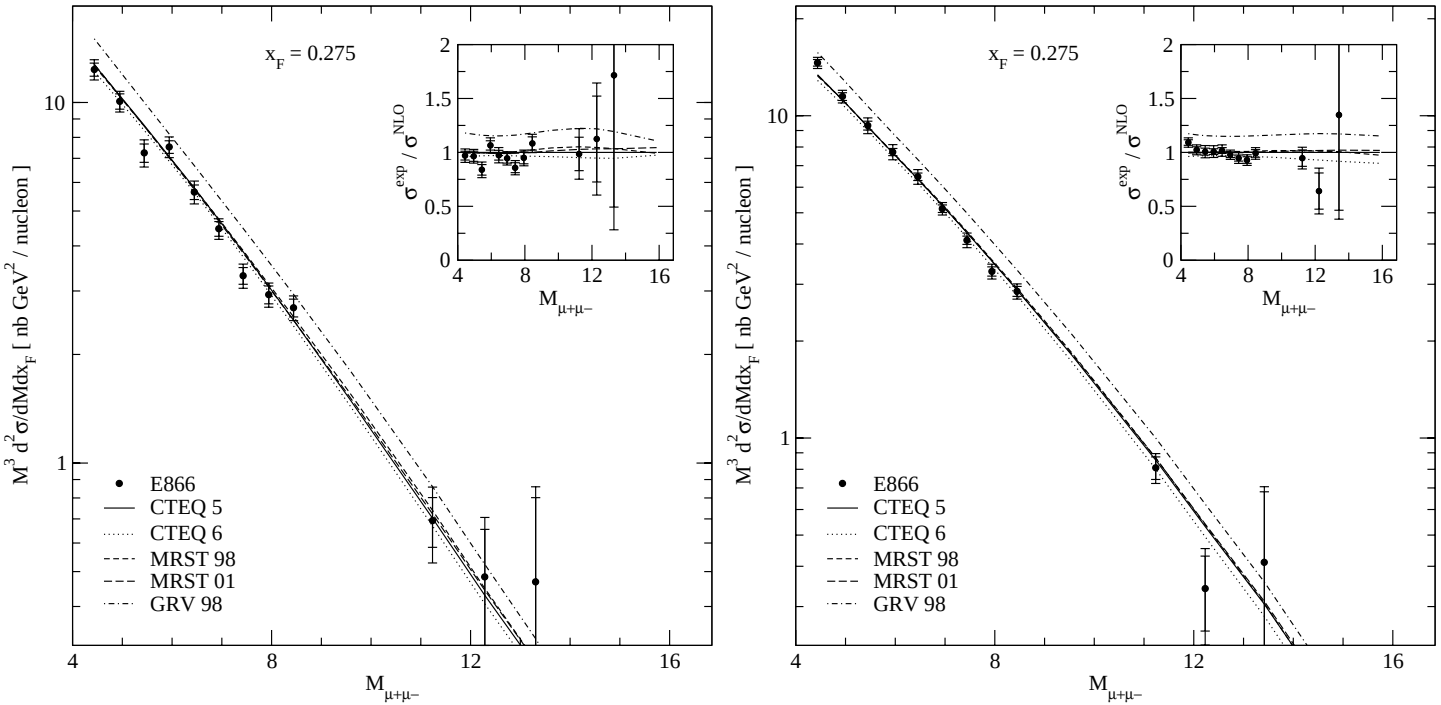

Figure 5.6: Scaling form $M^3 d^2\sigma/dMdx_F$ of the hydrogen (left) and deuterium (right) cross sections for $0.25 \leq x_F < 0.3$. The data are compared to NLO calculations based on several different sets of parton distributions. The inset shows the ratio of the experimentally measured cross sections to NLO calculations based on the CTEQ 5 partons.

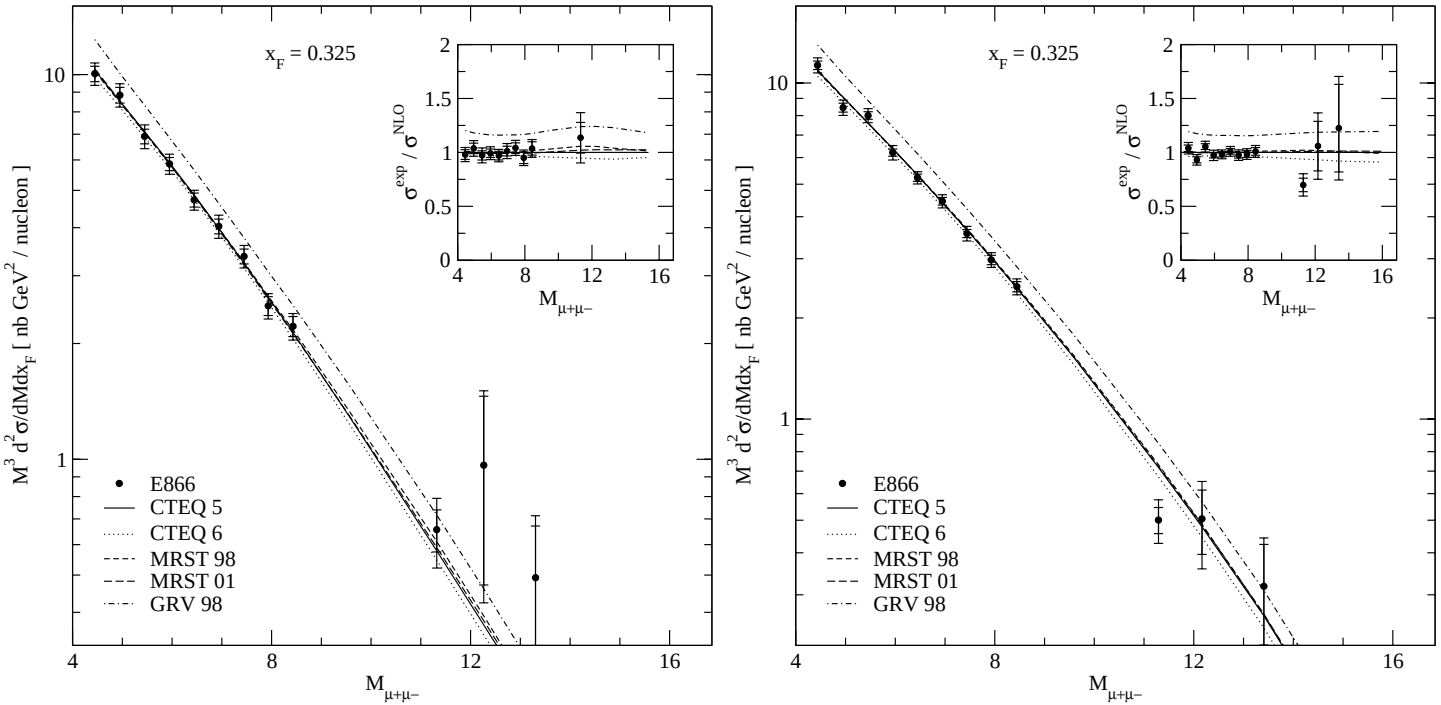

Figure 5.7: Scaling form $M^3 d^2\sigma/dMdx_F$ of the hydrogen (left) and deuterium (right) cross sections for $0.3 \leq x_F < 0.35$. The data are compared to NLO calculations based on several different sets of parton distributions. The inset shows the ratio of the experimentally measured cross sections to NLO calculations based on the CTEQ 5 partons.

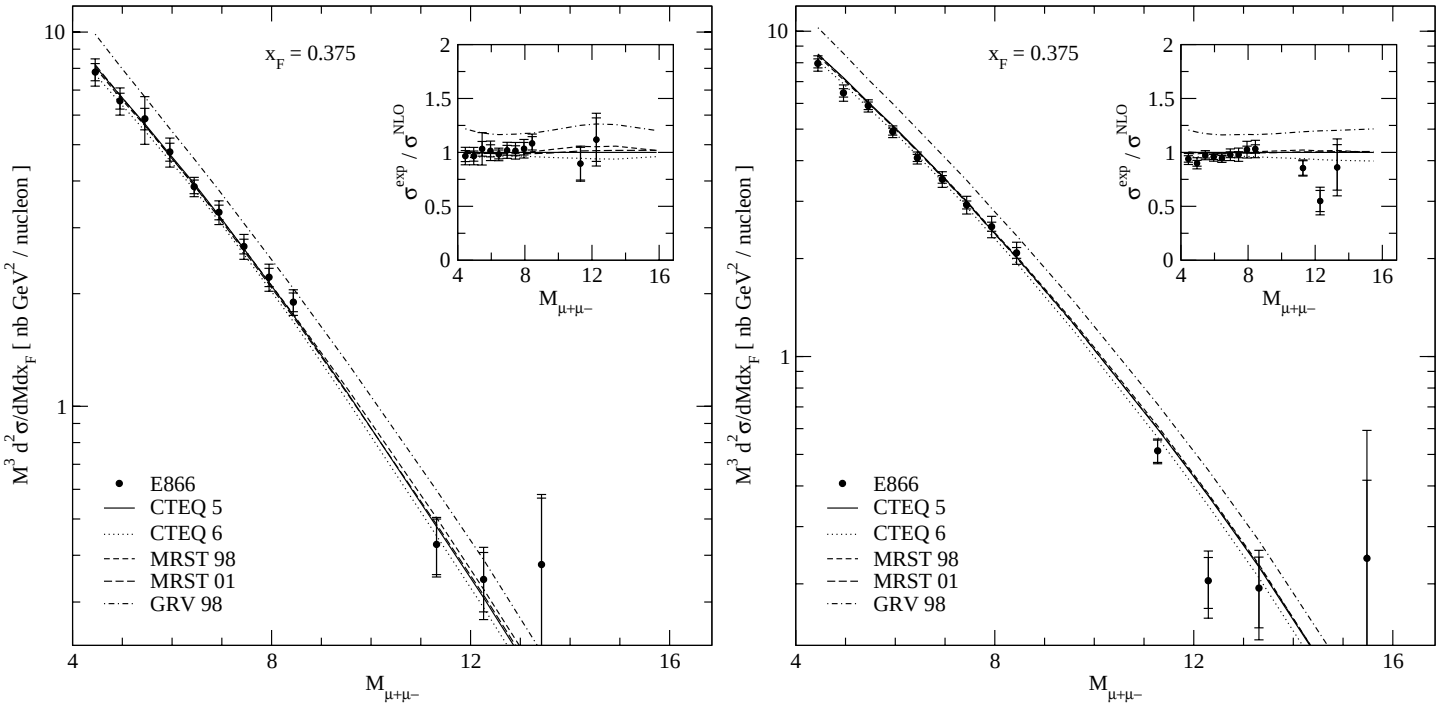

Figure 5.8: Scaling form $M^3 d^2\sigma/dMdx_F$ of the hydrogen (left) and deuterium (right) cross sections for $0.35 \leq x_F < 0.4$. The data are compared to NLO calculations based on several different sets of parton distributions. The inset shows the ratio of the experimentally measured cross sections to NLO calculations based on the CTEQ 5 partons.

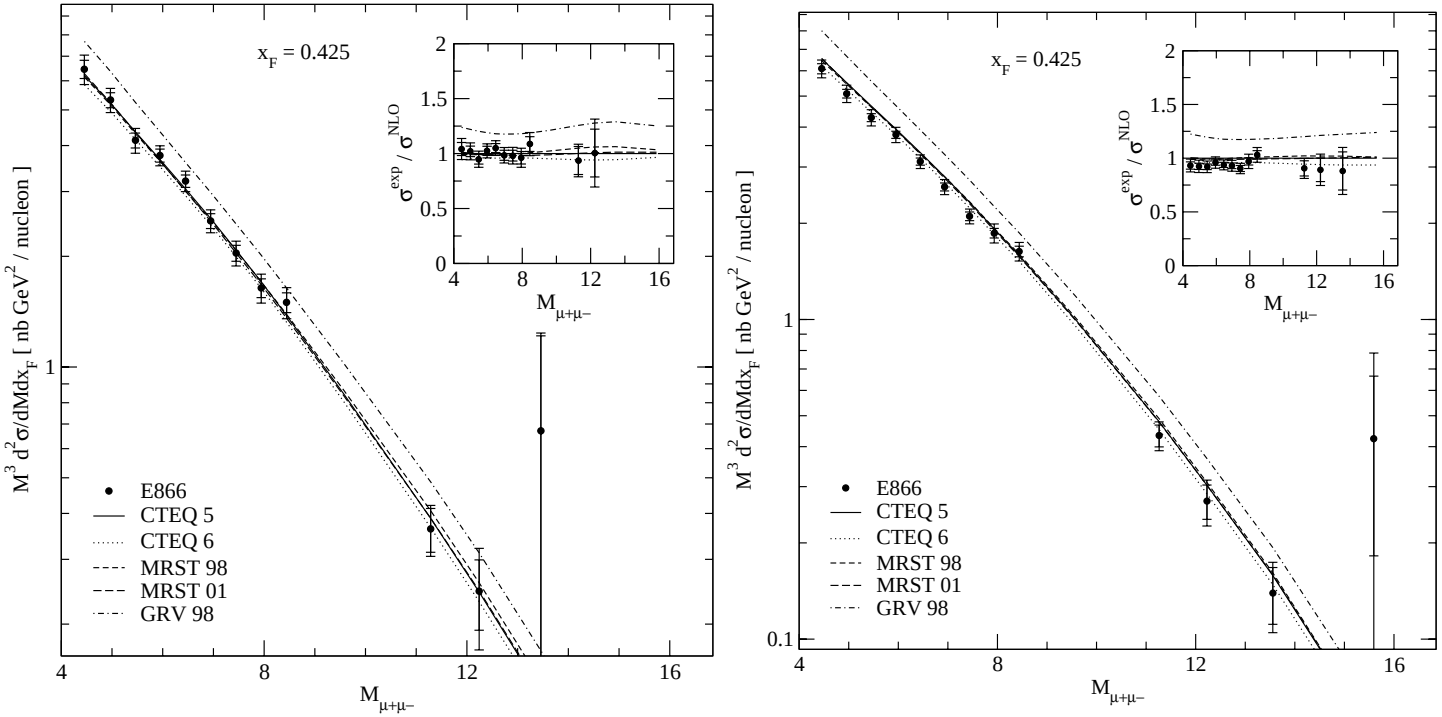

Figure 5.9: Scaling form $M^3 d^2\sigma/dMdx_F$ of the hydrogen (left) and deuterium (right) cross sections for $0.4 \leq x_F < 0.45$. The data are compared to NLO calculations based on several different sets of parton distributions. The inset shows the ratio of the experimentally measured cross sections to NLO calculations based on the CTEQ 5 partons.

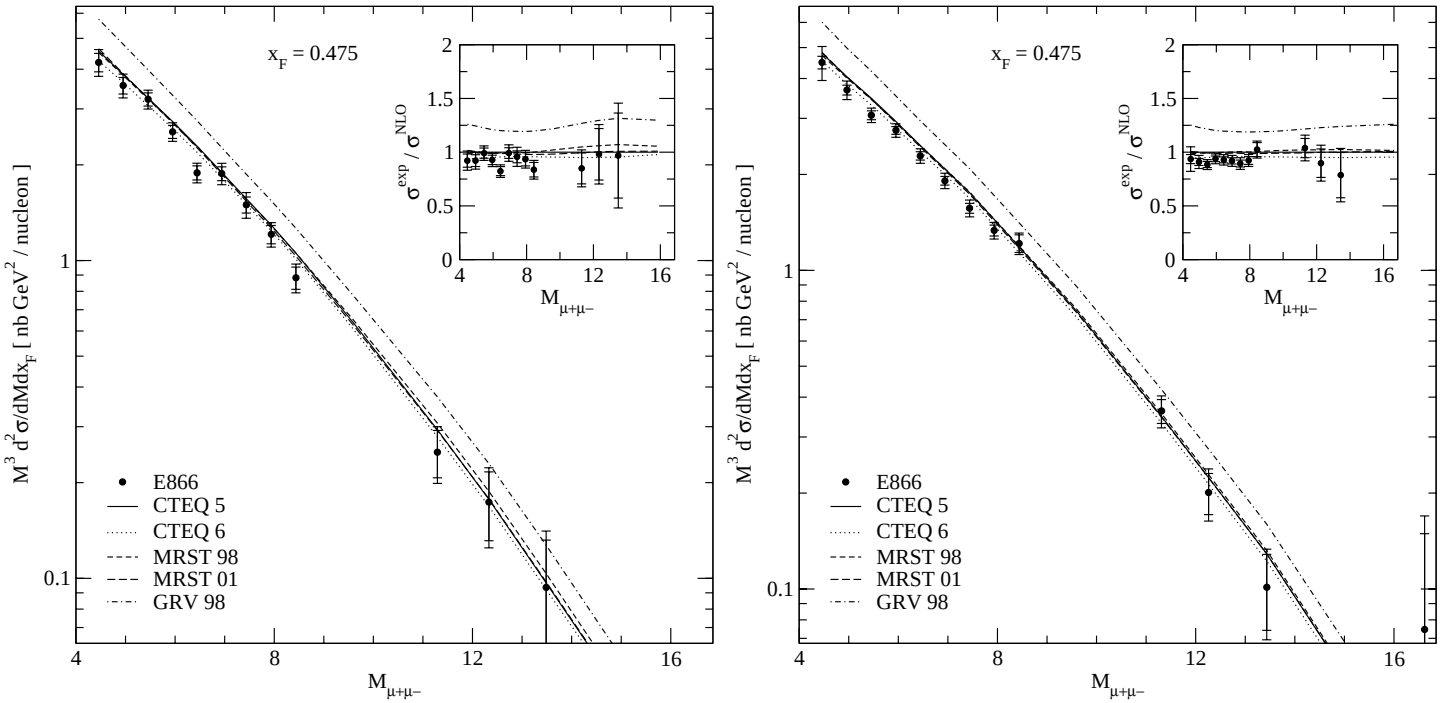

Figure 5.10: Scaling form $M^3 d^2\sigma/dMdx_F$ of the hydrogen (left) and deuterium (right) cross sections for $0.45 \leq x_F < 0.5$. The data are compared to NLO calculations based on several different sets of parton distributions. The inset shows the ratio of the experimentally measured cross sections to NLO calculations based on the CTEQ 5 partons.

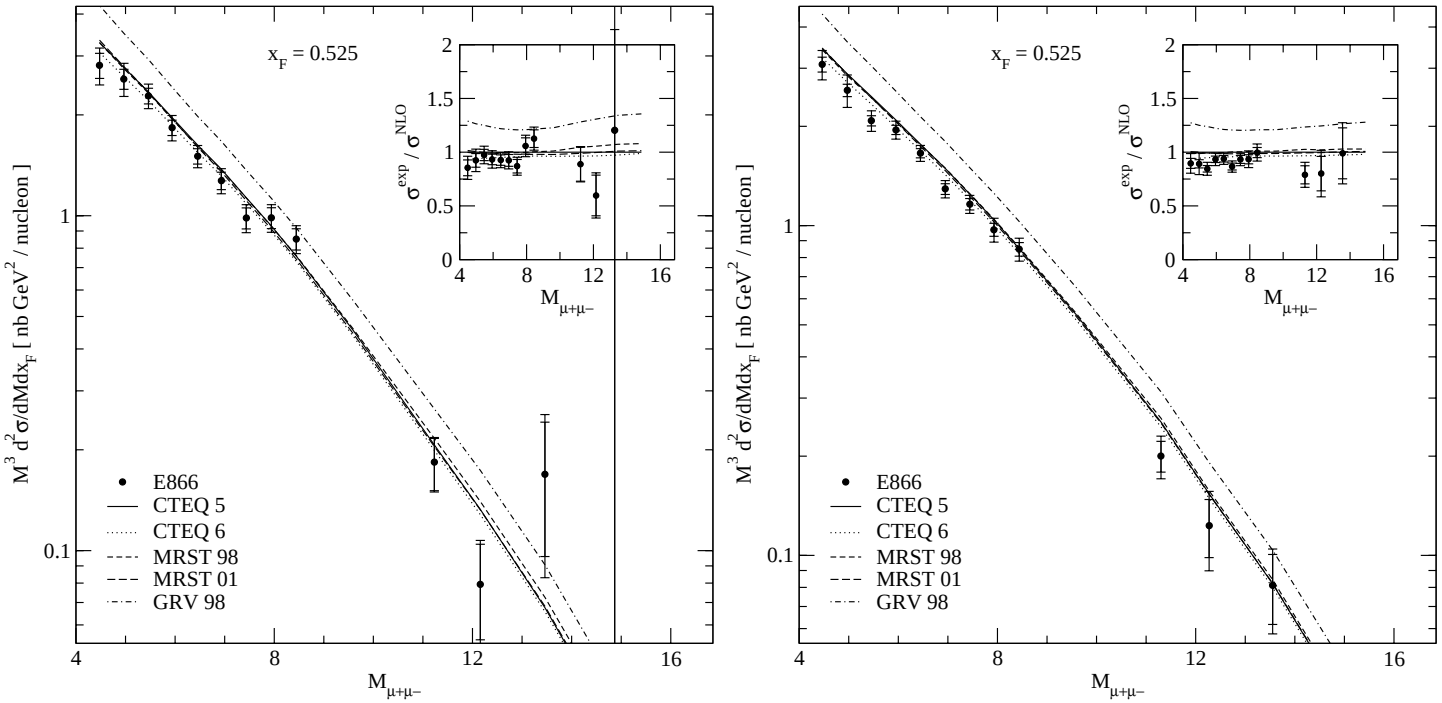

Figure 5.11: Scaling form $M^3 d^2\sigma/dMdx_F$ of the hydrogen (left) and deuterium (right) cross sections for $0.5 \leq x_F < 0.55$. The data are compared to NLO calculations based on several different sets of parton distributions. The inset shows the ratio of the experimentally measured cross sections to NLO calculations based on the CTEQ 5 partons.

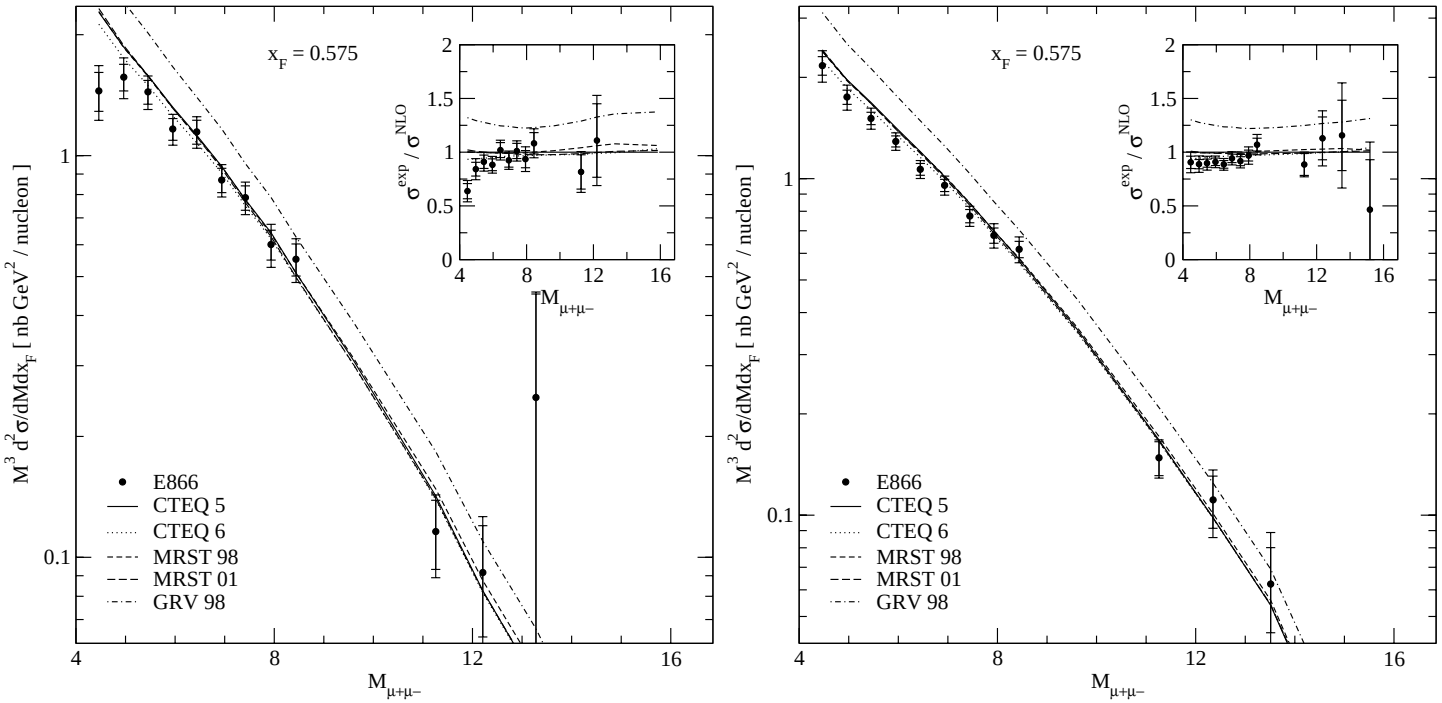

Figure 5.12: Scaling form $M^3 d^2\sigma/dMdx_F$ of the hydrogen (left) and deuterium (right) cross sections for $0.55 \leq x_F < 0.6$. The data are compared to NLO calculations based on several different sets of parton distributions. The inset shows the ratio of the experimentally measured cross sections to NLO calculations based on the CTEQ 5 partons.

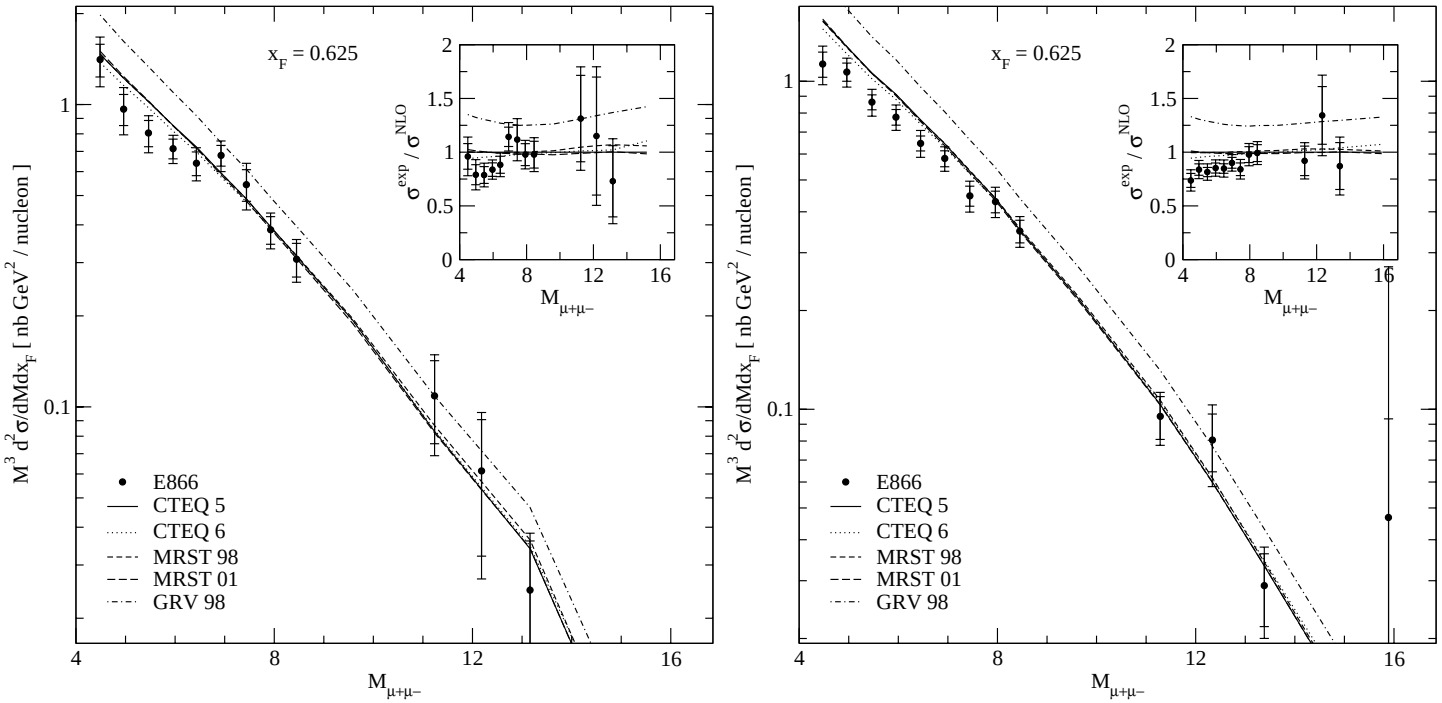

Figure 5.13: Scaling form $M^3 d^2\sigma/dMdx_F$ of the hydrogen (left) and deuterium (right) cross sections for $0.6 \leq x_F < 0.65$. The data are compared to NLO calculations based on several different sets of parton distributions. The inset shows the ratio of the experimentally measured cross sections to NLO calculations based on the CTEQ 5 partons.

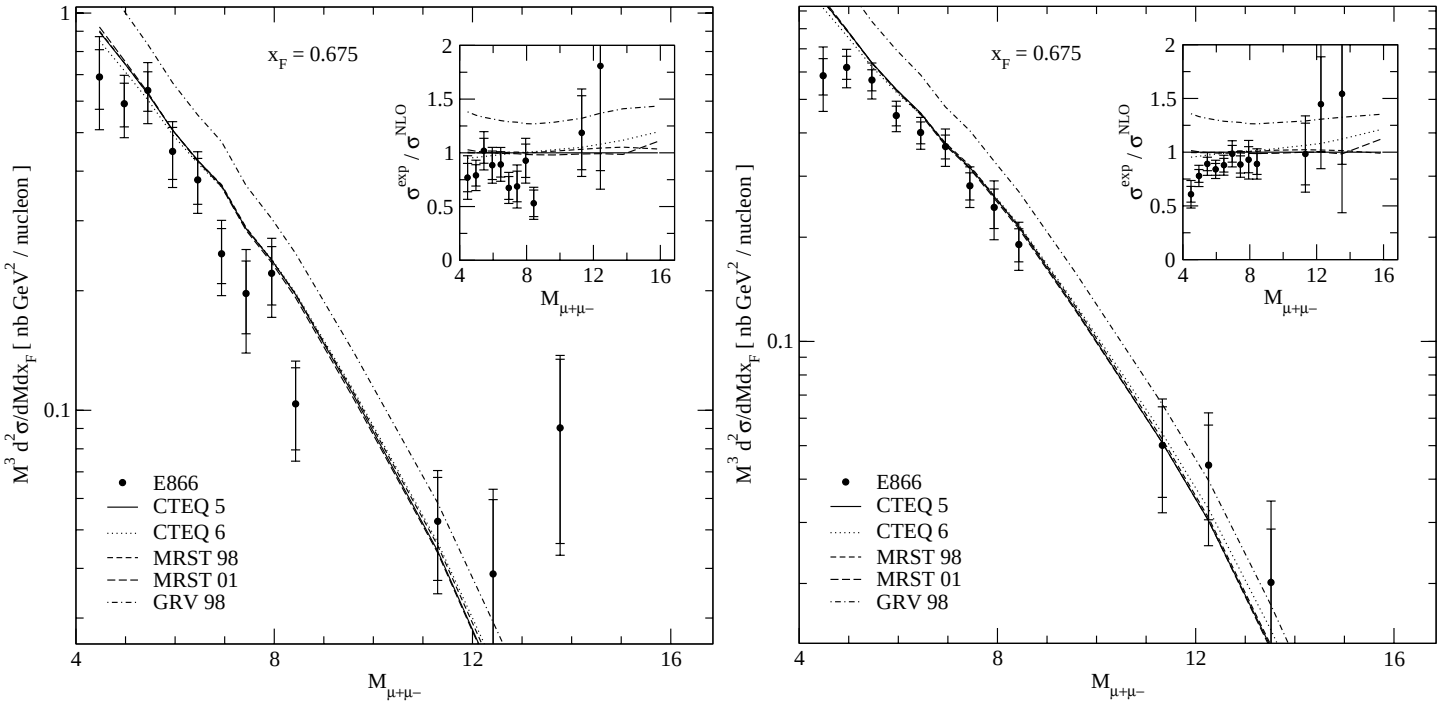

Figure 5.14: Scaling form $M^3 d^2\sigma/dMdx_F$ of the hydrogen (left) and deuterium (right) cross sections for $0.65 \leq x_F < 0.7$. The data are compared to NLO calculations based on several different sets of parton distributions. The inset shows the ratio of the experimentally measured cross sections to NLO calculations based on the CTEQ 5 partons.

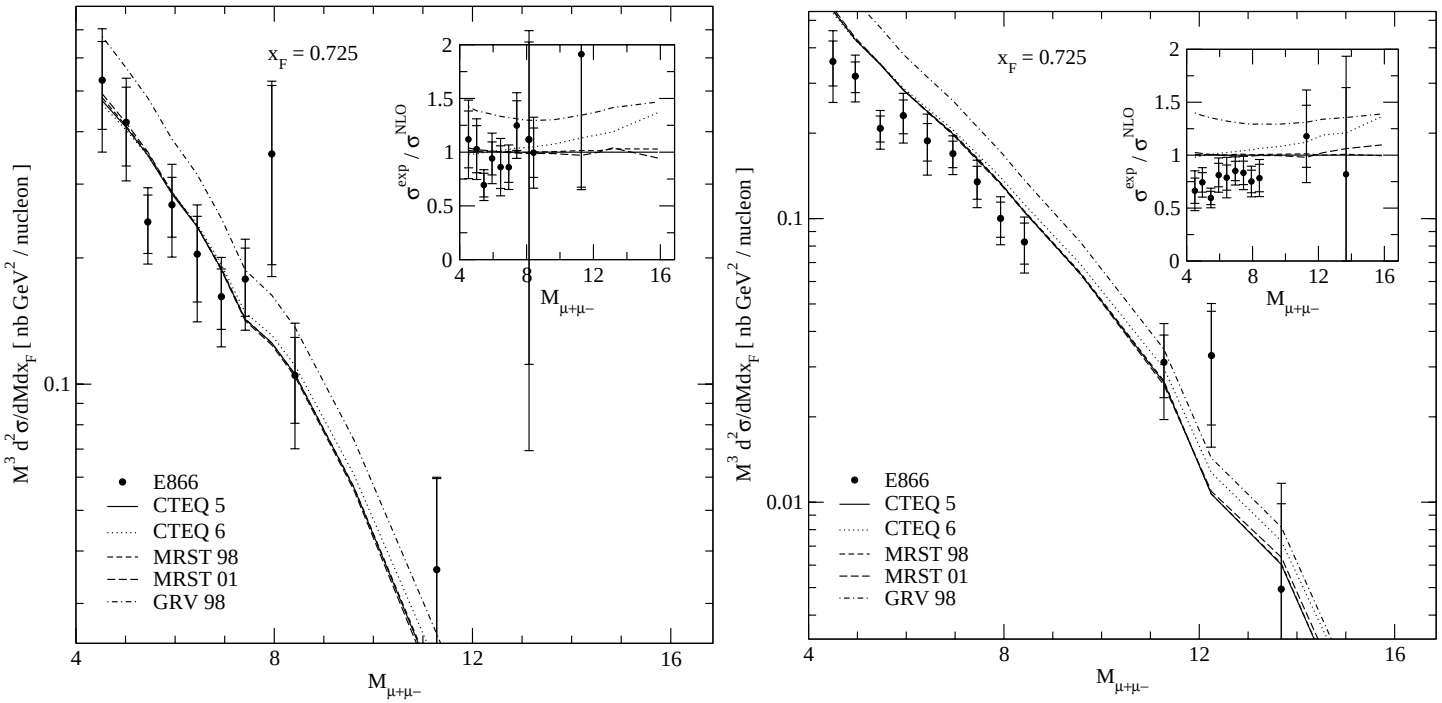

Figure 5.15: Scaling form $M^3 d^2\sigma/dMdx_F$ of the hydrogen (left) and deuterium (right) cross sections for $0.7 \leq x_F < 0.75$. The data are compared to NLO calculations based on several different sets of parton distributions. The inset shows the ratio of the experimentally measured cross sections to NLO calculations based on the CTEQ 5 partons.

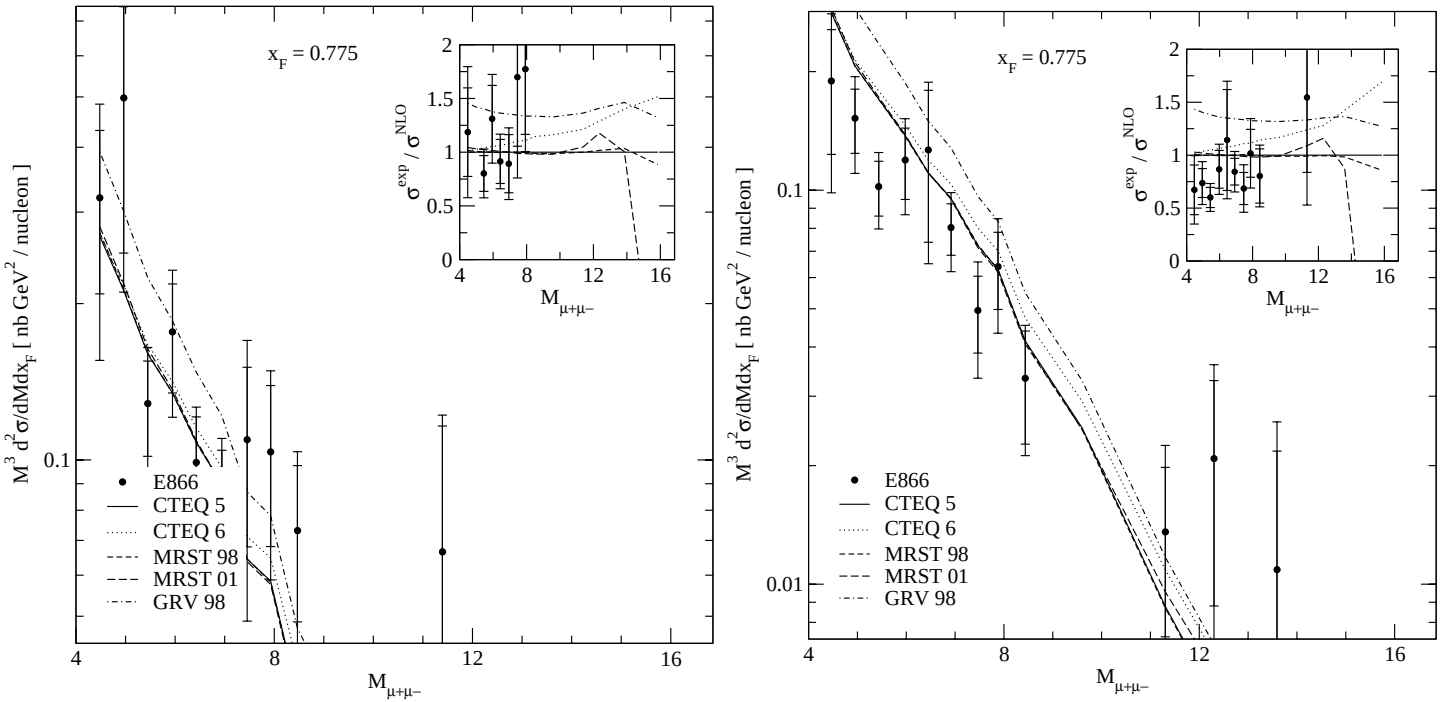

Figure 5.16: Scaling form $M^3 d^2\sigma/dMdx_F$ of the hydrogen (left) and deuterium (right) cross sections for $0.75 \leq x_F < 0.8$. The data are compared to NLO calculations based on several different sets of parton distributions. The inset shows the ratio of the experimentally measured cross sections to NLO calculations based on the CTEQ 5 partons.

5.2 FNAL E866/NuSea Results – $Ed^3\sigma/dp^3$

The p_T-distributions are presented in terms of the invariant cross section

$$E\frac{d^3\sigma}{dp^3} = \frac{2E}{\pi\sqrt{s}}\frac{d^2\sigma}{dx_F dp_T^2} \tag{5.1}$$

where the ϕ dependence has been averaged over. The cross sections are tabulated in tables 5.3 through 5.10, in x_F bins, integrated over the specified range in invariant mass. The mean mass, x_F, p_T and E in each bin are also tabulated.

Table 5.3: Invariant form $Ed^3\sigma/dp^3$ (in units of pb / GeV^2 / nucleon) for the hydrogen cross section for -0.05 $\leq x_F \leq$ 0.15. Statistical and point-to-point systematic uncertainties are shown separately. An additional $\pm$6.5% uncertainty in the normalization is common to all data points.

p_T [GeV]	$< p_T >$	$< M >$	$< x_F >$	$< E >$	$4.20 \leq M_{\mu^+\mu^-} \leq 5.20$	Stat. Error.	Syst. Error
0.00-0.25	0.16	4.64	0.11	6.277	1.33e+01	1.56e+00	8.80e-01
0.25-0.50	0.39	4.66	0.12	6.544	1.21e+01	1.20e+00	3.62e-01
0.50-0.75	0.63	4.65	0.12	6.533	9.72e+00	8.45e-01	2.93e-01
0.75-1.00	0.87	4.64	0.12	6.641	8.85e+00	6.40e-01	2.80e-01
1.00-1.25	1.12	4.61	0.12	6.727	5.70e+00	5.60e-01	1.84e-01
1.25-1.50	1.36	4.64	0.12	6.741	4.86e+00	4.72e-01	1.57e-01
1.50-1.75	1.64	4.61	0.13	6.923	2.01e+00	3.70e-01	8.46e-02
1.75-2.00	1.85	4.58	0.12	6.782	1.67e+00	3.43e-01	7.15e-02
2.00-2.50	2.19	4.54	0.12	6.866	7.72e-01	1.45e-01	3.40e-02
2.50-3.00	2.69	4.77	0.13	7.434	3.06e-01	1.00e-01	1.91e-02
3.00-3.50	3.13	4.75	0.13	7.657	1.22e-01	7.95e-02	1.34e-02
p_T [GeV]	$< p_T >$	$< M >$	$< x_F >$	$< E >$	$5.20 \leq M_{\mu^+\mu^-} \leq 6.20$	Stat. Error.	Syst. Error
0.00-0.25	0.19	5.61	0.13	7.449	1.97e+00	8.11e-01	2.00e-01
0.25-0.50	0.39	5.67	0.12	7.305	4.75e+00	6.04e-01	1.80e-01
0.50-0.75	0.62	5.56	0.12	7.221	4.72e+00	4.68e-01	1.74e-01
0.75-1.00	0.88	5.65	0.12	7.475	2.88e+00	3.85e-01	1.11e-01
1.00-1.25	1.12	5.66	0.12	7.496	2.84e+00	3.24e-01	1.10e-01
1.25-1.50	1.35	5.61	0.13	7.566	1.01e+00	2.40e-01	7.08e-02
1.50-1.75	1.60	5.70	0.12	7.498	1.05e+00	2.01e-01	8.97e-02
1.75-2.00	1.86	5.66	0.12	7.577	8.38e-01	1.92e-01	7.77e-02

Table 5.3: continued

2.00-2.50	2.16	5.67	0.11	7.518	1.73e-01	6.68e-02	2.25e-02
2.50-3.00	2.76	5.68	0.11	7.656	2.45e-01	8.65e-02	2.72e-02
3.00-3.50	3.28	5.79	0.12	8.119	5.91e-02	4.21e-02	1.32e-02
p_T [GeV]	$< p_T >$	$< M >$	$< x_F >$	$< E >$	$6.20 \leq M_{\mu^+\mu^-} \leq 7.20$	Stat. Error.	Syst. Error
0.00-0.25	0.16	6.66	0.10	7.877	1.58e+00	3.93e-01	1.59e-01
0.25-0.50	0.38	6.67	0.09	7.804	1.52e+00	3.17e-01	8.64e-02
0.50-0.75	0.62	6.69	0.10	7.865	1.42e+00	2.43e-01	9.54e-02
0.75-1.00	0.88	6.70	0.10	7.982	1.11e+00	1.60e-01	7.37e-02
1.00-1.25	1.10	6.75	0.11	8.178	8.44e-01	1.63e-01	9.10e-02
1.25-1.50	1.36	6.66	0.12	8.212	3.80e-01	1.38e-01	6.89e-02
1.50-1.75	1.62	6.75	0.11	8.266	2.92e-01	1.16e-01	5.42e-02
1.75-2.00	1.84	6.80	0.10	8.086	1.32e-01	5.25e-02	1.00e-02
2.00-2.50	2.16	6.56	0.12	8.390	1.22e-01	6.79e-02	2.00e-02
2.50-3.00	2.56	6.47	0.12	8.333	5.16e-02	3.09e-02	1.01e-02
p_T [GeV]	$< p_T >$	$< M >$	$< x_F >$	$< E >$	$7.20 \leq M_{\mu^+\mu^-} \leq 8.70$	Stat. Error.	Syst. Error
0.00-0.25	0.16	8.14	0.09	8.988	8.26e-01	1.35e-01	5.02e-02
0.25-0.50	0.39	8.09	0.09	9.029	1.08e+00	9.70e-02	3.41e-02
0.50-0.75	0.63	8.05	0.09	8.982	7.51e-01	6.72e-02	3.68e-02
0.75-1.00	0.87	8.06	0.10	9.072	7.33e-01	5.25e-02	2.39e-02
1.00-1.25	1.12	8.02	0.10	9.102	5.26e-01	4.69e-02	2.08e-02
1.25-1.50	1.36	8.05	0.10	9.179	3.09e-01	3.35e-02	1.27e-02
1.50-1.75	1.61	8.10	0.10	9.265	2.39e-01	2.96e-02	1.03e-02
1.75-2.00	1.86	8.05	0.11	9.386	1.50e-01	2.55e-02	7.80e-03
2.00-2.50	2.17	8.05	0.11	9.397	5.58e-02	1.15e-02	2.08e-03
2.50-3.00	2.66	8.10	0.11	9.569	3.27e-02	8.53e-03	2.38e-03
3.00-3.50	3.26	7.98	0.10	9.524	1.22e-02	4.51e-03	1.88e-03

Table 5.3: continued

3.50-4.00	3.78	7.89	0.11	9.762	1.88e-02	9.54e-03	3.18e-03
p_T [GeV]	$< p_T >$	$< M >$	$< x_F >$	$< E >$	$10.85 \leq M_{\mu^+\mu^-} \leq 12.85$	Stat. Error.	Syst. Error
0.25-0.50	0.40	11.25	0.08	11.627	6.61e-02	6.61e-02	1.55e-02
0.50-0.75	0.64	11.35	0.13	12.525	7.12e-02	3.07e-02	2.13e-02
0.75-1.00	0.89	11.28	0.10	11.989	6.28e-02	3.63e-02	1.21e-02
1.00-1.25	1.16	11.04	0.11	11.870	4.23e-02	1.97e-02	4.45e-03
1.25-1.50	1.37	10.98	0.11	11.866	2.99e-02	1.50e-02	4.27e-03
1.50-1.75	1.59	11.23	0.13	12.355	3.57e-02	2.52e-02	6.28e-03
1.75-2.00	1.89	11.25	0.10	12.048	9.40e-02	4.70e-02	1.96e-02

Table 5.4: Invariant form $Ed^3\sigma/dp^3$ (in units of pb / GeV^2 / nucleon) for the hydrogen cross section for $0.15 \leq x_F \leq 0.35$. Statistical and point-to-point systematic uncertainties are shown. An additional $\pm 6.5\%$ uncertainty in the normalization is common to all data points.

p_T [GeV]	$< p_T >$	$< M >$	$< x_F >$	$< E >$	$4.20 \leq M_{\mu^+\mu^-} \leq 5.20$	Stat. Error.	Syst. Error
0.00-0.25	0.17	4.67	0.25	10.767	1.15e+01	7.46e-01	4.71e-01
0.25-0.50	0.39	4.66	0.25	10.840	1.31e+01	5.19e-01	3.94e-01
0.50-0.75	0.63	4.66	0.25	10.848	1.16e+01	3.96e-01	3.20e-01
0.75-1.00	0.87	4.66	0.25	10.880	8.05e+00	2.91e-01	2.22e-01
1.00-1.25	1.12	4.66	0.25	10.807	5.99e+00	2.21e-01	1.70e-01
1.25-1.50	1.37	4.67	0.25	10.902	3.87e+00	1.82e-01	1.15e-01
1.50-1.75	1.61	4.65	0.25	10.877	2.54e+00	1.39e-01	6.89e-02
1.75-2.00	1.87	4.68	0.25	11.050	1.49e+00	1.06e-01	5.25e-02
2.00-2.50	2.21	4.63	0.26	11.252	6.55e-01	5.78e-02	2.25e-02

Table 5.4: continued

2.50-3.00	2.72	4.62	0.26	11.532	3.01e-01	3.44e-02	2.07e-02
3.00-3.50	3.21	4.69	0.26	11.599	1.07e-01	3.09e-02	1.33e-02
3.50-4.00	3.72	4.65	0.27	12.160	5.40e-02	2.34e-02	1.28e-02
4.00-5.00	4.32	4.71	0.28	12.512	3.92e-02	1.39e-02	5.32e-03
p_T [GeV]	$< p_T >$	$< M >$	$< x_F >$	$< E >$	$5.20 \leq M_{\mu^+\mu^-} \leq 6.20$	Stat. Error.	Syst. Error
0.00-0.25	0.16	5.69	0.27	12.024	4.26e+00	3.56e-01	1.85e-01
0.25-0.50	0.39	5.68	0.27	12.053	5.55e+00	2.39e-01	1.86e-01
0.50-0.75	0.63	5.69	0.27	12.023	4.32e+00	1.68e-01	1.37e-01
0.75-1.00	0.87	5.69	0.27	11.996	3.25e+00	1.32e-01	9.49e-02
1.00-1.25	1.12	5.69	0.27	12.090	2.34e+00	1.03e-01	6.63e-02
1.25-1.50	1.37	5.70	0.27	12.065	1.59e+00	8.55e-02	4.59e-02
1.50-1.75	1.62	5.70	0.27	12.115	1.11e+00	6.37e-02	3.29e-02
1.75-2.00	1.87	5.71	0.28	12.359	6.55e-01	5.27e-02	2.15e-02
2.00-2.50	2.21	5.63	0.27	12.071	3.15e-01	2.56e-02	1.09e-02
2.50-3.00	2.69	5.70	0.27	12.127	9.87e-02	1.65e-02	4.90e-03
3.00-3.50	3.24	5.75	0.28	12.880	3.94e-02	9.16e-03	6.33e-03
3.50-4.00	3.71	5.66	0.28	12.947	2.74e-02	8.02e-03	6.96e-03
4.00-5.00	4.35	5.84	0.27	12.853	2.06e-02	6.10e-03	4.55e-03
p_T [GeV]	$< p_T >$	$< M >$	$< x_F >$	$< E >$	$6.20 \leq M_{\mu^+\mu^-} \leq 7.20$	Stat. Error.	Syst. Error
0.00-0.25	0.16	6.69	0.27	12.511	1.81e+00	1.44e-01	1.22e-01
0.25-0.50	0.38	6.67	0.27	12.631	2.33e+00	1.05e-01	9.07e-02
0.50-0.75	0.63	6.69	0.27	12.488	1.82e+00	7.45e-02	7.60e-02
0.75-1.00	0.88	6.68	0.27	12.638	1.41e+00	5.89e-02	6.05e-02
1.00-1.25	1.12	6.70	0.27	12.618	1.02e+00	4.52e-02	3.56e-02
1.25-1.50	1.36	6.70	0.27	12.667	6.21e-01	3.53e-02	1.81e-02
1.50-1.75	1.61	6.73	0.27	12.751	4.55e-01	2.84e-02	1.88e-02

Table 5.4: continued

1.75-2.00	1.86	6.71	0.27	12.678	2.56e-01	2.12e-02	1.34e-02
2.00-2.50	2.21	6.72	0.28	12.922	1.26e-01	1.02e-02	4.00e-03
2.50-3.00	2.69	6.78	0.27	12.943	4.26e-02	5.60e-03	2.05e-03
3.00-3.50	3.25	6.71	0.29	13.499	2.09e-02	3.86e-03	1.38e-03
3.50-4.00	3.71	6.74	0.25	12.325	9.14e-03	2.80e-03	8.29e-04
4.00-5.00	4.40	6.91	0.26	13.002	5.71e-03	2.03e-03	1.02e-03
5.00-6.00	5.74	6.82	0.32	15.200	2.79e-03	2.79e-03	1.59e-03
p_T [GeV]	$< p_T >$	$< M >$	$< x_F >$	$< E >$	$7.20 \leq M_{\mu^+\mu^-} \leq 8.70$	Stat. Error.	Syst. Error
0.00-0.25	0.17	7.87	0.26	12.844	8.59e-01	7.78e-02	3.89e-02
0.25-0.50	0.39	7.87	0.26	12.854	1.22e+00	5.56e-02	3.62e-02
0.50-0.75	0.63	7.86	0.26	12.931	9.48e-01	4.04e-02	2.73e-02
0.75-1.00	0.87	7.87	0.26	12.878	7.37e-01	3.02e-02	3.04e-02
1.00-1.25	1.12	7.88	0.26	12.846	5.22e-01	2.29e-02	1.94e-02
1.25-1.50	1.37	7.88	0.26	12.835	3.86e-01	1.79e-02	1.07e-02
1.50-1.75	1.62	7.91	0.26	12.933	2.35e-01	1.34e-02	7.07e-03
1.75-2.00	1.86	7.92	0.26	13.026	1.61e-01	1.05e-02	4.82e-03
2.00-2.50	2.21	7.93	0.26	13.090	8.23e-02	5.21e-03	3.49e-03
2.50-3.00	2.71	7.95	0.26	13.225	3.39e-02	3.25e-03	2.56e-03
3.00-3.50	3.23	8.04	0.27	13.744	1.33e-02	1.98e-03	1.08e-03
3.50-4.00	3.69	7.95	0.28	14.005	5.60e-03	1.57e-03	5.36e-04
4.00-5.00	4.43	7.79	0.28	14.172	5.35e-04	3.54e-04	1.30e-04
5.00-6.00	5.27	8.18	0.26	14.262	1.22e-03	7.15e-04	2.92e-04
p_T [GeV]	$< p_T >$	$< M >$	$< x_F >$	$< E >$	$10.85 \leq M_{\mu^+\mu^-} \leq 12.85$	Stat. Error.	Syst. Error
0.00-0.25	0.17	11.35	0.28	15.856	5.19e-02	1.79e-02	6.69e-03
0.25-0.50	0.36	11.55	0.28	15.850	8.50e-02	1.90e-02	3.76e-03
0.50-0.75	0.65	11.47	0.28	15.745	6.75e-02	1.37e-02	5.43e-03

Table 5.4: continued

0.75-1.00	0.86	11.52	0.27	15.750	4.67e-02	9.80e-03	3.43e-03
1.00-1.25	1.11	11.43	0.28	15.749	5.49e-02	8.02e-03	3.49e-03
1.25-1.50	1.36	11.53	0.26	15.492	3.29e-02	5.92e-03	3.02e-03
1.50-1.75	1.62	11.48	0.28	15.898	2.97e-02	6.12e-03	4.83e-03
1.75-2.00	1.86	11.45	0.28	16.073	9.18e-03	3.09e-03	2.44e-03
2.00-2.50	2.17	11.39	0.26	15.376	6.91e-03	1.44e-03	1.12e-03
2.50-3.00	2.75	11.35	0.29	16.260	4.82e-03	1.21e-03	1.22e-03
3.00-3.50	3.24	11.60	0.29	16.438	2.84e-03	1.08e-03	5.82e-04
p_T [GeV]	$< p_T >$	$< M >$	$< x_F >$	$< E >$	$12.85 \leq M_{\mu^+\mu^-} \leq 16.85$	Stat. Error.	Syst. Error
0.00-0.25	0.22	13.08	0.22	15.641	4.16e-02	3.71e-02	1.57e-02
0.25-0.50	0.41	13.47	0.26	16.864	4.77e-02	3.37e-02	8.62e-03
0.50-0.75	0.67	13.40	0.27	17.111	4.03e-02	4.03e-02	8.31e-03
0.75-1.00	0.93	13.09	0.29	17.194	1.67e-02	1.10e-02	1.52e-03
1.00-1.25	1.09	13.18	0.24	16.172	2.02e-02	1.23e-02	2.20e-03
1.25-1.50	1.35	14.11	0.31	18.589	2.47e-02	1.44e-02	3.57e-03
1.50-1.75	1.61	13.38	0.32	18.430	2.77e-02	1.96e-02	4.81e-03
2.00-2.50	2.29	13.53	0.25	16.762	5.19e-03	3.67e-03	8.84e-04
2.50-3.00	2.79	13.05	0.25	16.712	5.77e-03	4.09e-03	1.33e-03

Table 5.5: Invariant form $Ed^3\sigma/dp^3$ (in units of pb / GeV^2 / nucleon) for the hydrogen cross section for $0.35 \leq x_F \leq 0.55$. Statistical and point-to-point systematic uncertainties are shown. An additional $\pm 6.5\%$ uncertainty in the normalization is common to all data points.

p_T [GeV]	$< p_T >$	$< M >$	$< x_F >$	$< E >$	$4.20 \leq M_{\mu^+\mu^-} \leq 5.20$	Stat. Error.	Syst. Error

Table 5.5: continued

0.00-0.25	0.17	4.72	0.43	17.356	7.12e+00	6.41e-01	5.75e-01
0.25-0.50	0.39	4.73	0.43	17.272	9.00e+00	4.58e-01	3.12e-01
0.50-0.75	0.63	4.71	0.43	17.439	7.93e+00	3.27e-01	2.30e-01
0.75-1.00	0.87	4.74	0.43	17.357	5.28e+00	2.47e-01	1.94e-01
1.00-1.25	1.12	4.74	0.43	17.360	3.76e+00	1.82e-01	1.70e-01
1.25-1.50	1.37	4.74	0.43	17.470	2.34e+00	1.42e-01	1.16e-01
1.50-1.75	1.61	4.74	0.43	17.542	1.25e+00	1.08e-01	4.09e-02
1.75-2.00	1.86	4.74	0.43	17.555	7.64e-01	7.55e-02	2.69e-02
2.00-2.50	2.20	4.75	0.43	17.313	3.03e-01	3.40e-02	1.14e-02
2.50-3.00	2.71	4.70	0.42	17.237	9.48e-02	2.02e-02	4.83e-03
3.00-3.50	3.23	4.75	0.42	17.204	4.71e-02	1.14e-02	3.79e-03
3.50-4.00	3.73	4.73	0.41	17.056	3.28e-02	1.01e-02	7.09e-03
4.00-5.00	4.32	4.81	0.44	18.352	1.12e-02	4.90e-03	1.85e-02
5.00-6.00	5.11	4.74	0.37	15.808	4.89e-03	4.89e-03	9.98e-03
p_T [GeV]	$< p_T >$	$< M >$	$< x_F >$	$< E >$	$5.20 \leq M_{\mu^+\mu^-} \leq 6.20$	Stat. Error.	Syst. Error
0.00-0.25	0.16	5.71	0.44	18.031	3.65e+00	2.17e-01	1.27e-01
0.25-0.50	0.39	5.72	0.44	17.976	3.56e+00	1.36e-01	1.22e-01
0.50-0.75	0.63	5.72	0.43	17.825	3.06e+00	1.07e-01	9.12e-02
0.75-1.00	0.87	5.71	0.44	17.900	2.02e+00	7.66e-02	6.00e-02
1.00-1.25	1.12	5.71	0.44	18.059	1.43e+00	5.79e-02	3.89e-02
1.25-1.50	1.37	5.73	0.44	17.975	9.52e-01	4.57e-02	2.72e-02
1.50-1.75	1.62	5.72	0.44	17.940	5.82e-01	3.53e-02	1.74e-02
1.75-2.00	1.87	5.71	0.44	18.033	3.54e-01	2.64e-02	1.13e-02
2.00-2.50	2.22	5.71	0.44	17.961	1.42e-01	1.29e-02	5.06e-03
2.50-3.00	2.68	5.65	0.43	17.837	5.01e-02	7.23e-03	2.59e-03
3.00-3.50	3.26	5.71	0.43	18.108	1.65e-02	4.88e-03	1.48e-03

Table 5.5: continued

3.50-4.00	3.73	5.64	0.43	17.960	7.44e-03	2.65e-03	2.12e-03
4.00-5.00	4.41	5.74	0.48	19.844	2.03e-03	9.28e-04	7.55e-04
5.00-6.00	5.44	5.59	0.38	16.530	3.53e-03	2.50e-03	2.75e-03
6.00-7.00	6.82	6.08	0.53	22.453	4.82e-04	4.82e-04	9.83e-04
p_T [GeV]	$< p_T >$	$< M >$	$< x_F >$	$< E >$	$6.20 \leq M_{\mu^+\mu^-} \leq 7.20$	Stat. Error.	Syst. Error
0.00-0.25	0.17	6.63	0.44	18.205	1.25e+00	8.81e-02	4.28e-02
0.25-0.50	0.38	6.67	0.44	18.246	1.41e+00	6.54e-02	4.28e-02
0.50-0.75	0.63	6.67	0.43	18.145	1.19e+00	4.62e-02	3.33e-02
0.75-1.00	0.87	6.66	0.44	18.319	8.88e-01	3.66e-02	2.41e-02
1.00-1.25	1.12	6.68	0.44	18.231	6.87e-01	2.71e-02	1.87e-02
1.25-1.50	1.37	6.69	0.44	18.247	4.30e-01	2.10e-02	1.20e-02
1.50-1.75	1.62	6.70	0.43	18.140	2.45e-01	1.56e-02	7.90e-03
1.75-2.00	1.86	6.70	0.44	18.376	1.59e-01	1.21e-02	5.80e-03
2.00-2.50	2.20	6.71	0.43	18.284	7.74e-02	5.60e-03	2.67e-03
2.50-3.00	2.70	6.71	0.43	18.307	2.80e-02	3.09e-03	1.54e-03
3.00-3.50	3.21	6.72	0.45	18.919	7.96e-03	1.93e-03	5.68e-04
3.50-4.00	3.67	6.64	0.43	18.472	4.06e-03	1.16e-03	5.21e-04
4.00-5.00	4.49	6.74	0.44	18.966	2.23e-03	6.52e-04	4.63e-04
5.00-6.00	5.23	6.71	0.46	19.640	4.46e-04	4.46e-04	2.20e-04
p_T [GeV]	$< p_T >$	$< M >$	$< x_F >$	$< E >$	$7.20 \leq M_{\mu^+\mu^-} \leq 8.70$	Stat. Error.	Syst. Error
0.00-0.25	0.16	7.80	0.44	18.755	6.65e-01	5.96e-02	4.80e-02
0.25-0.50	0.39	7.84	0.44	18.642	8.30e-01	4.19e-02	2.80e-02
0.50-0.75	0.63	7.82	0.44	18.725	6.88e-01	2.99e-02	2.27e-02
0.75-1.00	0.87	7.86	0.44	18.712	5.48e-01	2.25e-02	1.50e-02
1.00-1.25	1.12	7.87	0.44	18.827	3.60e-01	1.73e-02	9.79e-03
1.25-1.50	1.37	7.88	0.44	18.856	2.59e-01	1.30e-02	7.09e-03

Table 5.5: continued

1.50-1.75	1.61	7.85	0.43	18.694	1.59e-01	9.36e-03	4.49e-03
1.75-2.00	1.87	7.94	0.43	18.630	1.05e-01	7.17e-03	3.19e-03
2.00-2.50	2.21	7.89	0.44	18.858	5.49e-02	3.57e-03	1.65e-03
2.50-3.00	2.70	7.95	0.43	18.752	1.66e-02	1.83e-03	5.96e-04
3.00-3.50	3.21	7.79	0.42	18.363	5.26e-03	1.10e-03	3.61e-04
3.50-4.00	3.70	7.71	0.44	19.029	2.20e-03	5.98e-04	2.31e-04
4.00-5.00	4.26	7.76	0.42	18.531	7.84e-04	3.14e-04	1.22e-04
5.00-6.00	5.51	7.29	0.41	18.390	1.45e-04	1.45e-04	9.02e-05
p_T [GeV]	$< p_T >$	$< M >$	$< x_F >$	$< E >$	$10.85 \leq M_{\mu^+\mu^-} \leq 12.85$	Stat. Error.	Syst. Error
0.00-0.25	0.18	11.71	0.42	20.021	2.17e-02	1.73e-02	2.43e-03
0.25-0.50	0.38	11.56	0.44	20.773	5.98e-02	1.08e-02	4.66e-03
0.50-0.75	0.63	11.56	0.43	20.459	4.32e-02	7.20e-03	3.31e-03
0.75-1.00	0.87	11.52	0.44	20.784	4.28e-02	6.62e-03	3.99e-03
1.00-1.25	1.12	11.43	0.43	20.407	2.58e-02	4.00e-03	1.22e-03
1.25-1.50	1.37	11.44	0.44	20.586	1.94e-02	3.39e-03	9.90e-04
1.50-1.75	1.62	11.49	0.45	20.970	6.01e-03	2.93e-03	4.91e-04
1.75-2.00	1.87	11.58	0.44	20.665	1.14e-02	2.54e-03	9.49e-04
2.00-2.50	2.21	11.57	0.43	20.299	4.87e-03	8.33e-04	3.53e-04
2.50-3.00	2.68	11.54	0.45	21.151	1.90e-03	4.60e-04	1.10e-04
3.00-3.50	3.18	11.33	0.47	21.718	5.87e-04	3.70e-04	5.84e-05
3.50-4.00	3.65	11.49	0.41	19.832	4.52e-04	3.39e-04	6.75e-05
4.00-5.00	4.67	11.81	0.41	20.319	1.10e-04	1.10e-04	3.26e-05
5.00-6.00	5.64	11.40	0.41	20.415	5.57e-05	5.57e-05	1.13e-04
p_T [GeV]	$< p_T >$	$< M >$	$< x_F >$	$< E >$	$12.85 \leq M_{\mu^+\mu^-} \leq 16.85$	Stat. Error.	Syst. Error
0.00-0.25	0.06	13.22	0.49	23.133	5.19e-02	5.19e-02	9.21e-03
0.25-0.50	0.41	13.25	0.51	23.884	7.28e-02	5.15e-02	8.29e-03

Table 5.5: continued

0.50-0.75	0.67	13.37	0.42	21.241	1.61e-02	5.47e-03	9.73e-04
0.75-1.00	0.84	13.68	0.48	23.158	1.09e-02	4.43e-03	6.29e-04
1.00-1.25	1.08	13.51	0.48	23.098	9.68e-03	4.26e-03	6.40e-04
1.25-1.50	1.40	14.02	0.45	22.405	4.22e-03	2.15e-03	2.87e-04
1.50-1.75	1.64	13.39	0.43	21.321	5.02e-03	2.31e-03	3.69e-04
1.75-2.00	1.95	13.36	0.48	23.111	1.61e-02	1.14e-02	1.96e-03
2.00-2.50	2.09	13.24	0.40	20.624	6.51e-03	4.61e-03	9.44e-04
2.50-3.00	2.77	13.56	0.52	24.424	1.53e-03	1.53e-03	3.07e-04
3.00-3.50	3.17	13.43	0.42	21.367	5.40e-03	5.40e-03	3.18e-03

Table 5.6: Invariant form $Ed^3\sigma/dp^3$ (in units of pb / GeV^2 / nucleon) for the hydrogen cross section for $0.55 \leq x_F \leq 0.8$. Statistical and point-to-point systematic uncertainties are shown. An additional $\pm 6.5\%$ uncertainty in the normalization is common to all data points.

p_T [GeV]	$< p_T >$	$< M >$	$< x_F >$	$< E >$	$4.20 \leq M_{\mu^+\mu^-} \leq 5.20$	Stat. Error.	Syst. Error
0.00-0.25	0.17	4.87	0.62	24.586	1.86e+00	3.00e-01	2.19e-01
0.25-0.50	0.39	4.78	0.63	24.948	2.61e+00	2.48e-01	1.54e-01
0.50-0.75	0.63	4.80	0.62	24.641	1.71e+00	1.59e-01	8.19e-02
0.75-1.00	0.87	4.79	0.63	24.800	1.35e+00	1.18e-01	5.93e-02
1.00-1.25	1.12	4.78	0.61	24.314	9.03e-01	8.65e-02	3.87e-02
1.25-1.50	1.36	4.77	0.62	24.673	4.90e-01	6.05e-02	2.06e-02
1.50-1.75	1.61	4.81	0.62	24.731	2.00e-01	3.54e-02	9.80e-03
1.75-2.00	1.86	4.72	0.60	23.822	1.03e-01	3.21e-02	7.25e-03
2.00-2.50	2.20	4.77	0.62	24.448	6.73e-02	1.40e-02	3.81e-03

Table 5.6: continued

2.50-3.00	2.66	4.70	0.62	24.646	1.60e-02	9.68e-03	1.57e-03
3.00-3.50	3.30	4.93	0.67	26.580	1.57e-02	9.58e-03	2.52e-03
3.50-4.00	3.67	4.88	0.63	25.254	1.64e-02	1.16e-02	1.17e-02
p_T [GeV]	$< p_T >$	$< M >$	$< x_F >$	$< E >$	$5.20 \leq M_{\mu^+\mu^-} \leq 6.20$	Stat. Error.	Syst. Error
0.00-0.25	0.17	5.67	0.63	25.027	8.73e-01	9.90e-02	5.51e-02
0.25-0.50	0.38	5.69	0.62	24.668	9.47e-01	6.90e-02	4.34e-02
0.50-0.75	0.63	5.71	0.62	24.597	7.51e-01	4.52e-02	3.21e-02
0.75-1.00	0.87	5.70	0.62	24.795	5.30e-01	3.87e-02	1.95e-02
1.00-1.25	1.12	5.73	0.62	24.646	3.41e-01	2.75e-02	1.15e-02
1.25-1.50	1.36	5.71	0.62	24.700	2.30e-01	2.03e-02	8.16e-03
1.50-1.75	1.61	5.75	0.63	25.074	1.08e-01	1.43e-02	5.43e-03
1.75-2.00	1.88	5.69	0.61	24.352	5.90e-02	8.88e-03	3.68e-03
2.00-2.50	2.17	5.72	0.61	24.255	2.55e-02	3.88e-03	1.12e-03
2.50-3.00	2.73	5.69	0.61	24.371	5.26e-03	1.94e-03	7.89e-04
3.00-3.50	3.33	5.85	0.66	26.333	4.22e-03	1.57e-03	7.21e-04
3.50-4.00	3.74	5.40	0.64	25.676	3.07e-03	2.18e-03	8.02e-04
4.00-5.00	4.20	5.83	0.71	28.484	1.50e-03	1.50e-03	5.70e-04
p_T [GeV]	$< p_T >$	$< M >$	$< x_F >$	$< E >$	$6.20 \leq M_{\mu^+\mu^-} \leq 7.20$	Stat. Error.	Syst. Error
0.00-0.25	0.16	6.65	0.62	24.963	3.38e-01	4.39e-02	2.69e-02
0.25-0.50	0.39	6.64	0.63	25.195	3.69e-01	3.60e-02	1.48e-02
0.50-0.75	0.63	6.67	0.62	24.953	3.24e-01	2.41e-02	1.09e-02
0.75-1.00	0.87	6.65	0.62	24.933	2.79e-01	1.82e-02	9.13e-03
1.00-1.25	1.12	6.68	0.62	25.010	1.65e-01	1.31e-02	6.72e-03
1.25-1.50	1.37	6.67	0.62	24.847	8.91e-02	1.01e-02	4.80e-03
1.50-1.75	1.61	6.70	0.61	24.564	5.63e-02	6.72e-03	2.32e-03
1.75-2.00	1.86	6.64	0.62	24.857	3.50e-02	4.69e-03	1.45e-03

Table 5.6: continued

2.00-2.50	2.20	6.70	0.61	24.819	8.22e-03	1.77e-03	4.07e-04
2.50-3.00	2.70	6.64	0.61	24.863	4.86e-03	1.53e-03	2.53e-04
3.00-3.50	3.23	6.73	0.61	24.780	1.87e-03	7.67e-04	1.44e-04
3.50-4.00	3.62	6.76	0.60	24.599	9.29e-04	6.17e-04	3.42e-04
4.00-5.00	4.29	6.85	0.59	24.152	3.88e-04	3.07e-04	1.08e-04
p_T [GeV]	$< p_T >$	$< M >$	$< x_F >$	$< E >$	$7.20 \leq M_{\mu^+\mu^-} \leq 8.70$	Stat. Error.	Syst. Error
0.00-0.25	0.18	7.87	0.63	25.571	2.20e-01	3.02e-02	1.18e-02
0.25-0.50	0.38	7.79	0.62	25.230	2.34e-01	2.10e-02	8.44e-03
0.50-0.75	0.64	7.83	0.62	25.198	1.74e-01	1.50e-02	5.38e-03
0.75-1.00	0.88	7.85	0.61	25.090	1.46e-01	1.11e-02	4.86e-03
1.00-1.25	1.12	7.82	0.62	25.364	9.27e-02	8.34e-03	3.10e-03
1.25-1.50	1.37	7.91	0.61	25.161	5.32e-02	5.74e-03	1.83e-03
1.50-1.75	1.61	7.81	0.62	25.266	3.45e-02	4.14e-03	1.40e-03
1.75-2.00	1.86	7.82	0.61	25.098	2.41e-02	3.17e-03	9.33e-04
2.00-2.50	2.22	7.82	0.62	25.486	4.76e-03	1.01e-03	2.28e-04
2.50-3.00	2.72	7.78	0.62	25.371	2.11e-03	7.78e-04	8.39e-05
3.00-3.50	3.28	8.01	0.62	25.553	1.64e-03	5.08e-04	9.57e-05
3.50-4.00	3.72	7.83	0.61	25.046	9.17e-04	4.58e-04	1.03e-04
4.00-5.00	4.31	7.92	0.60	24.851	2.62e-04	4.27e-04	1.50e-04
5.00-6.00	5.51	7.44	0.58	24.190	2.08e-04	2.08e-04	9.57e-05
p_T [GeV]	$< p_T >$	$< M >$	$< x_F >$	$< E >$	$10.85 \leq M_{\mu^+\mu^-} \leq 12.85$	Stat. Error.	Syst. Error
0.00-0.25	0.21	11.20	0.62	26.684	8.62e-03	4.34e-03	7.43e-04
0.25-0.50	0.38	11.33	0.59	25.404	8.13e-03	2.76e-03	3.99e-04
0.50-0.75	0.64	11.50	0.60	26.056	9.56e-03	2.71e-03	4.70e-04
0.75-1.00	0.87	11.43	0.63	26.839	9.35e-03	2.61e-03	1.67e-03
1.00-1.25	1.10	11.38	0.63	26.864	3.26e-03	1.41e-03	1.54e-04

Table 5.6: continued

1.25-1.50	1.35	11.76	0.63	27.083	3.75e-03	1.19e-03	2.38e-04
1.50-1.75	1.57	11.49	0.61	26.375	3.71e-03	1.12e-03	2.21e-04
1.75-2.00	1.86	11.30	0.63	26.843	1.58e-03	5.06e-04	1.09e-04
2.00-2.50	2.31	11.49	0.64	27.573	4.19e-04	2.21e-04	2.37e-04
2.50-3.00	2.59	11.02	0.60	25.991	3.00e-04	3.00e-04	3.60e-05
3.00-3.50	3.14	11.24	0.61	26.422	6.62e-04	6.62e-04	1.07e-04
3.50-4.00	3.60	10.95	0.55	24.276	3.14e-05	3.14e-05	3.82e-06
p_T [GeV]	$< p_T >$	$< M >$	$< x_F >$	$< E >$	$12.85 \leq M_{\mu^+\mu^-} \leq 16.85$	Stat. Error.	Syst. Error
0.00-0.25	0.20	13.03	0.60	26.813	1.97e-02	1.97e-02	1.27e-02
0.25-0.50	0.38	13.73	0.67	29.495	7.02e-03	4.11e-03	8.60e-04
0.50-0.75	0.66	13.23	0.61	27.224	6.90e-03	3.45e-03	1.06e-03
0.75-1.00	0.88	13.89	0.63	28.152	1.69e-03	1.16e-03	1.52e-04
1.00-1.25	1.12	13.55	0.58	26.315	1.37e-03	1.09e-03	1.49e-04
1.25-1.50	1.33	13.01	0.64	28.196	9.64e-04	1.13e-03	1.12e-04
1.50-1.75	1.61	13.02	0.56	25.240	5.00e-04	5.00e-04	6.03e-05
2.00-2.50	2.24	13.28	0.71	30.505	3.34e-04	3.34e-04	4.89e-05

Table 5.7: Invariant form $Ed^3\sigma/dp^3$ (in units of pb / GeV^2 / nucleon) for the deuterium cross section for -0.05 $\leq x_F \leq$ 0.15. Statistical and point-to-point systematic uncertainties are shown. An additional $\pm$6.5% uncertainty in the normalization is common to all data points.

p_T [GeV]	$< p_T >$	$< M >$	$< x_F >$	$< E >$	$4.20 \leq M_{\mu^+\mu^-} \leq 5.20$	Stat. Error.	Syst. Error
0.00-0.25	0.16	4.66	0.11	6.456	1.35e+01	1.03e+00	8.93e-01
0.25-0.50	0.38	4.68	0.12	6.569	1.44e+01	7.84e-01	4.32e-01

Table 5.7: continued

0.50-0.75	0.62	4.66	0.12	6.588	1.25e+01	5.79e-01	3.76e-01
0.75-1.00	0.87	4.65	0.12	6.644	9.01e+00	4.29e-01	2.85e-01
1.00-1.25	1.12	4.64	0.12	6.694	6.82e+00	3.81e-01	2.15e-01
1.25-1.50	1.37	4.63	0.12	6.844	5.05e+00	3.24e-01	1.64e-01
1.50-1.75	1.63	4.66	0.12	6.771	2.16e+00	2.33e-01	9.04e-02
1.75-2.00	1.87	4.61	0.12	6.826	1.74e+00	2.22e-01	7.72e-02
2.00-2.50	2.22	4.59	0.12	6.956	9.53e-01	1.10e-01	4.21e-02
2.50-3.00	2.65	4.67	0.12	7.068	1.91e-01	5.35e-02	1.36e-02
3.50-4.00	3.70	4.60	0.12	7.442	2.20e-01	1.10e-01	6.12e-02
p_T [GeV]	$< p_T >$	$< M >$	$< x_F >$	$< E >$	$5.20 \leq M_{\mu^+\mu^-} \leq 6.20$	Stat. Error.	Syst. Error
0.00-0.25	0.16	5.55	0.11	7.116	4.36e+00	6.50e-01	2.97e-01
0.25-0.50	0.39	5.61	0.11	7.188	4.28e+00	3.69e-01	1.75e-01
0.50-0.75	0.63	5.60	0.12	7.249	4.11e+00	2.90e-01	1.54e-01
0.75-1.00	0.87	5.62	0.12	7.395	3.11e+00	2.47e-01	1.15e-01
1.00-1.25	1.12	5.65	0.12	7.384	1.63e+00	1.66e-01	6.78e-02
1.25-1.50	1.37	5.59	0.12	7.537	1.23e+00	1.63e-01	6.56e-02
1.50-1.75	1.62	5.65	0.12	7.527	9.74e-01	1.31e-01	8.31e-02
1.75-2.00	1.86	5.61	0.12	7.547	7.12e-01	1.17e-01	8.39e-02
2.00-2.50	2.25	5.63	0.12	7.644	4.42e-01	6.96e-02	5.71e-02
2.50-3.00	2.61	5.78	0.13	8.023	1.42e-01	4.76e-02	3.26e-02
3.00-3.50	3.15	5.54	0.13	8.066	3.99e-02	2.36e-02	1.30e-02
p_T [GeV]	$< p_T >$	$< M >$	$< x_F >$	$< E >$	$6.20 \leq M_{\mu^+\mu^-} \leq 7.20$	Stat. Error.	Syst. Error
0.00-0.25	0.18	6.69	0.10	7.819	1.31e+00	2.28e-01	1.08e-01
0.25-0.50	0.38	6.69	0.11	7.981	1.79e+00	1.91e-01	1.19e-01
0.50-0.75	0.63	6.74	0.10	7.960	1.34e+00	1.49e-01	7.59e-02
0.75-1.00	0.87	6.70	0.10	7.999	1.31e+00	1.18e-01	7.05e-02

Table 5.7: continued

1.00-1.25	1.11	6.71	0.10	8.011	6.17e-01	8.45e-02	6.31e-02
1.25-1.50	1.37	6.68	0.10	8.089	5.56e-01	8.99e-02	3.65e-02
1.50-1.75	1.62	6.82	0.12	8.464	3.18e-01	6.52e-02	4.46e-02
1.75-2.00	1.88	6.70	0.10	8.069	1.89e-01	4.09e-02	1.50e-02
2.00-2.50	2.13	6.66	0.09	8.017	9.92e-02	3.31e-02	9.85e-03
2.50-3.00	2.69	6.91	0.12	8.873	4.07e-02	1.59e-02	7.55e-03
3.00-3.50	3.21	6.91	0.12	8.902	4.33e-02	2.20e-02	1.74e-02
p_T [GeV]	$< p_T >$	$< M >$	$< x_F >$	$< E >$	$7.20 \leq M_{\mu^+\mu^-} \leq 8.70$	Stat. Error.	Syst. Error
0.00-0.25	0.16	8.10	0.09	8.987	8.63e-01	8.43e-02	5.27e-02
0.25-0.50	0.39	8.06	0.09	9.003	9.77e-01	5.96e-02	4.12e-02
0.50-0.75	0.63	8.05	0.09	9.015	9.64e-01	4.71e-02	2.86e-02
0.75-1.00	0.87	8.08	0.10	9.074	7.73e-01	3.58e-02	2.51e-02
1.00-1.25	1.12	8.08	0.10	9.162	5.83e-01	3.06e-02	2.30e-02
1.25-1.50	1.37	8.11	0.10	9.275	3.60e-01	2.23e-02	1.46e-02
1.50-1.75	1.61	8.06	0.10	9.283	2.54e-01	1.90e-02	1.09e-02
1.75-2.00	1.86	8.07	0.11	9.369	1.43e-01	1.51e-02	7.08e-03
2.00-2.50	2.23	8.13	0.11	9.558	8.54e-02	8.31e-03	3.24e-03
2.50-3.00	2.69	7.96	0.10	9.393	3.09e-02	5.21e-03	2.22e-03
3.00-3.50	3.21	8.10	0.11	9.708	1.24e-02	3.19e-03	1.91e-03
3.50-4.00	3.74	7.99	0.12	10.020	6.94e-03	3.25e-03	1.30e-03
4.00-5.00	4.25	8.57	0.10	10.455	2.11e-03	1.22e-03	5.46e-04
p_T [GeV]	$< p_T >$	$< M >$	$< x_F >$	$< E >$	$10.85 \leq M_{\mu^+\mu^-} \leq 12.85$	Stat. Error.	Syst. Error
0.00-0.25	0.19	11.13	0.04	11.595	4.74e-02	2.94e-02	9.09e-03
0.25-0.50	0.41	11.32	0.10	12.003	9.01e-02	2.85e-02	1.92e-02
0.50-0.75	0.63	11.13	0.10	11.857	1.01e-01	2.45e-02	3.02e-02
0.75-1.00	0.87	11.31	0.11	12.136	8.56e-02	2.53e-02	1.57e-02

Table 5.7: continued

1.00-1.25	1.12	11.15	0.11	12.091	4.04e-02	1.36e-02	4.23e-03
1.25-1.50	1.34	11.49	0.11	12.402	2.88e-02	1.13e-02	3.67e-03
1.50-1.75	1.61	11.23	0.12	12.307	3.24e-02	1.28e-02	4.91e-03
1.75-2.00	1.87	11.27	0.12	12.370	3.27e-02	1.37e-02	1.02e-02
2.00-2.50	2.26	11.65	0.13	12.853	1.22e-02	6.57e-03	1.04e-02
2.50-3.00	2.71	11.33	0.14	12.882	6.74e-02	4.77e-02	8.51e-02
3.00-3.50	3.49	11.13	0.12	12.537	3.48e-03	3.48e-03	2.55e-03

Table 5.8: Invariant form $Ed^3\sigma/dp^3$ (in units of pb / GeV^2 / nucleon) for the deuterium cross section for $0.15 \leq x_F \leq 0.35$. Statistical and point-to-point systematic uncertainties are shown. An additional $\pm 6.5\%$ uncertainty in the normalization is common to all data points.

p_T [GeV]	$< p_T >$	$< M >$	$< x_F >$	$< E >$	$4.20 \leq M_{\mu^+\mu^-} \leq 5.20$	Stat. Error.	Syst. Error
0.00-0.25	0.17	4.65	0.25	10.788	1.27e+01	4.92e-01	4.75e-01
0.25-0.50	0.39	4.66	0.25	10.855	1.42e+01	3.41e-01	4.20e-01
0.50-0.75	0.63	4.66	0.25	10.844	1.24e+01	2.58e-01	3.41e-01
0.75-1.00	0.87	4.66	0.25	10.844	8.91e+00	1.90e-01	2.41e-01
1.00-1.25	1.12	4.65	0.25	10.813	6.51e+00	1.47e-01	1.76e-01
1.25-1.50	1.37	4.65	0.25	10.752	4.28e+00	1.17e-01	1.20e-01
1.50-1.75	1.61	4.64	0.25	10.856	2.87e+00	9.27e-02	8.09e-02
1.75-2.00	1.87	4.64	0.25	10.903	1.81e+00	7.28e-02	5.54e-02
2.00-2.50	2.21	4.66	0.26	11.229	8.43e-01	3.86e-02	2.84e-02
2.50-3.00	2.71	4.65	0.26	11.449	3.39e-01	2.42e-02	1.96e-02
3.00-3.50	3.21	4.63	0.26	11.694	1.01e-01	1.76e-02	1.31e-02

Table 5.8: continued

3.50-4.00	3.75	4.61	0.28	12.354	4.07e-02	1.27e-02	7.20e-03
4.00-5.00	4.42	4.57	0.28	12.559	1.69e-02	5.90e-03	2.56e-03
5.00-6.00	5.38	4.78	0.27	12.854	5.47e-03	5.47e-03	2.55e-03
p_T [GeV]	$< p_T >$	$< M >$	$< x_F >$	$< E >$	$5.20 \leq M_{\mu^+\mu^-} \leq 6.20$	Stat. Error.	Syst. Error
0.00-0.25	0.16	5.66	0.27	12.052	4.85e+00	2.24e-01	2.13e-01
0.25-0.50	0.39	5.67	0.27	12.021	5.95e+00	1.57e-01	2.00e-01
0.50-0.75	0.63	5.68	0.27	12.058	4.86e+00	1.13e-01	1.53e-01
0.75-1.00	0.87	5.68	0.27	11.968	3.70e+00	8.79e-02	1.07e-01
1.00-1.25	1.12	5.69	0.27	12.061	2.81e+00	7.05e-02	7.91e-02
1.25-1.50	1.37	5.70	0.27	12.061	1.67e+00	5.41e-02	4.85e-02
1.50-1.75	1.61	5.70	0.27	12.075	1.11e+00	4.14e-02	3.31e-02
1.75-2.00	1.86	5.66	0.28	12.291	6.86e-01	3.38e-02	2.22e-02
2.00-2.50	2.21	5.70	0.27	12.328	3.26e-01	1.65e-02	1.21e-02
2.50-3.00	2.72	5.67	0.27	12.371	1.16e-01	1.08e-02	5.51e-03
3.00-3.50	3.21	5.60	0.27	12.230	3.27e-02	5.34e-03	7.88e-03
3.50-4.00	3.72	5.75	0.29	13.320	3.02e-02	5.59e-03	8.07e-03
4.00-5.00	4.37	5.62	0.31	13.879	5.33e-03	2.33e-03	6.22e-03
5.00-6.00	5.36	5.61	0.30	13.873	7.66e-03	7.66e-03	3.92e-03
p_T [GeV]	$< p_T >$	$< M >$	$< x_F >$	$< E >$	$6.20 \leq M_{\mu^+\mu^-} \leq 7.20$	Stat. Error.	Syst. Error
0.00-0.25	0.17	6.68	0.27	12.585	1.94e+00	9.54e-02	1.30e-01
0.25-0.50	0.39	6.69	0.27	12.582	2.43e+00	6.90e-02	1.01e-01
0.50-0.75	0.63	6.69	0.28	12.674	1.98e+00	4.98e-02	8.25e-02
0.75-1.00	0.87	6.70	0.27	12.606	1.61e+00	3.93e-02	6.81e-02
1.00-1.25	1.12	6.70	0.27	12.637	1.15e+00	3.03e-02	4.01e-02
1.25-1.50	1.36	6.71	0.27	12.660	7.19e-01	2.30e-02	2.10e-02
1.50-1.75	1.62	6.72	0.27	12.675	4.95e-01	1.83e-02	2.03e-02

Table 5.8: continued

1.75-2.00	1.87	6.72	0.28	12.793	2.94e-01	1.42e-02	1.57e-02
2.00-2.50	2.21	6.72	0.28	12.934	1.66e-01	7.35e-03	5.23e-03
2.50-3.00	2.70	6.74	0.27	12.947	6.35e-02	4.49e-03	2.65e-03
3.00-3.50	3.20	6.66	0.27	12.911	2.66e-02	2.98e-03	1.69e-03
3.50-4.00	3.73	6.82	0.27	13.075	4.84e-03	1.37e-03	8.00e-04
4.00-5.00	4.23	6.73	0.29	13.745	2.99e-03	9.76e-04	4.94e-04
5.00-6.00	5.06	7.09	0.35	16.081	1.34e-03	1.45e-03	3.15e-03
p_T [GeV]	$< p_T >$	$< M >$	$< x_F >$	$< E >$	$7.20 \leq M_{\mu^+\mu^-} \leq 8.70$	Stat. Error.	Syst. Error
0.00-0.25	0.16	7.90	0.26	12.756	1.07e+00	5.25e-02	4.67e-02
0.25-0.50	0.39	7.89	0.26	12.777	1.23e+00	3.59e-02	4.29e-02
0.50-0.75	0.63	7.87	0.26	12.805	1.12e+00	2.71e-02	3.21e-02
0.75-1.00	0.87	7.87	0.26	12.845	8.73e-01	2.03e-02	3.59e-02
1.00-1.25	1.12	7.87	0.26	12.899	6.09e-01	1.53e-02	2.23e-02
1.25-1.50	1.37	7.89	0.26	12.933	4.30e-01	1.19e-02	1.19e-02
1.50-1.75	1.62	7.90	0.26	13.020	2.88e-01	9.13e-03	8.20e-03
1.75-2.00	1.87	7.93	0.26	13.036	1.90e-01	7.04e-03	5.61e-03
2.00-2.50	2.21	7.89	0.26	13.051	9.25e-02	3.44e-03	3.91e-03
2.50-3.00	2.72	7.93	0.26	13.186	4.03e-02	2.28e-03	3.00e-03
3.00-3.50	3.21	7.94	0.26	13.457	1.59e-02	1.43e-03	1.31e-03
3.50-4.00	3.68	8.22	0.25	13.366	3.37e-03	8.14e-04	2.26e-04
4.00-5.00	4.45	7.87	0.28	14.118	2.59e-03	5.15e-04	7.51e-04
5.00-6.00	5.30	7.91	0.27	14.123	8.93e-04	4.65e-04	7.22e-04
p_T [GeV]	$< p_T >$	$< M >$	$< x_F >$	$< E >$	$10.85 \leq M_{\mu^+\mu^-} \leq 12.85$	Stat. Error.	Syst. Error
0.00-0.25	0.15	11.49	0.26	15.472	6.21e-02	1.40e-02	8.00e-03
0.25-0.50	0.38	11.42	0.27	15.690	1.12e-01	1.33e-02	1.01e-02
0.50-0.75	0.64	11.39	0.27	15.487	7.81e-02	9.09e-03	4.52e-03

Table 5.8: continued

0.75-1.00	0.87	11.44	0.27	15.719	7.01e-02	6.93e-03	5.63e-03
1.00-1.25	1.12	11.41	0.28	15.759	5.44e-02	5.24e-03	6.89e-03
1.25-1.50	1.38	11.41	0.26	15.393	3.13e-02	3.72e-03	2.87e-03
1.50-1.75	1.62	11.39	0.27	15.729	2.19e-02	3.34e-03	3.08e-03
1.75-2.00	1.87	11.47	0.29	16.177	1.57e-02	2.63e-03	3.28e-03
2.00-2.50	2.22	11.42	0.26	15.592	7.04e-03	1.01e-03	1.14e-03
2.50-3.00	2.73	11.25	0.25	15.216	2.06e-03	5.37e-04	5.23e-04
3.00-3.50	3.20	11.35	0.25	15.369	9.92e-04	4.02e-04	2.63e-04
3.50-4.00	3.66	11.37	0.31	17.000	5.29e-04	3.12e-04	9.67e-05
4.00-5.00	4.21	11.17	0.33	17.418	2.25e-04	2.25e-04	2.20e-04
p_T [GeV]	$< p_T >$	$< M >$	$< x_F >$	$< E >$	$12.85 \leq M_{\mu^+\mu^-} \leq 16.85$	Stat. Error.	Syst. Error
0.00-0.25	0.21	13.63	0.26	17.097	2.41e-02	2.23e-02	9.04e-03
0.25-0.50	0.34	13.16	0.28	17.161	1.50e-02	1.36e-02	4.06e-03
0.50-0.75	0.64	13.10	0.28	17.006	2.33e-02	2.77e-02	3.15e-03
0.75-1.00	0.88	13.48	0.31	18.132	4.91e-02	1.49e-02	1.35e-03
1.00-1.25	1.10	13.58	0.24	16.468	1.09e-02	5.88e-03	2.04e-03
1.25-1.50	1.34	13.49	0.28	17.375	2.08e-02	8.25e-03	2.68e-03
1.50-1.75	1.58	13.31	0.30	17.868	6.07e-03	3.36e-03	1.73e-03
1.75-2.00	1.86	13.45	0.30	17.818	3.73e-02	2.64e-02	1.30e-02
2.00-2.50	2.45	13.25	0.35	19.118	2.86e-03	2.86e-03	2.60e-04
2.50-3.00	2.95	13.08	0.27	17.073	2.02e-02	2.02e-02	5.17e-04

Table 5.9: Invariant form $Ed^3\sigma/dp^3$ (in units of pb / GeV^2 / nucleon) for the deuterium cross section for $0.35 \leq x_F \leq 0.55$. Statistical and point-to-point systematic uncertainties are shown. An additional $\pm 6.5\%$ uncertainty in the normalization is common to all data points.

p_T [GeV]	$< p_T >$	$< M >$	$< x_F >$	$< E >$	$4.20 \leq M_{\mu^+\mu^-} \leq 5.20$	Stat. Error.	Syst. Error
0.00-0.25	0.16	4.74	0.43	17.465	8.63e+00	4.41e-01	6.65e-01
0.25-0.50	0.38	4.75	0.43	17.338	9.61e+00	3.03e-01	3.35e-01
0.50-0.75	0.63	4.74	0.43	17.430	7.31e+00	2.04e-01	2.13e-01
0.75-1.00	0.87	4.73	0.43	17.416	5.68e+00	1.60e-01	1.75e-01
1.00-1.25	1.12	4.74	0.43	17.371	3.67e+00	1.16e-01	1.64e-01
1.25-1.50	1.37	4.73	0.43	17.455	2.33e+00	8.90e-02	1.11e-01
1.50-1.75	1.61	4.72	0.43	17.482	1.28e+00	6.67e-02	4.15e-02
1.75-2.00	1.87	4.74	0.43	17.396	7.94e-01	4.85e-02	2.77e-02
2.00-2.50	2.20	4.72	0.43	17.313	3.12e-01	2.15e-02	1.30e-02
2.50-3.00	2.70	4.73	0.42	17.216	1.14e-01	1.32e-02	5.38e-03
3.00-3.50	3.22	4.73	0.44	17.841	5.37e-02	8.42e-03	3.55e-03
3.50-4.00	3.69	4.70	0.40	16.494	1.71e-02	5.07e-03	2.73e-03
4.00-5.00	4.42	4.64	0.43	17.756	4.00e-03	2.04e-03	3.08e-03
p_T [GeV]	$< p_T >$	$< M >$	$< x_F >$	$< E >$	$5.20 \leq M_{\mu^+\mu^-} \leq 6.20$	Stat. Error.	Syst. Error
0.00-0.25	0.16	5.71	0.44	17.995	3.23e+00	1.33e-01	1.15e-01
0.25-0.50	0.39	5.71	0.44	17.907	3.81e+00	9.07e-02	1.14e-01
0.50-0.75	0.63	5.72	0.44	17.875	3.10e+00	6.83e-02	9.26e-02
0.75-1.00	0.87	5.72	0.44	17.881	2.20e+00	4.97e-02	6.17e-02
1.00-1.25	1.12	5.72	0.44	17.983	1.59e+00	3.86e-02	4.35e-02
1.25-1.50	1.37	5.72	0.44	17.948	9.18e-01	2.86e-02	2.62e-02
1.50-1.75	1.61	5.72	0.43	17.844	5.93e-01	2.22e-02	1.77e-02

Table 5.9: continued

1.75-2.00	1.87	5.70	0.43	17.877	3.35e-01	1.64e-02	1.17e-02
2.00-2.50	2.22	5.73	0.43	17.876	1.62e-01	8.15e-03	5.91e-03
2.50-3.00	2.71	5.76	0.43	18.006	5.66e-02	4.68e-03	2.66e-03
3.00-3.50	3.19	5.72	0.44	18.145	1.05e-02	2.38e-03	9.71e-04
3.50-4.00	3.68	5.67	0.44	18.217	6.48e-03	1.72e-03	8.23e-04
4.00-5.00	4.35	5.74	0.43	18.107	1.84e-03	5.86e-04	6.55e-04
6.00-7.00	6.08	6.10	0.40	17.758	2.38e-04	2.51e-04	4.85e-04
p_T [GeV]	$< p_T >$	$< M >$	$< x_F >$	$< E >$	$6.20 \leq M_{\mu^+\mu^-} \leq 7.20$	Stat. Error.	Syst. Error
0.00-0.25	0.17	6.65	0.44	18.312	1.36e+00	5.98e-02	4.62e-02
0.25-0.50	0.39	6.64	0.44	18.275	1.50e+00	4.17e-02	4.46e-02
0.50-0.75	0.63	6.67	0.44	18.292	1.30e+00	3.06e-02	3.62e-02
0.75-1.00	0.87	6.67	0.44	18.305	9.66e-01	2.35e-02	2.63e-02
1.00-1.25	1.12	6.68	0.44	18.218	7.17e-01	1.77e-02	1.95e-02
1.25-1.50	1.37	6.68	0.43	18.205	4.26e-01	1.31e-02	1.21e-02
1.50-1.75	1.61	6.68	0.43	18.202	2.90e-01	1.03e-02	9.40e-03
1.75-2.00	1.87	6.70	0.43	18.157	1.57e-01	7.45e-03	5.68e-03
2.00-2.50	2.21	6.71	0.43	18.244	7.50e-02	3.47e-03	2.60e-03
2.50-3.00	2.70	6.72	0.43	18.169	2.60e-02	1.97e-03	1.39e-03
3.00-3.50	3.19	6.71	0.43	18.449	1.08e-02	1.33e-03	7.07e-04
3.50-4.00	3.69	6.68	0.42	18.088	3.55e-03	7.31e-04	3.86e-04
4.00-5.00	4.26	6.68	0.45	19.144	1.45e-03	3.46e-04	2.83e-04
5.00-6.00	5.55	6.58	0.41	17.946	1.75e-04	1.75e-04	8.61e-05
p_T [GeV]	$< p_T >$	$< M >$	$< x_F >$	$< E >$	$7.20 \leq M_{\mu^+\mu^-} \leq 8.70$	Stat. Error.	Syst. Error
0.00-0.25	0.16	7.84	0.44	18.819	7.58e-01	3.95e-02	5.35e-02
0.25-0.50	0.38	7.88	0.44	18.765	9.06e-01	2.80e-02	3.11e-02
0.50-0.75	0.63	7.85	0.44	18.781	7.89e-01	2.02e-02	2.26e-02

Table 5.9: continued

0.75-1.00	0.88	7.85	0.44	18.734	5.83e-01	1.46e-02	1.59e-02
1.00-1.25	1.12	7.87	0.44	18.731	4.24e-01	1.14e-02	1.15e-02
1.25-1.50	1.37	7.86	0.43	18.653	2.89e-01	8.56e-03	7.86e-03
1.50-1.75	1.62	7.89	0.43	18.680	1.65e-01	6.00e-03	4.59e-03
1.75-2.00	1.87	7.85	0.44	18.779	1.17e-01	4.85e-03	3.51e-03
2.00-2.50	2.21	7.89	0.44	18.804	5.34e-02	2.24e-03	1.54e-03
2.50-3.00	2.70	7.87	0.43	18.748	1.95e-02	1.28e-03	7.02e-04
3.00-3.50	3.19	7.93	0.43	18.890	6.28e-03	7.44e-04	2.66e-04
3.50-4.00	3.71	7.88	0.43	18.772	2.50e-03	4.32e-04	1.85e-04
4.00-5.00	4.36	7.88	0.43	18.936	1.17e-03	2.42e-04	1.53e-04
5.00-6.00	5.26	7.98	0.43	19.251	2.03e-04	9.31e-05	1.21e-04
p_T [GeV]	$< p_T >$	$< M >$	$< x_F >$	$< E >$	$10.85 \leq M_{\mu^+\mu^-} \leq 12.85$	Stat. Error.	Syst. Error
0.00-0.25	0.17	11.56	0.45	20.901	4.24e-02	1.13e-02	4.63e-03
0.25-0.50	0.39	11.51	0.44	20.469	7.26e-02	7.40e-03	3.50e-03
0.50-0.75	0.62	11.58	0.45	20.859	6.28e-02	5.58e-03	4.80e-03
0.75-1.00	0.88	11.43	0.45	20.832	4.29e-02	4.11e-03	4.31e-03
1.00-1.25	1.12	11.59	0.45	20.858	3.51e-02	2.98e-03	2.61e-03
1.25-1.50	1.37	11.47	0.44	20.595	2.36e-02	2.43e-03	1.22e-03
1.50-1.75	1.63	11.55	0.44	20.653	1.30e-02	1.91e-03	8.16e-04
1.75-2.00	1.85	11.41	0.44	20.675	1.01e-02	1.53e-03	1.60e-03
2.00-2.50	2.21	11.52	0.44	20.770	4.41e-03	5.59e-04	6.29e-04
2.50-3.00	2.71	11.37	0.44	20.761	1.40e-03	2.73e-04	2.65e-04
3.00-3.50	3.18	11.69	0.45	21.149	4.98e-04	2.34e-04	3.85e-05
3.50-4.00	3.57	11.34	0.40	19.469	3.51e-04	2.07e-04	5.26e-05
4.00-5.00	4.23	11.83	0.41	20.241	6.69e-05	4.32e-05	1.62e-05
p_T [GeV]	$< p_T >$	$< M >$	$< x_F >$	$< E >$	$12.85 \leq M_{\mu^+\mu^-} \leq 16.85$	Stat. Error.	Syst. Error

Table 5.9: continued

0.00-0.25	0.15	13.83	0.45	22.325	4.21e-02	1.54e-02	5.61e-03
0.25-0.50	0.40	13.34	0.46	22.267	2.18e-02	9.75e-03	6.32e-04
0.50-0.75	0.64	13.76	0.46	22.449	1.85e-02	4.48e-03	1.08e-03
0.75-1.00	0.87	13.93	0.45	22.507	9.92e-03	2.88e-03	5.70e-04
1.00-1.25	1.08	13.33	0.44	21.690	5.75e-03	2.25e-03	3.79e-04
1.25-1.50	1.37	13.72	0.44	22.071	8.60e-03	2.21e-03	5.42e-04
1.50-1.75	1.63	13.49	0.45	22.199	6.57e-03	1.94e-03	4.84e-04
1.75-2.00	1.88	13.77	0.47	23.052	2.88e-03	1.19e-03	1.43e-04
2.00-2.50	2.27	13.68	0.43	21.676	9.69e-04	6.04e-04	6.87e-05
2.50-3.00	2.79	14.13	0.45	22.798	3.52e-04	2.14e-04	6.36e-05
3.00-3.50	3.04	13.99	0.51	24.267	5.10e-04	3.61e-04	9.74e-05

Table 5.10: Invariant form $Ed^3\sigma/dp^3$ (in units of pb / GeV^2 / nucleon) for the deuterium cross section for $0.55 \leq x_F \leq 0.8$. Statistical and point-to-point systematic uncertainties are shown. An additional $\pm 6.5\%$ uncertainty in the normalization is common to all data points.

p_T [GeV]	$< p_T >$	$< M >$	$< x_F >$	$< E >$	$4.20 \leq M_{\mu^+\mu^-} \leq 5.20$	Stat. Error.	Syst. Error
0.00-0.25	0.17	4.86	0.63	24.768	1.87e+00	1.98e-01	2.17e-01
0.25-0.50	0.38	4.80	0.62	24.530	2.43e+00	1.57e-01	1.45e-01
0.50-0.75	0.63	4.80	0.62	24.519	2.11e+00	1.11e-01	9.94e-02
0.75-1.00	0.87	4.79	0.62	24.617	1.35e+00	7.68e-02	5.95e-02
1.00-1.25	1.12	4.75	0.62	24.357	8.18e-01	5.43e-02	3.50e-02
1.25-1.50	1.36	4.76	0.62	24.526	4.82e-01	3.97e-02	2.05e-02
1.50-1.75	1.61	4.81	0.62	24.426	3.07e-01	2.91e-02	1.34e-02

Table 5.10: continued

1.75-2.00	1.88	4.77	0.62	24.499	1.69e-01	2.32e-02	8.97e-03
2.00-2.50	2.22	4.71	0.61	24.381	6.25e-02	8.96e-03	3.70e-03
2.50-3.00	2.68	4.71	0.63	24.876	2.10e-02	5.21e-03	2.21e-03
3.00-3.50	3.19	4.94	0.61	24.447	9.63e-03	3.94e-03	1.46e-03
3.50-4.00	3.76	4.33	0.57	22.878	2.57e-03	2.57e-03	5.88e-04
p_T [GeV]	$< p_T >$	$< M >$	$< x_F >$	$< E >$	$5.20 \leq M_{\mu^+\mu^-} \leq 6.20$	Stat. Error.	Syst. Error
0.00-0.25	0.16	5.71	0.62	24.865	8.35e-01	6.26e-02	3.81e-02
0.25-0.50	0.39	5.71	0.62	24.850	1.01e+00	4.44e-02	4.13e-02
0.50-0.75	0.62	5.71	0.62	24.878	8.12e-01	3.13e-02	3.61e-02
0.75-1.00	0.87	5.72	0.62	24.719	5.50e-01	2.43e-02	2.00e-02
1.00-1.25	1.12	5.72	0.62	24.580	3.68e-01	1.77e-02	1.26e-02
1.25-1.50	1.37	5.76	0.62	24.669	2.04e-01	1.23e-02	7.21e-03
1.50-1.75	1.62	5.69	0.62	24.742	1.18e-01	9.19e-03	6.14e-03
1.75-2.00	1.87	5.68	0.61	24.344	7.54e-02	6.63e-03	4.55e-03
2.00-2.50	2.22	5.72	0.60	24.003	2.57e-02	2.60e-03	1.12e-03
2.50-3.00	2.70	5.78	0.60	24.191	9.18e-03	1.65e-03	6.38e-04
3.00-3.50	3.13	5.77	0.60	24.291	1.87e-03	7.23e-04	2.85e-04
3.50-4.00	3.80	5.63	0.60	24.228	1.39e-03	6.01e-04	2.14e-04
4.00-5.00	4.28	5.44	0.61	24.584	6.68e-04	4.77e-04	2.73e-04
5.00-6.00	5.20	5.20	0.58	23.539	8.94e-05	8.94e-05	4.32e-05
p_T [GeV]	$< p_T >$	$< M >$	$< x_F >$	$< E >$	$6.20 \leq M_{\mu^+\mu^-} \leq 7.20$	Stat. Error.	Syst. Error
0.00-0.25	0.16	6.67	0.62	24.848	3.72e-01	2.94e-02	2.95e-02
0.25-0.50	0.39	6.68	0.62	25.117	4.08e-01	2.24e-02	1.52e-02
0.50-0.75	0.63	6.68	0.62	25.057	3.27e-01	1.51e-02	1.14e-02
0.75-1.00	0.87	6.68	0.62	24.953	2.68e-01	1.16e-02	8.92e-03
1.00-1.25	1.12	6.67	0.62	25.048	1.83e-01	8.74e-03	7.14e-03

Table 5.10: continued

1.25-1.50	1.37	6.68	0.62	24.898	1.07e-01	6.52e-03	4.26e-03
1.50-1.75	1.62	6.67	0.62	24.864	4.77e-02	3.97e-03	1.90e-03
1.75-2.00	1.86	6.68	0.61	24.666	3.51e-02	3.05e-03	1.35e-03
2.00-2.50	2.22	6.69	0.61	24.696	1.46e-02	1.48e-03	6.16e-04
2.50-3.00	2.69	6.71	0.62	25.020	1.47e-03	4.78e-04	8.58e-05
3.00-3.50	3.17	6.66	0.62	25.152	1.97e-03	5.49e-04	1.53e-04
3.50-4.00	3.79	6.76	0.64	25.814	8.57e-04	3.98e-04	1.09e-04
4.00-5.00	4.19	6.61	0.62	25.158	1.83e-04	2.79e-04	4.14e-05
p_T [GeV]	$< p_T >$	$< M >$	$< x_F >$	$< E >$	$7.20 \leq M_{\mu^+\mu^-} \leq 8.70$	Stat. Error.	Syst. Error
0.00-0.25	0.17	7.80	0.62	25.221	2.22e-01	1.99e-02	9.47e-03
0.25-0.50	0.38	7.87	0.62	25.263	2.65e-01	1.43e-02	9.33e-03
0.50-0.75	0.63	7.87	0.62	25.279	1.87e-01	9.69e-03	5.86e-03
0.75-1.00	0.87	7.86	0.62	25.139	1.50e-01	7.25e-03	4.79e-03
1.00-1.25	1.12	7.87	0.62	25.355	1.10e-01	5.56e-03	3.50e-03
1.25-1.50	1.36	7.82	0.61	25.103	6.43e-02	3.92e-03	2.19e-03
1.50-1.75	1.62	7.86	0.61	25.116	3.56e-02	2.61e-03	1.34e-03
1.75-2.00	1.87	7.88	0.62	25.288	2.32e-02	2.00e-03	8.73e-04
2.00-2.50	2.20	7.88	0.62	25.242	8.51e-03	8.18e-04	3.37e-04
2.50-3.00	2.70	7.87	0.61	24.942	2.80e-03	4.92e-04	1.12e-04
3.00-3.50	3.26	7.90	0.61	25.003	1.23e-03	3.06e-04	7.02e-05
3.50-4.00	3.73	7.67	0.61	25.151	1.22e-04	9.33e-05	1.05e-05
4.00-5.00	4.24	7.65	0.59	24.606	1.25e-04	1.04e-04	3.65e-05
p_T [GeV]	$< p_T >$	$< M >$	$< x_F >$	$< E >$	$10.85 \leq M_{\mu^+\mu^-} \leq 12.85$	Stat. Error.	Syst. Error
0.00-0.25	0.16	11.52	0.64	27.216	1.44e-02	4.51e-03	1.24e-03
0.25-0.50	0.41	11.60	0.62	26.670	1.61e-02	2.68e-03	1.65e-03
0.50-0.75	0.63	11.70	0.63	27.097	1.49e-02	2.38e-03	1.74e-03

Table 5.10: continued

0.75-1.00	0.87	11.58	0.64	27.446	1.29e-02	1.98e-03	1.68e-03
1.00-1.25	1.12	11.53	0.62	26.604	6.25e-03	1.06e-03	2.89e-04
1.25-1.50	1.37	11.63	0.62	26.815	5.50e-03	9.86e-04	6.61e-04
1.50-1.75	1.58	11.68	0.62	26.747	4.29e-03	8.30e-04	2.54e-04
1.75-2.00	1.87	11.70	0.62	26.881	9.95e-04	2.83e-04	2.04e-04
2.00-2.50	2.15	11.67	0.60	26.023	1.06e-03	2.24e-04	6.12e-05
2.50-3.00	2.80	11.36	0.61	26.431	2.80e-04	1.39e-04	2.38e-05
3.00-3.50	3.31	12.21	0.60	26.456	1.46e-04	1.03e-04	6.36e-06
3.50-4.00	3.83	12.27	0.80	33.552	2.71e-04	2.71e-04	1.02e-05

p_T [GeV]	$< p_T >$	$< M >$	$< x_F >$	$< E >$	$12.85 \leq M_{\mu^+\mu^-} \leq 16.85$	Stat. Error.	Syst. Error
0.00-0.25	0.14	14.46	0.62	27.955	3.32e-02	1.97e-02	2.14e-02
0.25-0.50	0.37	13.42	0.60	26.899	2.82e-03	1.77e-03	3.48e-04
0.50-0.75	0.62	13.79	0.63	27.915	5.32e-03	1.60e-03	5.34e-04
0.75-1.00	0.88	13.35	0.59	26.661	2.37e-03	9.32e-04	2.15e-04
1.00-1.25	1.09	13.35	0.62	27.545	2.26e-03	7.94e-04	1.91e-04
1.25-1.50	1.40	13.17	0.65	28.395	4.50e-03	2.60e-03	1.17e-04
1.50-1.75	1.64	13.43	0.62	27.718	1.20e-03	4.93e-04	1.23e-04
1.75-2.00	1.88	13.35	0.61	27.239	3.15e-04	1.91e-04	2.67e-05
2.00-2.50	2.18	13.31	0.58	26.362	2.12e-04	1.15e-04	1.97e-05
2.50-3.00	2.76	13.10	0.61	27.138	7.51e-05	6.00e-05	1.25e-05
3.00-3.50	3.29	16.01	0.64	29.691	4.55e-04	4.55e-04	4.93e-04
3.50-4.00	3.66	15.77	0.61	28.534	4.06e-05	4.06e-05	1.43e-05

6 DISCUSSION

In the thirty years since the seminal experiment by Christenson *et al.* [Chr 70], the Drell-Yan process for continuum dilepton production in hadronic interactions remains an active area of experimental and theoretical investigation. Several experiments have studied both pion- and proton-induced dileptons, providing a wealth of data utilizing various beams, targets and center-of-mass energies. When these data are analyzed within the framework of perturbative QCD along with data from other types of hadronic interactions, they provide a powerful tool for extracting information about the parton distribution functions.

In the preceding chapters we have described the procedures used in and reported the results of a measurement of continuum diumon cross sections in 800-GeV pp and pd interactions. In this chapter, we compare our results to existing dimuon data from pA and pd measurements performed by the CERN NA3 [Bad 83], FNAL E605 [Mor 91] and FNAL E772 [McG 94] experiments. Fermilab E866 has already published [Haw 98, Tow 01] results on the deuterium-to-hydrogen cross section ratio, and we will also demonstrate that our absolute measurements are consistent with those previous results. We will also discuss the level of agreement between our results and next-to-leading order calculations of the cross sections based on various sets of parton distribution fits. We will highlight some important differences between data and theory, and discuss the likely

impact our results will have on future fits to the parton distributions.

6.1 Comparison with Other Experiments

Following the work of Christenson *et al.*, several experiments measured Drell-Yan cross sections using various beams and targets. The first high-statistics measurements to study the Drell-Yan process over an extended range of kinematics examined dimuon production in pA interactions. CERN NA3 [Bad 83] studied pPt at $\sqrt{s} = 27.4$ GeV, while Fermilab E605 [Mor 91] studied pCu at $\sqrt{s} = 38.8$ GeV. Less extensive measurements of the pp and pd cross sections in a narrow x_F range centered around $x_F = 0$ were also carried out at CERN. CERN R-209 [Ant 82] studied the pp cross sections at $\sqrt{s} = 44$ and 62 GeV, while CERN NA51 [Bal 94] studied the pp and pd cross sections[1] at $\sqrt{s} = 29$ GeV. In the early 1990's, the pd cross sections were measured over a wide range of mass and x_F by the Fermilab E772 collaboration [McG 94]. They published results spanning the range $0.05 \leq x_F \leq 0.7$ based on an $83,000$ event dimuon sample. It is important to note that the E605 and E772 measurements were conducted using essentially the same apparatus as E866. Thus, these two experiments provide important cross checks on the consistency of our results.

Figures 6.1 and 6.2 compare the E866 measurements of the scaling form of

[1] CERN NA51 did not publish absolute measurements, only the asymmetry between pp and pd cross sections.

the cross section $M^3 d^2\sigma/dMdx_F$ in pd interactions to the NA3, E605 and E772 measurements. The data are plotted versus the scaling variable $\sqrt{\tau}$ to enable a direct comparison between the results measured at different $\sqrt{s}$. The E866 data, which are subject to an additional $\pm 6.5\%$ global normalization uncertainty, are in good agreement with these previous dimuon experiments over a broad range of mass and x_F. The E605, E772 and E866 data typically agree to within less than the quoted normalization uncertainties[2] of the three experiments. The only major area of disagreement is at larger values of x_F and smaller masses, where the E866 measurement differs significantly from the E772 results. In this kinematic region, the E772 measurement is subject to larger systematic uncertainties ($\sim 20\%$) [**?**]. The major differences between E772 and E866 in this region are thought to be primarily due to uncertainties in the E772 magnetic field maps [McG].

Because the E772 and E866 measurements used essentially the same apparatus it is worth exploring this difference in a little more detail. Figure 6.3 shows the results from the low- and high-mass data settings used in E866, and the published E772 results. They are shown over the range $0.4 \leq x_F < 0.5$ where the discrepancy is most pronounced. The two E866 mass settings have very different acceptances. The acceptance in the high-mass data is plunging rapidly with decreasing mass, while the low-mass acceptance is fairly large in the same region. The agreement

[2]We expect the systematic uncertainties in the normalization of these three experiments to be correlated at some level, since they used the same beam line monitors to calibrate the data, and some of the same calibration measurements are common.

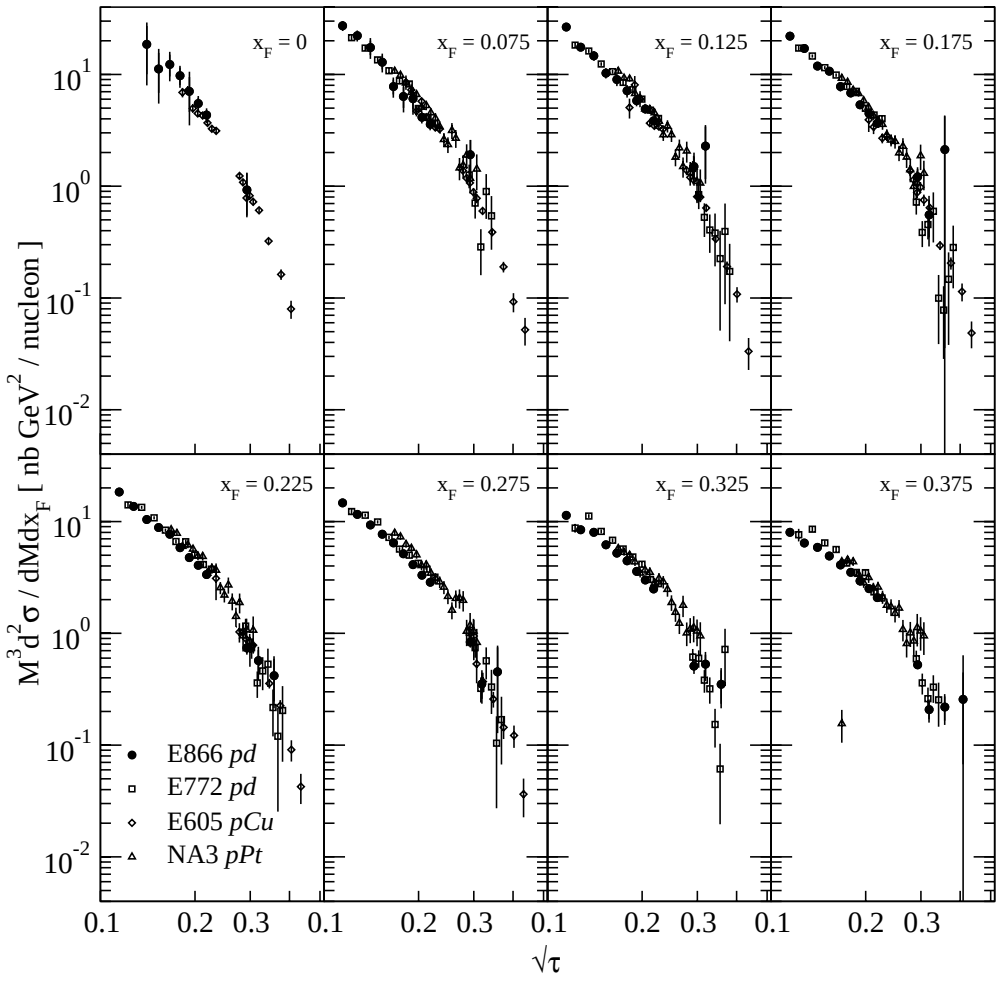

Figure 6.1: Scaling form $M^3 d^2\sigma/dMdx_F$ plotted versus $\sqrt{\tau}$ for the E866 pd, E772 pd [McG 94], E605 pCu [Mor 91] and NA3 pPt [Bad 83] measurements. Errors are statistical only, except for the E866 uncertainties which are the linear sum of statistical and systematic uncertainties. The E866 data contain an additional $\pm 6.5\%$ systematic uncertainty in the normalization.

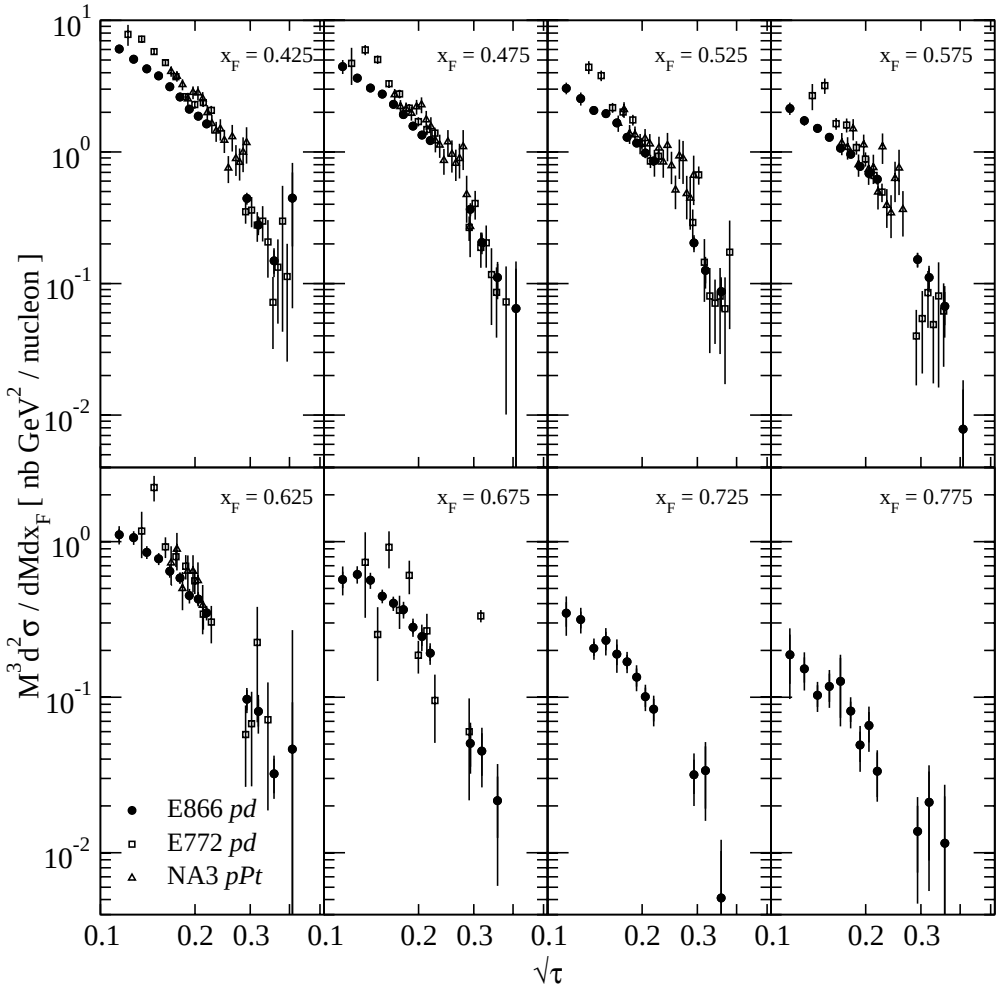

Figure 6.2: Scaling form $M^3 d^2\sigma/dMdx_F$ plotted versus $\sqrt{\tau}$ for the E866 pd, E772 pd [McG 94], and NA3 pPt [Bad 83] measurements. Errors are statistical only, except for the E866 uncertainties which are the linear sum of the statistical and systematic uncertainties. The E866 data contain an additional $\pm 6.5\%$ systematic uncertainty in the normalization.

between these data sets is quite good, suggesting that the E866 data is generally free of the systematic uncertainties present in the E772 data in this region.

Fermilab E772 has also published measurements of the triple-differential cross section $Ed^3\sigma/dp^3$, over a more restricted kinematic range ($0.1 \leq x_F \leq 0.3$) than their double-differential measurements. This range is below the x_F range where the E772 and E866 measurements disagree, and was imposed on E772 by correlations between their x_F and p_T acceptance [McG], which was much less of a concern in the E866 data. In the previous chapter we tabulated $Ed^3\sigma/dp^3$ in various x_F bins covering our entire x_F range. To make a direct comparison between our results and those of E772, we recalculated our cross sections using the E772 binning. These results are shown in figure 6.4 along with the E772 measurement. In general, there is excellent agreement between the two experiments. Only as $p_T \to 0$ GeV do the two experiments disagree. The cross sections in this region are highly sensitive to the precise alignment of the beam. Uncertainties in either or both the beam position and angle would lead to systematic shifts in the p_T of each event. Thus, the differences between the two measurements may be due to beam alignment issues in the two experiments.

6.2 Cross Section Ratios

We turn now to a comparison of our absolute measurements with the previously published cross section ratios. The primary goal of Fermilab E866 was to measure

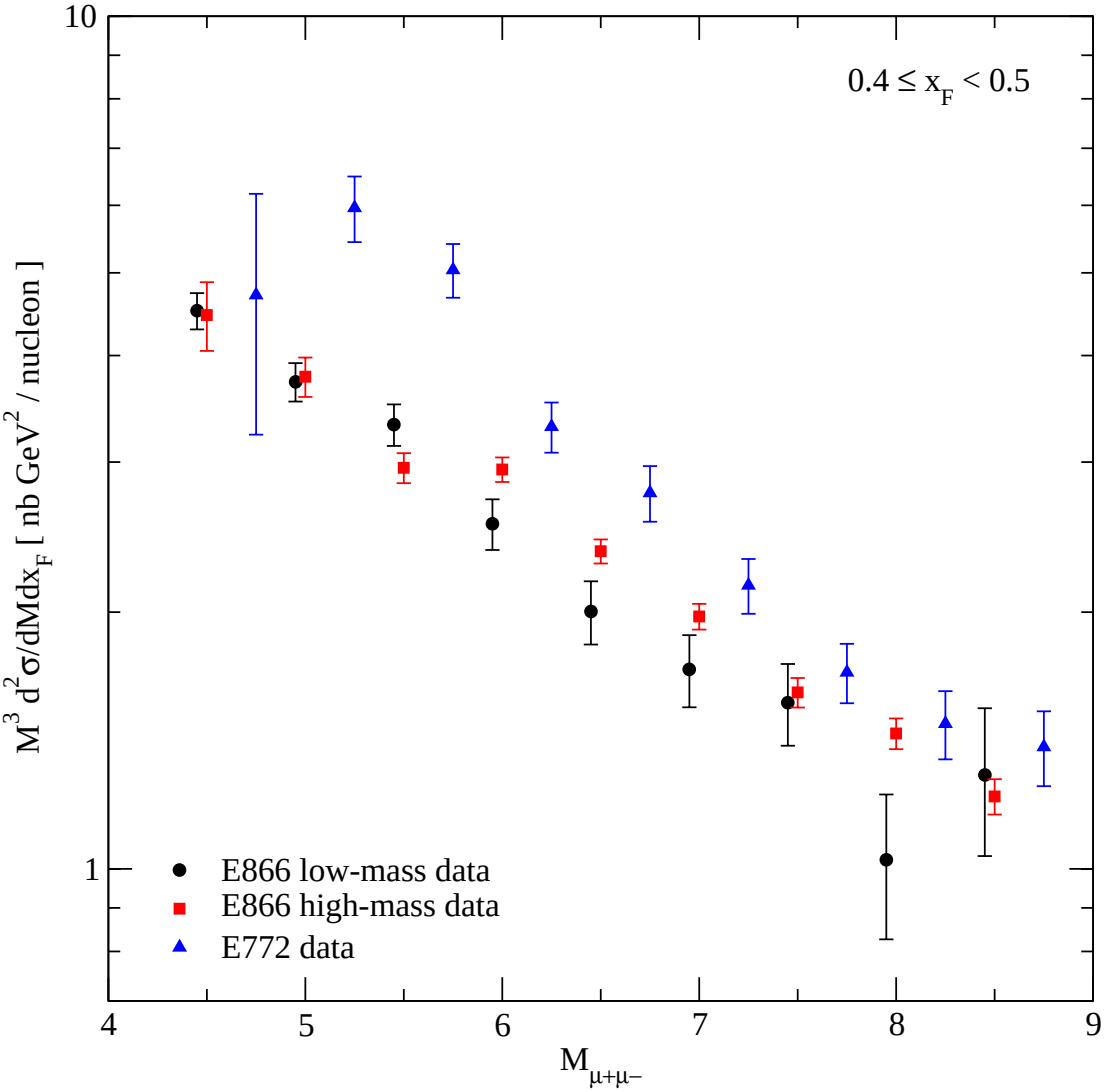

Figure 6.3: A comparison of the results from the low- and high-mass data sets to the E772 results for $0.4 \leq x_F < 0.5$. Error bars represent the statistical uncertainties only, and the high mass data has been offset from the bin center by 0.05 GeV.

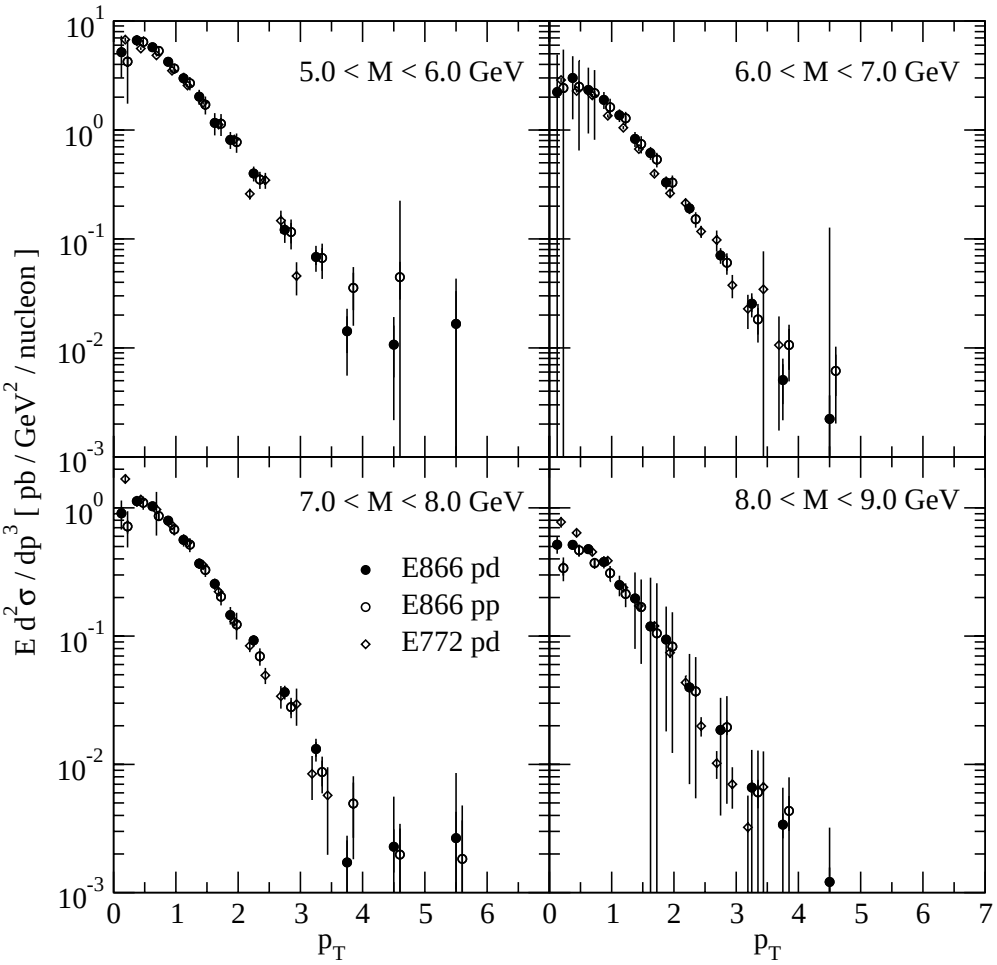

Figure 6.4: Comparison of the E866 measurement of the invariant cross section $Ed^3\sigma/dp^3$ in pd (closed circles) and pp (open circles, offset by 0.1 GeV) interactions to the E772 pd (open diamonds, offset by 0.05 GeV) measurement. The cross sections are in the range $0 \leq x_F < 0.3$. The E866 error bars are the linear sum of the statistical and systematic uncertainties.

the deuterium-to-hydrogen cross section ratio as a function of x_2, which provides a clean probe of the Björken-x dependence of the ratio of anti-down to anti-up quarks in the nucleon sea[3]. Those results [Haw 98, Tow 01] have already been published and incorporated into the various global analyses of the parton distribution functions [CTEQ, MRST, GRV].

Although the previous analysis and this current work began with the same data sample, the tighter event selection criteria required for absolute normalization resulted in the elimination of much of the data above $x_2 \approx 0.15$. Direct comparison between the results presented in chapter 5 and those of Towell *et al.* [Tow 01] are complicated by this. Further complicating matters, the results of Towell *et al.* are differential only in a single variable (x_2)[4], while our new results are differential in the mass and x_F of the dimuon pair.

In figure 6.5, we present the deuterium-to-hydrogen cross-section ratio versus mass in four x_F bins. The ratios were calculated by integrating the data in tables 5.3 through 5.10 over all p_T and taking the ratio of deuterium to hydrogen in each bin. Next-to-leading order calculations of the cross section ratio, based on the CTEQ 5 and CTEQ 6[5] parton distributions, are also shown in the figure. Since

[3]Although not explicitly shown in chapter 1, the ratio of the leading-order pd and pp cross sections can be written for large x_F as $\frac{\sigma_{pd}}{\sigma_{pp}}(M, x_F; x_2) \approx \left\{\frac{1+\frac{1}{4}\frac{d}{u}(x_1)}{1+\frac{1}{4}\frac{d}{u}(x_1)\frac{\bar{d}}{\bar{u}}(x_2)}\right\}\left(1+\frac{\bar{d}}{\bar{u}}(x_2)\right)$, where x_2 is evaluated according to equation 1.3.

[4]Towell *et al.* did look at the cross section ratio versus other variables, but none which are directly comparable to our double-differential cross sections.

[5]The MRST 98, MRST 2001 and GRV 98 parton distributions give similar results.

the E866 cross section ratios were used in the CTEQ 5 and CTEQ 6 global analyses, they provide a convenient means to check the consistency between the two analyses. We also superimpose the previous cross section ratio results of Towell *et al.* on figure 6.5. Although those results are differential only in x_2, reference [Tow 01] does quote a mean mass and x_F in each x_2 bin. We therefore plot the cross section ratios in each x_2 bin at the mean mass quoted in the reference, and only in the x_F bins appropriate to their mean x_F. Overall, the level of agreement between the data presented in chapter 5 and the cross section ratios previously published by E866 is quite good.

To provide a more detailed and direct comparison with the previously published results, we calculated the absolute cross section $d^2\sigma/dx_1dx_2$ for hydrogen and deuterium using the same x_2 binning as reference [Tow 01] and the same procedures as outlined in chapter 4. For this study, the event selection criteria were loosened to admit the large-x_2 events which were otherwise problematic in the absolute cross sections analysis[6]. Figure 6.7 shows the deuterium-to-hydrogen cross section ratio versus x_2 as calculated in this analysis in three different x_1 bins. As with the previous analysis, there appears to be no significant x_1 dependence on the cross section ratio. Averaging the ratios over all x_1 we obtain a cross section

[6]Specifically, these events tended to occupy regions of the spectrometer with either known efficiency problems or uncertainties in reconstructing the event kinematics. These effects should almost completely cancel in ratio. We did not include any data from intermediate mass data sets 3 and 4, which account for approximately 1/3 of the total number of events used in reference [Tow 01].

ratio versus x_2 only, which is compared with the results of Towell *et al.* in figure 6.7. The only differences between the two analyses are almost completely due to the larger event sample available to reference [Tow 01].

6.3 Data versus Theory

Detailed information on how our data will impact the parton distribution functions must inevitably await their incorporation into future global analyses. It is still useful to compare our results with theoretical calculations of continuum dimuon cross sections. Such comparisons will demonstrate whether the existing sets of parton distributions are consistent with our data in kinematic regions already constrained by previous measurements (E605), and reveal where we expect our data to substantially impact upon the parton distributions in the next round of fits.

As discussed back in chapter 1, continuum dimuon production is sensitive to the gluon distributions through QCD processes at and beyond next-to-leading-order. Dimuon production is dominated by gluon Compton scattering for $p_T > \frac{1}{2}M$ [Ber 98], and the E866 results satisfy this kinematic condition over an extended range in mass and x_F. Thus, in addition to information on the light-antiquark distributions, our data should provide a new and valuable source of information about the gluon distributions. Because this is still an area of ongoing theoretical investigation, in the following discussion we limit ourselves to a

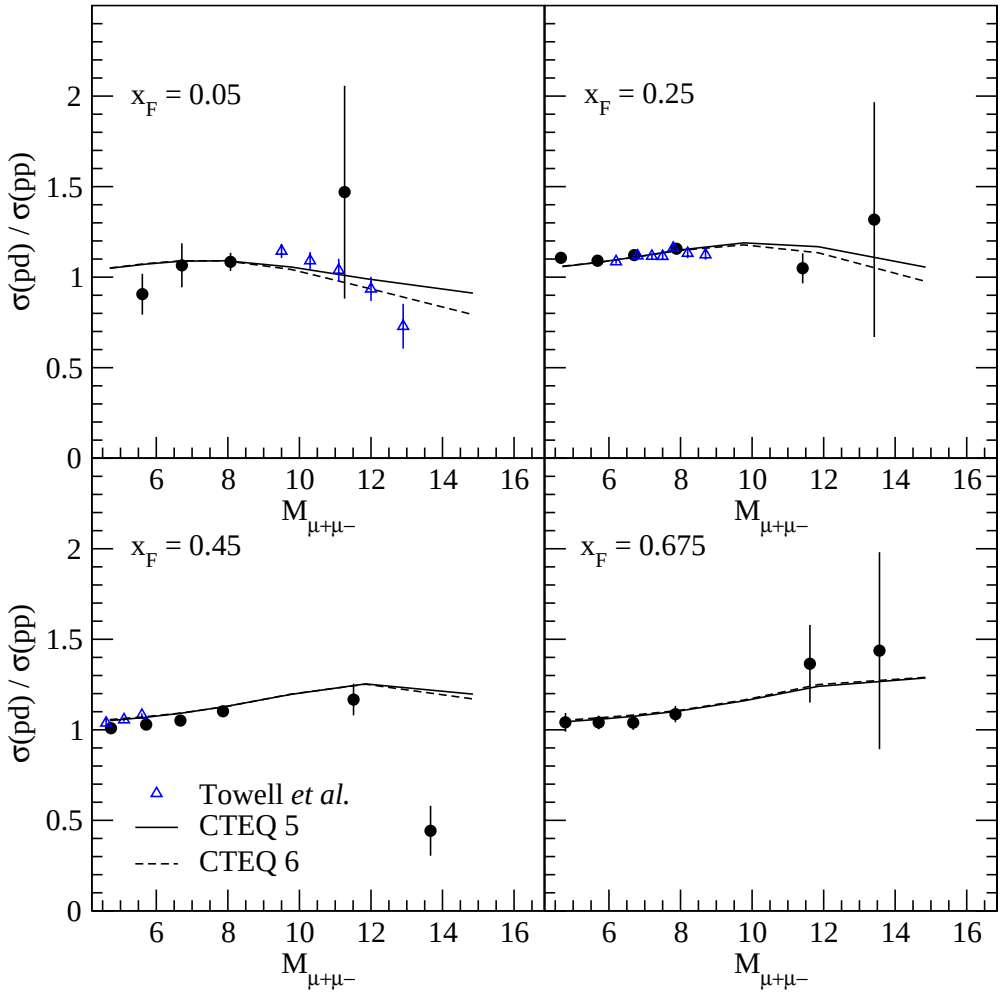

Figure 6.5: Ratio of *pd* and *pp* (per nucleon) cross sections. The results of this analysis (circles) are compared with the results (triangles) of the previous analysis of Towell *et al.* [Tow 01]. Although the results of Towell *et al.* are differential only in x_2, the mean mass and x_F of the events in each x_2 bin was tabulated in the reference. We plot those results at those mean mass values, and only in x_F bins appropriate to the mean x_F. NLO calculations of the ratio based on the CTEQ 5 and CTEQ 6 parton distributions are also shown.

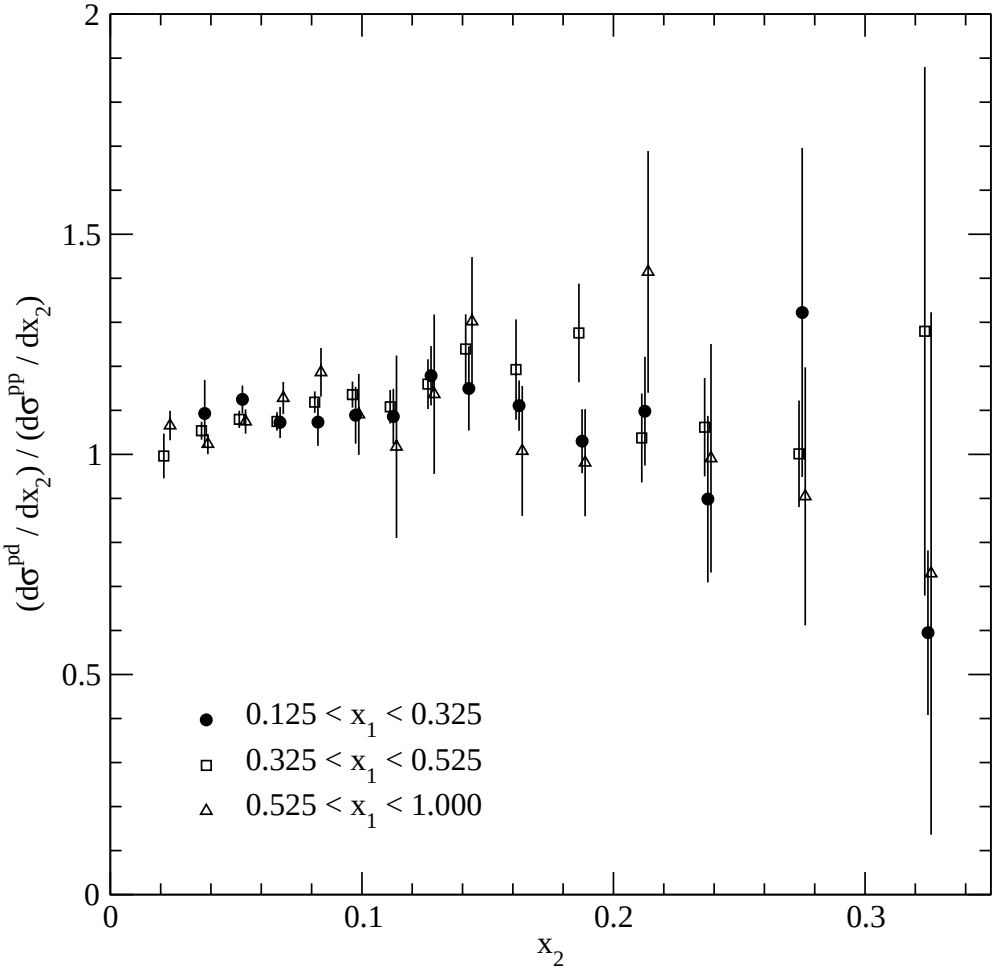

Figure 6.6: Ratio of *pd* and *pp* (per nucleon) cross sections plotted versus x_2 in three x_1 bins. The two larger x_1 bins are offset slightly in the horizontal direction from the bin center for clarity.

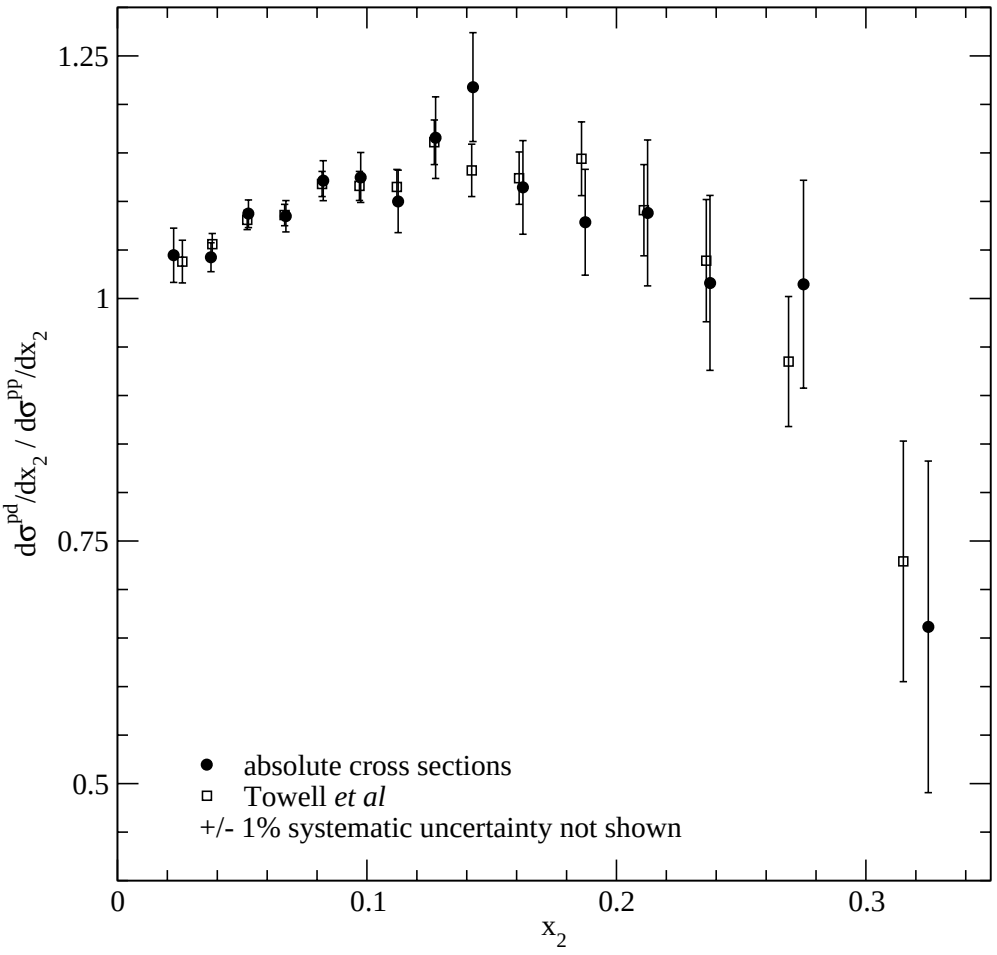

Figure 6.7: Ratio of *pd* and *pp* (per nucleon) cross sections plotted versus x_2, at the center of each x_2 bin. The data are compared with the previous E866 results, which are plotted at the mean x_2 in each bin. Both analyses are subject to an additional $\pm 1\%$ systematic uncertainty in the relative normalization.

discussion of the quark and antiquark distributions.

6.3.1 Scaling Form: $M^3 d^2\sigma/dMdx_F$

In the preceding chapter, the scaling form $M^3 d^2\sigma/dMdx_F$ was tabulated and plotted in mass and x_F bins. Figures 5.1 through 5.16 plotted the pp and pd cross section in x_F bins versus the invariant mass of the dimuon pair. In each x_F bin we also compared the data to perturbative QCD calculations performed to next-to-leading order. These calculations were based on several of the currently available and most commonly used sets of fits to the parton distributions. In general, they reproduce the shape and normalization of the data well, save for the GRV 98 distributions which systematically overestimate the data by $\sim 20\%$. To better illustrate this, the theoretical calculations were fit to the data to determine a "K'-factor", which we define as the ratio of the experimentally measured dimuon continuum to NLO theory.

The K'-factors for hydrogen and deuterium are shown in table 6.1. All of the parton distributions studied, with the exception of the GRV 98 set, reproduce the normalization of the measured cross sections to better than our systematic uncertainties. This is not unexpected. The valence distributions are well constrained by DIS measurements, and the E605 Drell-Yan data (with which we agree) are an important input into the fits, constraining the antiquark sea over much of the range covered by E866 [CTEQ, MRST, GRV].

Table 6.1: K'-factors, where $K' = \frac{\sigma^{\rm exp}}{\sigma^{\rm NLO}}$, for 800-GeV pp and pd dimuon production. The errors represent the statistical and point-to-point systematic uncertainties in the data. The data are subject to an additional $\pm 6.5\%$ uncertainty in the normalization.

PDF	K'_{pp}	χ^2/ndf	K'_{pd}	χ^2/ndf
CTEQ5	0.9753 ± 0.0037	1.47	0.9633 ± 0.0017	2.56
CTEQ6	1.0150 ± 0.0028	1.44	1.0003 ± 0.0004	2.62
MRST 98	0.9732 ± 0.0022	1.43	0.9604 ± 0.0028	2.42
MRST 2001	0.9799 ± 0.0034	1.50	0.9664 ± 0.0078	2.48
GRV 98	0.8107 ± 0.0043	2.11	0.8075 ± 0.0002	4.24

It is interesting to note the improvement in the normalization of the CTEQ 6 [CTEQ 02] based calculations relative to CTEQ 5 [CTEQ 99]. The main difference between the CTEQ 6 distributions and the previous CTEQ fit is a stiffer large-x gluon, the result of including Tevatron jet data in the newer analysis [CTEQ 02]. The same data has also been incorporated into the latest MRST fit [MRST 01], but without as significant a change in the gluon distributions. Though there is improvement in the calculations based on the MRST 2001 distributions over the previous MRST analysis, it is not as dramatic as that seen in the CTEQ distributions.

The relatively poor quality of the fits shown in table 6.1 can be explained by behavior observed in the cross sections which was not anticipated by the parton

distribution functions. The agreement between data and theory is quite good below $x_F \approx 0.3$, which is not surprising given the degree of agreement with the E605 data previously discussed. As x_F increases beyond the range constrained by E605, the agreement between the E866 data and the NLO calculations deteriorates, especially at low mass. While this kinematic range probes smaller values of x_2 than reached in E605, it also probes values of x_1 (the momentum fraction of the annihilating quark in the parton model) where the estimated uncertainties on the valence quark distributions are about $\sim 20\%$. Thus, we expect our data to provide important constraints on both the valence and sea quarks in the next round of fits.

6.3.2 $d^2\sigma/dx_1dx_2$

To explore the impact of our data on future fits in more detail, we now examine the cross sections written in the form $d^2\sigma/dx_1dx_2$. While higher-order QCD processes confuse the interpretation of x_1 and x_2 here, one should recall that almost half of the cross section is due to the leading-order $q\bar{q}$ annihilation for which x_1 and x_2 have their usual meaning. Writing the pp and pd cross sections in the limit of large x_F we have

$$\begin{aligned} \frac{d^2\sigma_{pp}}{dx_1dx_2} &\propto \frac{4}{9}u(x_1)\bar{u}(x_2) + \frac{1}{9}d(x_1)\bar{d}(x_2) \\ \frac{d^2\sigma_{pd}}{dx_1dx_2} &\propto \left\{\frac{4u(x_1)+d(x_1)}{9}\right\}\left(\bar{d}(x_2)+\bar{u}(x_2)\right). \end{aligned} \tag{6.1}$$

Thus, the shape of the cross sections relative to theoretical calculations should help us understand the effect of our data on the parton distributions.

In the comparisons between data and theory which follow, the cross sections of the form $d^2\sigma/dx_1dx_2$ were determined using the same procedures outlined in previous chapters. However, certain limitations are imposed on this analysis by the Monte Carlo event sample, which was generated over a limited range in mass and x_F. Because of this, calculating the acceptance in the lowest-lying x_1-x_2 bins is problematic – the x_1-x_2 bins extend beyond the kinematic limits of the Monte Carlo sample. This mainly affects the data below $x_2 = 0.03$, which partially overlaps the low-mass, large-x_F data discussed in the previous section.

To study the likely impact of our data on future fits to the antiquark distributions, we examine the behavior of data and theory as a function of x_2, the momentum fraction of the annihilating antiquark in the parton model. After the cross sections differential in the momentum fractions of the interacting partons was determined, the ratio of those cross sections to next-to-leading-order calculations based on the CTEQ 6 [CTEQ 02] partons was calculated in each x_1-x_2 bin. Figure 6.8 shows these ratios in two x_1 bins, each containing roughly the same number of events. The difference in shape (if any) between data and theory versus x_2 appears to be consistent over the two ranges in x_1.

In figure 6.9 we average together the ratios of data and theory over all x_1 bins to obtain the ratio of data to theory as a function of x_2 only. The theoretical

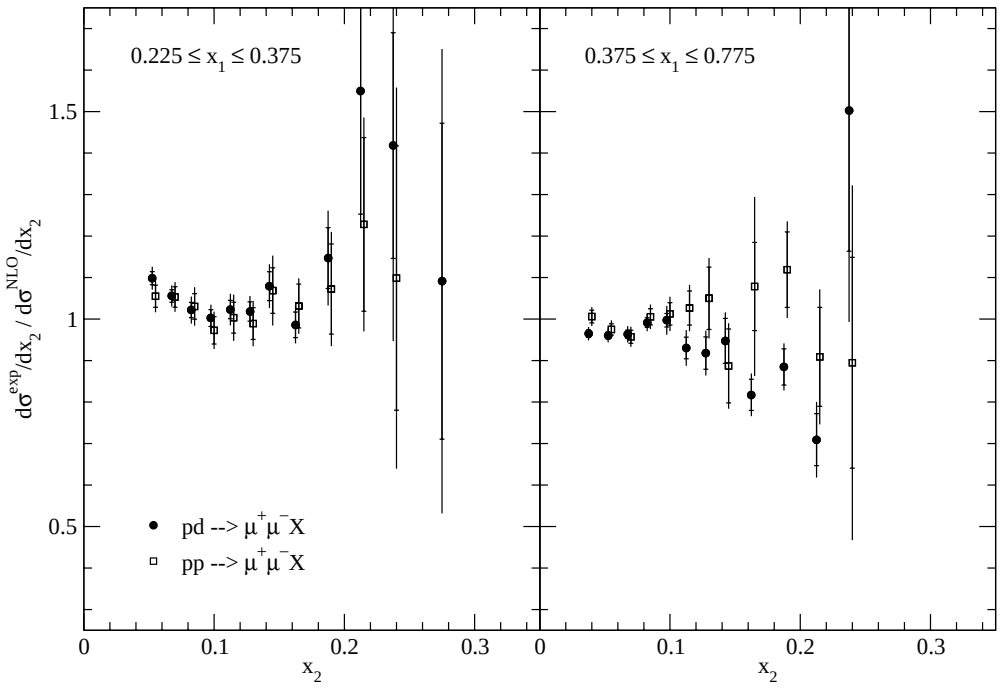

Figure 6.8: Ratio of data to NLO calculations based on CTEQ 6 [CTEQ 02] versus x_2. The left panel shows the range $0.225 \leq x_1 < 0.375$, and the right panel shows the range $0.375 \leq x_1 < 0.775$.

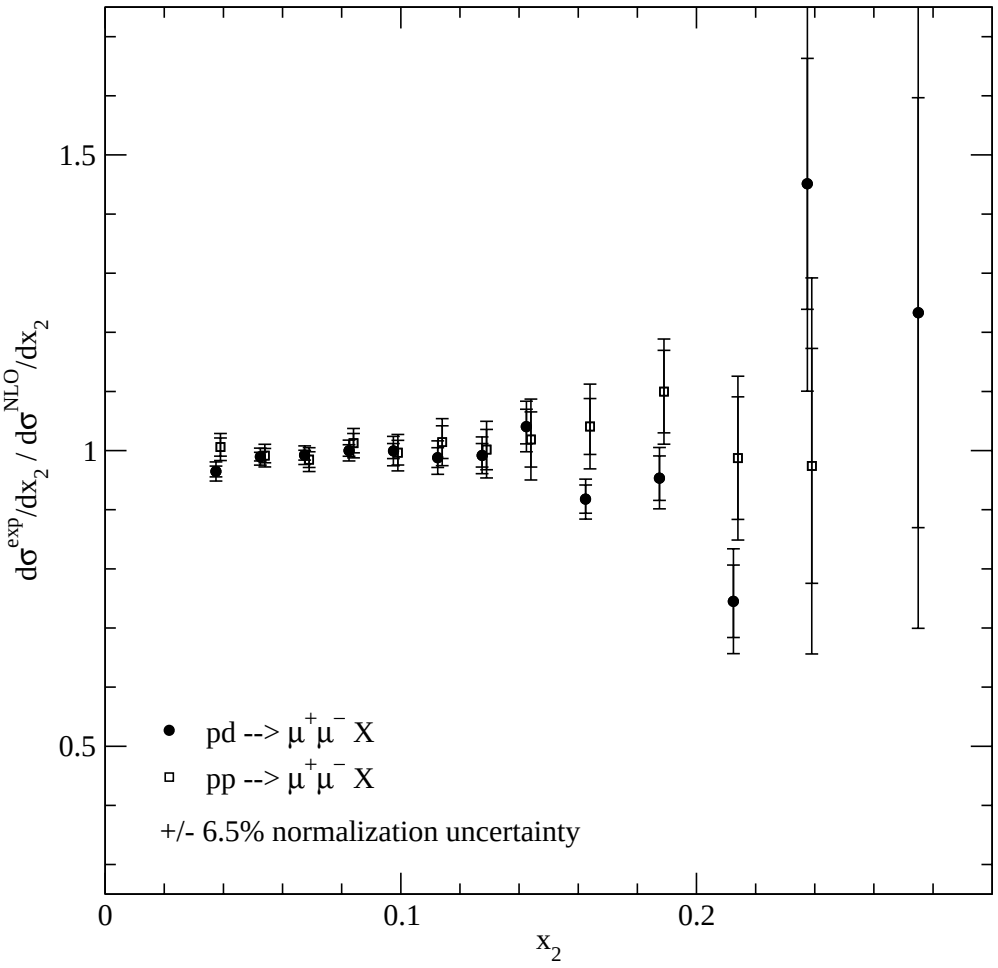

Figure 6.9: Ratio of data to NLO calculations based on CTEQ 6 [CTEQ 02] versus x_2.

calculations clearly reproduce our data well, to within the quoted statistical and systematic errors in the data, over the x_2 range covered. This indicates that the CTEQ 6 fits to the light antiquarks are consistent with our data. Since these fits are largely constrained by the E605 Drell-Yan measurements, this result was not unexpected.

The same analysis can be carried out to examine what our data imply for

future fits to the valence quark distributions. Figure 6.10 shows data-divided-by-theory plotted versus x_1, over two x_2 ranges each representing about half of the available statistics. There is an x_1 dependence which is consistent in both x_2 bins. Combining the results over all x_2 in figure 6.11 we see that at large x_1 the data falls about 20% below the theoretical predictions. This seems to suggest that the valence quark distributions are smaller at large Björken-x than in current parton distributions, though not outside the estimated uncertainties of the fits [CTEQ 02]. Parton distribution fits to DIS data at next-to-next-to-leading-order have also recently become available [MRST 02], and they also suggest a reduced valence distribution, relative to current NLO fits.

6.4 Future Prospects

Continuum dimuon production has been an active area of reseach for over thirty years, and the outlook for future measurements remains bright. Based on the cross section ratios published by E866 [Haw 98, Tow 01], Fermilab has accepted a proposal [E906] for a new dimuon experiment, Fermilab Experiment 906, to be conducted using the 120-GeV proton beam from the Main Injector. Like E866, the E906 measurements will examine the differences in continuum dimuon production in pp and pd interactions. Their primary goal is to measured $\frac{\bar{d}}{\bar{u}}(x)$ out to $x \approx 0.5$. The extended range in x is made possible in large measure due to the seven-fold increase in cross section using 120-GeV protons relative to 800-GeV protons.

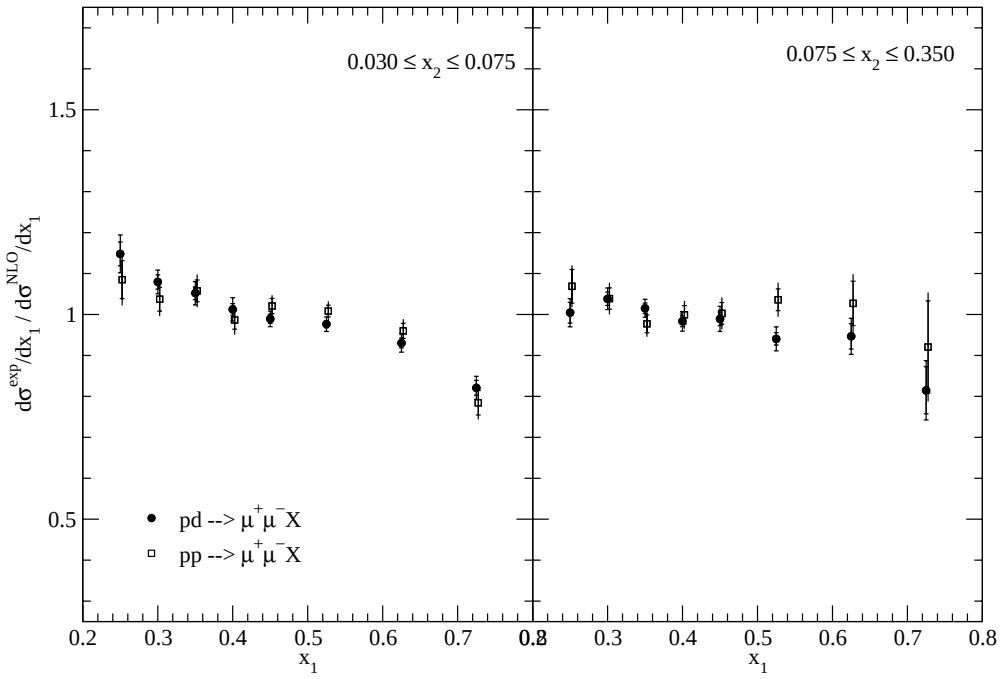

Figure 6.10: Ratio of data to NLO calculations based on CTEQ 6 [CTEQ 02] versus x_1. The left panel shows the range $0.225 \leq x_2 < 0.375$, and the right panel shows the range $0.03 \leq x_2 < 0.350$.

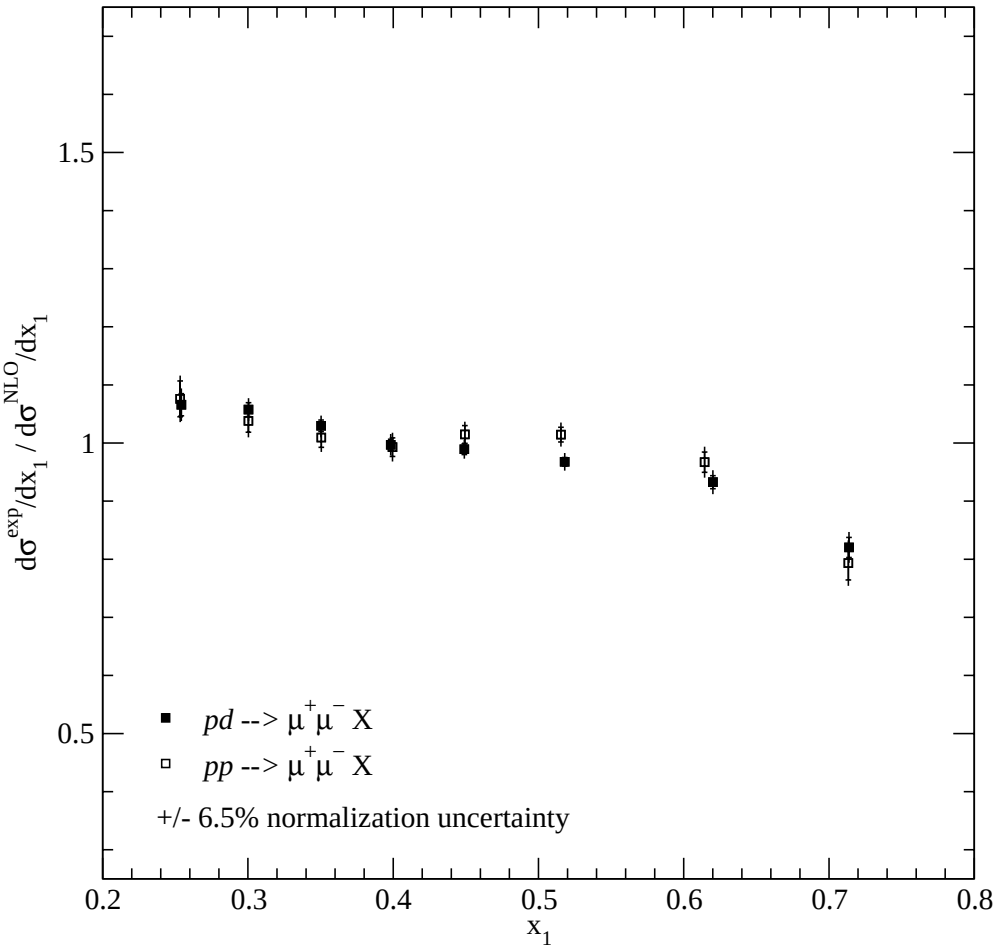

Figure 6.11: Ratio of data to NLO calculations based on CTEQ 6 [CTEQ 02] versus x_1.

Flavor asymmetry is but one of the topics to be adressed with the new experiment. Absolute measurements of the hydrogen and deuterium cross sections will also be possible, greatly extending the kinematic range and statistical precision available to constrain the parton distributions. Furthermore, these measurements may also be able to demonstrate an important property of QCD. Logarithmic scaling violations have long been established in DIS measurements, but have not been conclusively shown using the Drell-Yan process. The reasons for this include the relatively high q^2 probed in dimuon experiments, and the partial cancelation of the effect between the large-x behavior of the valence quarks, and the low-x behavior of the antiquarks [Fre 90, McG 99]. Given the statistical precision and overall understanding of systematic uncertainties attained with the E866 results, comparisons with the future measurements of E906 may well be able to demonstrate scaling violations in the Drell-Yan process.

6.5 Conclusion

Fermilab Experiment 866 has performed an absolute measurement of dimuon cross sections in 800-GeV pp and pd interactions. These data represent the most extensive measurement of the Drell-Yan process to date, covering a wider range of kinematics with better statistical precision than has been achieved in previous measurements. The results are in good agreement with existing pA and pd measurements, as well as NLO calculations based on the various sets of parton

distribution functions. The overall level of agreement between data and theory indicates that the antiquark distributions are well understood over the kinematic range relevant to E866. However, differences between data and theory suggest that the valence distributions are overestimated at large x in current parameterizations. Given the statistical precision of the data, we can expect a major impact on future fits to the valence quarks.

REFERENCES

[Ada 95] M.R. Adams et al., Phys. Rev. Lett. **75**, 1466 (1995).

[Ald 90] D.M. Alde et al., Phys. Rev. Lett. **64**, 2479 (1990).

[Ama 91] P. Amaudruz et al., Phys. Rev. Lett. **66**, 2712 (1991); M. Arneodo *et al.* , Phys. Rev. D **50**, R1 (1994).

[Ana 88] E. Anassontzis, et al. Phys. Rev. D **38**, 1377 (1988).

[Ant 82] D. Antreasyan et al., Phys. Rev. Lett. **48**, 302 (1982).

[Bad 83] J. Baider et al., Z. Phys. C **18**, 281, (1983).

[Bal 94] A. Baldit et al., Phys. Lett. B **332**, 244 (1994).

[Bak 84] S.I. Baker *et al.*, Nucl. Inst. Methods A **222**, 467 (1984).

[Ber 98] E. L. Berger, L. E. Gordon and M. Klasen, Phys. Rev. D **58**, 74012 (1998).

[Bet 85] B. Betev *et al.*, Z. Phys. C **28**, 9, (1985).

[Bro 97] C. N. Brown, E866 Internal Memo, September, 1997, *unpublished* .

[Bro 01] C. N. Brown *et al.*, Phys. Rev. Lett. **86**, 2259 (2001).

[Cha 99] T. Chang, New Mexico State University Ph.D. thesis, 1999.

[Chr 70] J.H. Christenson et al. Phys. Rev. Lett. **25**, 1523 (1970), Phys. Rev. D **8**, 2016 (1973).

[Cle 78] J. Cleymans and M. Kuroda, Nucl. Phys. B **155**, 480, (1979) [Erratum-ibid. B **160**, 510 (1979)].

[Cle 79] J. Cleymans and M. Kuroda, Nucl. Phys. B **155**, 480, (1979); Phys. Lett. B **105**, 68 (1981).

[Col 77] J.C. Collins and D.E. Soper, Phys. Rev. D **16**, 2219 (1977).

[Con 89] J. S. Conway et al., Phys. Rev. D **39**, 92 (1989).

[Cor 80] M. Corden *et al.*, Phys. Lett. B **96**, 417 (1980)

[Cri 86] J. A. Crittenden *et al.*, Phys. Rev. D **34**, 2584 (1986); D. E. Jaffe *et al.*, Phys. Rev. D **40**, 2777 (1989).

[CTEQ] See references [CTEQ 99, CTEQ 02]

[CTEQ 99] CTEQ Collaboration, hep-ph/9903282

[CTEQ 02] CTEQ Collaboration, *lookup reference*

[Dre 70] S.D. Drell and T.M. Yan, Phys. Rev. Lett. **25**, 316 (1970).

[E906] The E906 Collaboration, Fermi National Accelerator Laboratory Proposal 906 (unpublished).

[Fre 90] K. Freudenreich, Int. J. Mod. Phys. A **5**, 3643, (1990).

[Haw 98] E.A. Hawker et al., Phys. Rev. Lett. **80**, 3715 (1998).

[Gag 98] C.A. Gagliardi *et al.*, Nucl. Inst. Methods A **418**, 322 (1998).

[GEANT] CN/ASD Group. *Geant – Detector Description and Simulation Tool Q123* CERN, 1993.

[Gin 86] A. Van Ginneken, Nucl. Inst. Methods A **251**, 21 (1986).

[Got 67] K. Gottfried, Phys. Rev. Lett. **18**, 1174 (1967).

[Gre 85] H. B. Greenlee *et al.* Phys. Rev. Lett. **55**, 1555 (1985).

[Gro 00] D. E. Groom *et al.*, The European Physical Journal C **15**, 1 (2000).

[GRV] See reference [GRV 98]

[GRV 98] European Phys. J. C **5**, 461, (1998).

[Kap 78] D. M. Kaplan et al. Phys. Rev. Lett. **40**, 435 (1978).

[McG] P.L. McGaughey (private communication).

[McG 94] P.L. McGaughey et al. Phys. Rev. D **50**, 3038 (1994) [Erratum-ibid. D **60**, 119903 (1999)].

[McG 99] P. M. McGaughey, J.M. Moss, J.C. Peng, Ann. Rev. Nucl. Part. Sci. 49, 217 (1999).

[Mor 91] G. Moreno, *et al.* Phys. Rev. D **43**, 2815 (1991).

[MRST] See references [MRST 98, MRST 01]

[MRST 98] Martin, Stirling, Roberts and Thorne, European Phys. J. C **4**, 463, (1998).

[MRST 01] Martin, Stirling, Roberts and Thorne, European Phys. J. C **23**, 73, (2002).

[MRST 02] Martin, Stirling, Roberts and Thorne, Phys. Lett. B **531**, 216 (2002).

[PAW] CN/ASD Group. *Paw Users Guide, Program Library Q121.* CERN, 1995.

[Pre 02] E. Presley (private communication).

[Ope 94] Vector Fields, LTD. *OPERA-3D Program*, 1994.

[Rod 73] H. M. Roder, G. E. Childs, R. D. McCarty and P.E. Angerhofer, *Survey of the Properties of the Hydrogen Isotopes Below their Critical Termperatures*, National Bureau of Standards Technical Note 641 (1973).

[Smi 81] S. R. Smith et al., Phys. Rev. Lett. **46**, 1607 (1981).

[Tow 99] R. S. Towell, University of Texas at Austin, Ph.D. thesis, 1999.

[Tow 01] R.S. Towell et al., Phys. Rev. D **64**, 052002 (2001).

[Yoh 78] J. K. Yoh et al. Phys. Rev. Lett. **41**, 684 (1978).